



**NTNU – Trondheim**  
Norwegian University of  
Science and Technology

# Impact behaviour of stiffened steel plates

**Sindre Hellem Sølvernes**

Civil and Environmental Engineering (2 year)

Submission date: June 2015

Supervisor: Magnus Langseth, KT

Co-supervisor: David Morin, KT  
Odd Sture Hopperstad, KT

Norwegian University of Science and Technology  
Department of Structural Engineering



## **MASTEROPPGAVE 2015**

for

*Sindre Sølvernes*

*Impact behaviour of stiffened steel plates*

### **Oppførsel til avstivede platefelt i stål utsatt for støtlast**

Design of steel offshore structures under accidental loads is becoming more and more important. Under such load cases, design codes may be very difficult to use or lead to very high cost for the structures due to the conservative assumptions that has to be made. To reduce these potential costs, the offshore industry is increasingly using non-linear finite element analyses (NFEA). While design codes require a basic knowledge of material and structures, the use of NFEA impose to the user a strong background with respect to material and fracture models, but also on finite element formulations. The aim of this master's thesis is to apply a research and industrial approach on a welded steel structure subjected to dynamic loading. The main outcome is to compare both approaches and generate modeling guidelines with respect to this particular problem. This Master's thesis will be carried out in collaboration with DNV-GL.

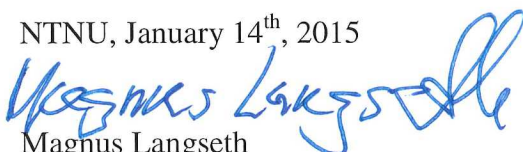
The following plan is proposed for the thesis work:

- A literature review shall be carried out on the behaviour and modelling of stiffened steel panels subjected to impact loading from a concentrated load.
- The student shall take part in the design of a test rig in the laboratory where generic testing of stiffened steel panels shall be carried out. This includes an evaluation of the support conditions, plate size and contact area between the impactor and the plate. The design shall be based on finite element simulations and simplified hand calculations.
- To carry out an experimental programme, i.e. material and component tests.
- To establish a numerical model and carry out a validation based on the tests carried out.
- Parametric studies and guidelines.
- Reporting.

*Supervisors: Magnus Langseth, David Morin and Odd Sture Hopperstad (NTNU)*

The candidate may agree with the supervisors to pay particular attention to specific parts of the investigation, or to include other aspects than those already mentioned. The thesis must be written as a research report, according to current requirements and submitted to Department of Structural Engineering, NTNU, no later than June 10<sup>th</sup>, 2015.

NTNU, January 14<sup>th</sup>, 2015



Magnus Langseth  
Professor



## PREFACE

This master's thesis within structural design has been carried out at the Department of Structural Engineering, NTNU.

Beforehand, the author had expectations that the thesis work would be challenging and enable the use of knowledge already gained and offer a chance to acquire further knowledge and expertise within the chosen field of specialization. By studying the impact behaviour of stiffened steel plates experimentally and numerically, these expectations were fulfilled.

This thesis has been carried out under the guidance and supervision of Professor Magnus Langseth, Professor Odd Sture Hopperstad and Dr David Morin. Their support and contributions throughout this study are gratefully acknowledged.

Special credits are also given to staff engineer Tore Wisth and senior engineer Trond Auestad at the Department of Structural Engineering, NTNU, for their decisive assistance and contribution to the experimental programme carried out.

The author would also like to thank fellow students Bente Larsen Kårstad and Birgitte Skajaa for the collaboration in designing a test rig to be used in testing of stiffened plates subjected to concentrated loading.

Trondheim, 9 June 2015

Sindre Sølvernes

Sindre Sølvernes



## **ABSTRACT**

The impact behaviour of stiffened steel plates subjected to impact loading from concentrated loads was studied experimentally and numerically. Both dynamic and quasi-static tests of stiffened steel plates with geometry adopted from a typical external deck area on an offshore platform were conducted. The quasi-static tests were performed to study the relationship between dynamic impact behaviour and the corresponding static ones. All tests were carried out in scale 1:4.

To allow the execution of generic testing in the laboratory, a steel frame that defines the support conditions for the test components is designed and constructed. Prior to the execution of the experimental programme, numerical models were created and several preliminary simulations of the tests were performed. The results from the preliminary simulations were directly used in the design phase of the tests, i.e. design of the test components and the support frame, determination of appropriate contact area between load and component, and determination of the load magnitude.

Tension tests were carried out to provide the necessary information on the strength and ductility of the steel material used in the stiffened plates. Based on the information obtained from the material tension tests, material models were created and implemented into the numerical models of the dynamic and quasi-static tests.

Comparisons between the numerical and experimental results were performed, mainly by comparing force-displacement curves. In order to determine the capacity of the stiffened steel plates by numerical simulations, three main approaches that involve predicting tensile failure was implemented.

The first approach is to use the Cockcroft-Latham fracture criterion which is based on calculation of accumulated damage during straining. With this approach it was possible to calculate the capacity with high precision. However, the way this fracture criterion was implemented it was inefficient with regard to computational time as it required a very dense mesh to obtain reliable results.

In the second approach, the Bressan-Williams-Hill instability criterion which is based on predicting the onset of local necking in a sheet metal was implemented. This method can be used with success for large-scale shell structures, where the element length is considerable larger than the plate thickness. For the applicable structure in this report, the Bressan-Williams-Hill instability criterion predicted acceptable estimates of the capacity, although with a higher degree of conservatism than expected in advance.

In the final approach a simplified check against tensile failure was performed according to a recommended practice from DNV-GL. The simplified approach provided conservative values of the plate capacity compared to the tests.





## SAMMENDRAG

Oppførselen til avstivede platefelt i stål utsatt for støtlast fra konsentrerte laster er studert numerisk og eksperimentelt. Både dynamiske og kvasi-statiske tester av avstivede platefelt i stål er utført og geometrien er hentet fra et typisk dekkområde på en offshore plattform. De kvasi-statiske testene ble utført for å studere sammenhengen mellom dynamisk og statisk oppførsel. Testene ble utført i skala 1:4.

For å kunne utføre generisk testing av platefelt i laboratoriet ble det konstruert en stållamme som definerte ønskede randbetingelser. På forhånd ble det etablert numeriske modeller for å kunne simulere testene før utførelsen av det eksperimentelle programmet. Endelig geometri av ramme og platefelt, fastsettelse av passende kontaktareal mellom påført last og platefelt samt størrelsen på lasten er basert på slike preliminære analyser.

Strekktester ble utført for å få nødvendig kunnskap om styrke og duktilitet for stålmaterialet benyttet i platefeltene. Basert på resultatene fra disse testene ble det etablert materialmodeller. Materialmodellene ble så implementert i numeriske analyser av dynamiske og kvasi-statiske tester av platefelt.

Videre ble det gjort sammenligninger av numeriske og eksperimentelle resultater, i hovedsak basert på kraft-forskyvningskurver. For å bestemme kapasiteten av platefeltene numerisk ble i hovedsak tre ulike metoder for å beregne strekkbrudd fulgt.

Den første metoden baserer seg på å beregne akkumulert skade påført materialet under tøyning ved hjelp av et kriterie omtalt som Cockcroft-Latham bruddkriterie. Med denne metoden var det mulig å beregne kapasiteten med høy presisjon. Derimot, som implementert i denne rapporten var denne metoden beregningsmessig uøkonomisk ettersom det var nødvendig å bruke et tett mesh i den numeriske modellen.

I den andre metoden er Bressan-Williams-Hill kriteriet implementert. Dette kriteriet baserer seg på å forutse begynnende ustabilitet i strekk for konstruksjoner som i hovedsak opplever en plan spenningstilstand. Denne metoden gir pålitelige resultater for numeriske modeller av skallkonstruksjoner hvor den karakteristiske elementlengden er betydelige større enn platetykkelsen. For den aktuelle konstruksjonen undersøkt i dette studiet ga Bressan-Williams-Hill kriteriet gode resultater, men med noe høyere grad av konservatisme enn forventet på forhånd.

Den tredje og siste metoden er en forenklet metode for å forutsi strekkbrudd i henhold til anbefalt praksis fra DNV-GL. Denne forenklete metoden gir konservative estimater for platekapasiteten sammenlignet med testene.



# CONTENTS

<b>PREFACE</b> .....	<b>i</b>
<b>ABSTRACT</b> .....	<b>iii</b>
<b>SAMMENDRAG</b> .....	<b>v</b>
<b>ABBREVIATIONS, NOTATIONS AND SYMBOLS</b> .....	<b>xi</b>
<b>1 INTRODUCTION</b> .....	<b>1</b>
1.1 Background .....	1
1.2 Previous work .....	2
1.3 Scope of work .....	3
1.4 Computer software .....	3
<b>2 THEORY</b> .....	<b>5</b>
2.1 Impact phenomena .....	5
2.1.1 General .....	5
2.1.2 Dropped object event .....	6
2.2 Non-linear finite element method .....	7
2.2.1 General .....	7
2.2.2 Motivation for using NFEM when dealing with impact problems .....	7
2.2.3 Finite element formulations .....	8
2.2.4 Dynamic stress/displacement analysis .....	9
2.2.5 Static stress/displacement analysis .....	11
2.3 Material modeling .....	11
2.3.1 General .....	11
2.3.2 Basic definitions and relations of stress and strain .....	12
2.3.3 The constitutive equations .....	13
2.3.4 Necking .....	16
2.3.5 Fracture criterions .....	17
<b>3 MATERIAL PROPERTIES</b> .....	<b>25</b>
3.1 Material tests .....	25
3.1.1 General .....	25
3.1.2 Test set-up .....	25
3.1.3 Test results .....	26
3.2 Material models .....	28
3.2.1 General .....	28
3.2.2 Validation of material models .....	30
3.2.3 Determination of $W_{cr}$ in CL fracture criterion .....	32
3.2.4 Stress based forming limit diagram according to BWH criterion .....	33
<b>4 DESIGN AND SET-UP OF COMPONENT TESTS</b> .....	<b>35</b>
4.1 General .....	35
4.2 Initial considerations and model selection .....	35
4.3 Test specimen, support frame and indenter geometry .....	36
4.3.1 Test specimen geometry .....	36
4.3.2 Test rig frame and test rig assembly .....	38

4.3.3	Corresponding idealized support conditions for specimen .....	40
4.3.4	Indenter geometries .....	40
4.4	Summary of design history .....	42
4.5	Preliminary analysis.....	45
4.5.1	General .....	45
4.5.2	Basic computer model 1 (rigid frame).....	45
4.5.3	Basic computer model 2 (deformable frame).....	48
4.5.4	Preliminary simulations of dynamic tests.....	52
4.5.5	Preliminary simulations of quasi-static tests .....	70
4.5.6	Calculation of stiffened steel plate initial bending capacity.....	72
4.6	Set-up of quasi-static tests .....	74
4.7	Set-up of dynamic tests.....	76
4.8	Test program.....	79
<b>5</b>	<b>RESULTS FROM COMPONENT TESTS.....</b>	<b>81</b>
5.1	Results from quasi-static tests.....	81
5.1.1	General .....	81
5.1.2	Load from indenter A .....	81
5.1.3	Load from indenter B .....	83
5.1.4	Test data accuracy .....	85
5.2	Results from dynamic tests .....	85
5.2.1	General .....	85
5.2.2	Load from indenter A .....	85
5.2.3	Load from indenter B .....	88
5.2.4	Test data accuracy .....	92
5.3	Scale effects .....	95
<b>6</b>	<b>ANALYSIS - VALIDATION BASED ON TESTS.....</b>	<b>97</b>
6.1	General.....	97
6.2	Computer model .....	97
6.3	Simulations of the quasi-static tests.....	99
6.3.1	Validation using CL fracture criterion .....	99
6.3.2	Validation using BWH instability criterion.....	103
6.3.3	Validation using DNV-RP-C208.....	108
6.4	Simulations of the dynamic tests .....	111
6.4.1	Validation using CL fracture criterion .....	111
6.4.2	Validation using BWH instability criterion.....	113
6.4.3	Validation using DNV-RP-C208.....	114
6.5	Discussion on results from numerical simulations .....	115
6.5.1	Strain rate sensitivity .....	115
6.5.2	Quasi-static versus dynamic simulation .....	117
6.5.3	Comparison of methods used to predict tensile failure .....	117
6.5.4	Model accuracy .....	121
<b>7</b>	<b>CONCLUSIONS AND RECOMMENDATIONS .....</b>	<b>123</b>
7.1	Conclusions.....	123
7.2	Recommendations for further work.....	124
<b>8</b>	<b>BIBLIOGRAPHY.....</b>	<b>125</b>

## **Appendices**

Appendix A

Drawings

Appendix B

Dynamic test results based on adjusted data



# ABBREVIATIONS, NOTATIONS AND SYMBOLS

## Abbreviations

BWH	Bressan-Williams-Hill
CL	Cockcroft-Latham
CS	Cowper-Symonds
DIC	Digital Image Correlation
DNV	Det Norske Veritas
DOF	Degrees of Freedom
EPC	Engineering, procurement and construction
FE	Finite Element
FEA	Finite Element Analysis
FEM	Finite Element Method
FLC	Forming Limit Curve
FLD	Forming Limit Diagram
GL	Germanischer Lloyd
ISO	International Organization for Standardization
NFEA	Non-linear Finite Element Analysis
NFEM	Non-linear Finite Element Method
ODS	Optical Displacement Sensor
RTCL	Rice-Tracey-Cockcroft-Latham
SHS	Square Hollow Section
SIMLab	Structural Impact Laboratory

## Notations and symbols

$A$	current cross-sectional area
$A_0$	initial cross-sectional area
$b$	width
$c_d$	dilatational wave speed
$C$	damping matrix / material constant
$E$	Young's modulus
$E_F$	frictional energy dissipated
$E_I$	internal energy
$E_K$	kinetic energy
$E_{tot}$	total energy
$E_V$	viscous energy dissipated by damping

$E_W$	external work
$F$	axial force / impact force
$F_{ext}$	external forces
$F_{int}$	internal forces
$f$	yield function
$f_y$	yield strength / yield stress
$f_u$	ultimate strength / ultimate stress
$h_R$	isotropic hardening modulus
$K$	power law parameter
$L^e$	characteristic length of smallest element in a mesh
$l_e$	initial length of element
$L$	current length
$L_0$	Initial length
$M$	mass matrix
$M_B$	rear mass (backing mass) of trolley
$M_N$	front part mass of trolley
$M_T$	mass of target (test specimen)
$n, \tilde{n}$	power law parameters
$P$	point load
$P$	force recorded by a load cell
$p$	plastic equivalent strain / material constant used in CS model
$\dot{p}$	plastic strain rate
$\dot{p}_0$	material parameter
$R$	hardening variable / reaction force
$t$	time, thickness
$t_e$	initial element thickness
$\Delta t_{cr}$	critical time increment
$T_1$	major principal tension
$u$	displacement vector
$v_0$	impact velocity
$w$	displacement
$W_l$	energy per unit volume used in CL fracture criterion
$W_{cr}$	critical energy per unit volume used in CL fracture criterion
$\alpha$	ratio between minor and major principal stress
$\beta$	ratio between minor and major principal strain
$\varepsilon$	true strain
$\varepsilon_1, \varepsilon_2, \varepsilon_3$	principal strains
$\varepsilon_e$	engineering strain



$\varepsilon_{eq}$	equivalent strain
$\varepsilon_u$	ultimate strain which corresponds to $f_u$
$\varepsilon_t$	strain in the direction of a shear plane
$\dot{\varepsilon}$	strain rate
$\dot{\varepsilon}_{ij}^p$	plastic strain rate tensor on index form
$\dot{\lambda}$	plastic multiplier
$\hat{\lambda}, \hat{\mu}$	Lamé constants
$\rho$	density
$\sigma$	true stress
$\sigma_1, \sigma_2, \sigma_3$	principal stresses
$\sigma'_1, \sigma'_2, \sigma'_3$	deviatoric stresses
$\sigma_0$	yield stress
$\sigma_e$	engineering stress
$\sigma_{eq}$	equivalent stress
$\sigma_{ij}$	stress tensor on index form
$\sigma$	stress tensor
$\tau_{cr}$	critical shear stress
$\nu$	Poisson's ratio
$\phi$	angle used in Hill's local necking criterion
$\varphi$	general symbol for the magnitude of a stress state
$\theta$	angle used in Bressan and Williams shear criterion



# 1 INTRODUCTION

## 1.1 Background

Design of offshore steel structures subjected to accidental loads is becoming more and more important. Accidental design situations involve exceptional conditions for the structure such as: impact, fire, explosion, local failure, loss of intended differential pressure (e.g. buoyancy). The emphasis in the present study will be on situations involving impact, i.e. the collision between two or more solids, which may arise due to ship collisions, fragments from explosions and dropped objects hitting parts of the structures.

Various structural design codes and regulations deal with impact loads and the definition of accidental impact events as well as acceptable design effect may vary. Where impact is a routine service condition, the structure should remain elastic, or close to elastic due to the impact loading. For abnormal or accidental events most structural design codes accept that local structural damage occur provided that the structure does not suffer a complete loss of integrity (e.g. a progressive collapse mechanism shall not occur).

In ISO 19900 [29] and ISO19902 [30] accidental design situations are used to provide robustness against events with a probability of exceedance of typically between  $10^{-3}$  and  $10^{-4}$  per annum. In the limit state checks, some or all of the partial safety factors are set to 1.0. The checks against accidental limit state ensure that local failure does not lead to a complete loss of integrity of the structure. The system ductility and reserve capacity may be taken into consideration in determining the resistance of the structure. Further it is required to check the post-damage integrity of the structure after the accidental event, if the assumed design structural resistance in accidental limit state implies a reduction in the load carrying capacity of ordinary loads (i.e. if large permanent deformations are allowed).

When considering the impact load cases as discussed above in the structural design, design codes may be difficult to use or lead to very high cost for the structures due to the conservative assumptions that has to be made. To reduce these potential costs, the offshore industry is increasingly using non-linear finite element analyses (NFEA). While design codes require a basic knowledge of materials and structures, the use of NFEA impose to the user a strong background with respect to material and fracture models, but also on finite element formulations. However, problems involving material instabilities and response discontinuities are still challenging problems to solve from a numerical point of view. Therefore it is a need for continued research to increase the physical understanding by performing material and component tests, and to compare numerical simulations with experimental results.

The structure of interest in the present study is adopted from a typical external deck area on the Edvard Grieg EPC Topside Project awarded to Kvaerner by the oil and gas company Lundin Norway AS. The applicable geometry was proposed and provided by DNV-GL. The most relevant design conditions in terms of impact for such a structure are the ones occurring due to dropped objects.

## 1.2 Previous work

Within the field of structural impact, quite a lot of research has been performed over the last decades. This part summarizes some of the work that is considered relevant for the present study regarding the impact behaviour of stiffened steel plates. A major part of the research work considered relevant is aimed towards accidental scenarios considering collision and grounding of ships. However, due to the similarities, many of the findings are also applicable when assessing the response of a deck structure which is hit by dropped objects.

Langseth and Larsen [12] performed an experimental investigation on the plugging capacity of simply supported and continuous steel plates with stringers subjected to impact load from a dropped drill-collar in the velocity range 0-50m/s. Both dynamic and static tests were performed and a comparison showed that the static and dynamic critical interface forces are approximately equal in the performed tests. Further it is concluded that strain rate effects are small for the applicable steel grade and can be neglected in the design.

Experimental and numerical results of various stiffened steel panel configurations subjected to lateral loading until fracture by a cone shaped indenter were reported by Alsos et al. [6] and [7]. The steel panels represent hull plates in ships subjected to grounding or collision actions. The performance of two failure criteria is investigated. In the first criterion, referred to as the RTCL damage criterion, the damage evolution of the material is followed, and fracture is initiated once the accumulated damage reaches a critical level. The second criterion, referred to as BWH instability criterion, gives a simplified way of determining the onset of material instability in tension. These two criteria are implemented into the explicit finite element code LS-DYNA where it is demonstrated that onset of tension failure may be estimated with good precision. In addition the influence of the element size with respect to onset of failure is studied.

Ehlers et al. [9] performed simulations of the collision response of three different ship side structures using the finite element method. The structures of interest were previously tested in large scale and these experiments were used to validate the simulations. Also here, different fracture criteria are implemented into LS-DYNA. It is found that handling of the mesh size sensitivity might be more important than the fracture criterion itself for the cases investigated.

Liu et al. [11] presents a simplified analytical method to examine the energy absorbing mechanisms of small-scale stiffened plate specimens, quasi-statically punched at the mid-span by a rigid indenter with a knife or a flat edge shape. The analytical method derives expressions to estimate the relation between the plastic deformation and the energy dissipation of the stiffened plates. The method describes the deformation mechanism and the inner force of the plate and the stiffeners individually. Both experiments and numerical simulations are conducted in order to validate the method and a good agreement is found when comparing results.

More research work will be discussed throughout the report where considered relevant.

### **1.3 Scope of work**

The aim of this master's thesis is to apply a research and industrial approach in determining the response and capacity of a stiffened steel plate subjected to dynamic impact loading. The main outcome is to compare both approaches with respect to this particular problem. Limited modeling guidelines will also be established. In communication with the supervisors for the thesis work it is agreed that the latter will not be put much emphasis on.

A major part of the thesis work consists of the design and execution of an experimental programme, i.e. material and component tests carried out in the laboratory. To enable generic testing of stiffened panels, a test rig will be designed in collaboration with two students conducting a parallel master's thesis work on the impact behaviour of stiffened aluminium plates.

### **1.4 Computer software**

Numerical simulations are performed using Abaqus [34]. Abaqus is a general purpose Finite Element Method (FEM) system provided by Dassault Systèmes SIMULIA Corp. A list of the main computer software used in the present work is included in chapter 8.



## 2 THEORY

### 2.1 Impact phenomena

#### 2.1.1 General

An impact can be defined as a force applied over a short time when two or more bodies collide. The general problem of an impact may be extremely complex. A complete description of the dynamics of impacting metal solids would demand that account be taken of the geometry of the interacting bodies, elastic, plastic and shock-wave propagation, hydrodynamic flow, finite strains and deformations, work hardening, thermal and frictional effects, and the initiation and propagation of failure in the colliding materials [2].

In order to distinguish between two solids involved in an impact, the terms projectile and target as used by Zukas et al. [2] is often used. All items capable of being launched can become a projectile. The target is defined as any moving or stationary object struck by a projectile.

Impact phenomena can be characterized in a number of ways, e.g.: according to impact angle, geometric and material characteristics, or striking velocity.

It is convenient to classify the target elements by thickness. Backman and Goldsmith [15] classify the target by thickness using the following definitions:

- *Semi-infinite*, if there is no influence on the distal boundary on the penetration process.
- *Thick*, if there is influence of the distal boundary on the penetration process only after substantial travel into the target element.
- *Intermediate*, if the rear surface exerts considerable influence on the deformation process during all (or nearly all) of the penetrator motion.
- *Thin*, if stress and deformation gradients throughout its thickness do not exist.

The following velocity ranges are often used in the classification of impact processes:

- Low velocity regime (0-50 m/s)
- Sub-ordnance velocity regime (50-500 m/s)
- Ordnance velocity regime (500-1300 m/s)
- Ultra-ordnance velocity regime (1300-3000 m/s)
- Hyper-velocity regime (>3000 m/s)

For the present study, only impacts in the low velocity regime are dealt with. This velocity regime covers e.g. dropped objects, vehicle impact and ship collisions.

An impact in the low velocity range can be divided into two separate phases [12]:

1. A transient phase where only the inertia forces are present.
2. A global mode phase where the supports are activated.

In the transient phase, only inertia forces are present as no forces are transmitted to the supports. In the global mode phase the target may behave almost quasi-statically. Figure 2-1 illustrates a typical force-time curve from the experiments on dropped drill-collars on steel plates performed by Langseth and Larsen [12].

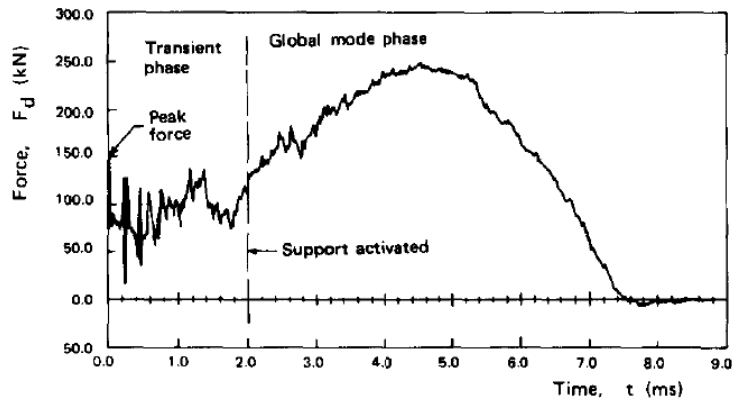


Figure 2-1: Impact phases. [12]

As previously described the geometry of the stiffened plate field of interest in the present study is adopted from a typical topside deck area. As the most relevant design conditions in terms of impact for such a structure is the ones occurring due to dropped objects, these events are briefly discussed in the next section.

### 2.1.2 Dropped object event

The dropped object load is characterized by a kinetic energy governed by the mass of the dropped object and its velocity at the instant of impact. The kinetic energy of the dropped object will partly be converted into elastic strain energy and partly dissipated through friction and as plastic strain energy. In addition energy will be dissipated by elastic vibrations in the dropped object and in the target.

The overall response will be a function of:

- Velocity and trajectory of dropped object
- Mechanical properties
- Geometry of dropped object and target
- Mass of dropped object and target
- Support conditions

The dynamic loads vary considerable depending on the total duration of the pulse and time of rise to a maximum value. For high impact velocities and/or stiff structures the mode of failure may be punishing shear (i.e. plugging) rather than global bending.

In the present study no attention will be made regarding the evaluation of the risk and the different operational consequences of a dropped object event. The emphasis will fully be on the impact behaviour of stiffened steel plates in terms of load bearing and energy absorption capacities. Nevertheless, a few general aspects of dropped object events are presented below.



Amdahl [16] divides the areas of offshore structures possible subjected to falling objects into three categories:

- Deck structure
- Process area
- Underwater structure

Dropped object in the process area are particularly dangerous as it may directly lead to fatalities in addition to structural and equipment damage, which again might lead to fire and explosions etc.

Amdahl [16] also divides the types of falling objects into three groups:

- *Loadfall*, caused by breaking of load line, failure of slings etc.
- *Boomfall*, caused by brake failure, boom twist-line failure etc.
- *Cranefall*, caused by crane overload or by breaks, fatigue.

The heaviest falling object will be the whole crane assembly itself with a typical weight of 60 tonnes [16].

For impacts against topside structure the impact velocity is given by simple energy considerations. For impacts against underwater structure the motion of the falling object will comprise the following phases:

1. Free fall in air from position at failure (if object is dropped from air)
2. Impact with water surface (if object is dropped from air)
3. Free fall in water from water surface until impact

In certain cases the impact will be damped due to the water pad being built up just before contact. The dropped object action in terms of kinetic energy may typically be estimated based on the aspects as mentioned above (location, type of object and fall height). However, specifications for design impact energy may typically be found in various industry design codes depending on type of structure of interest (topside, subsea etc.).

## **2.2 Non-linear finite element method**

### **2.2.1 General**

In this section some aspects of the non-linear finite element method will be briefly discussed. The emphasis will be on the major advantages of the method when dealing with problems similar as the present study, and to point out some of the important limitations. Derivations of the many solution methods within NFEM will not be given as it is comprehensive and not suitable for a report of this format. In addition the general theoretical foundation of the methods is well established and is presented in various text books, e.g. Cook et al. [1]. However, some of the methods and definitions that are considered central and discussed throughout this report will be mentioned.

### **2.2.2 Motivation for using NFEM when dealing with impact problems**

A linear response implies that there is always a linear fundamental relation between the representative load and the representative response of a system. As discussed in section 2.1.1 the general problem of impact may be extremely complex and highly non-linear, i.e. the

structural response can be markedly non-proportional to the applied loading. The sources of non-linear physical behaviour are:

- *Geometric non-linearity*: As the structure deforms a change in geometry occurs. This affects the strain-displacement (kinematic) and equilibrium equations for the system.
- *Material non-linearity*: In the impact problem the material behaviour may depend on the current deformation state. In addition the deformation history and rate of deformation may influence the overall response.
- *Non-linear boundary conditions*: At the interface between the projectile and the target, the applied force and contact area depend on the deformation. Depending on the geometries of the interacting bodies, the contact area may increase as the deformation develops then reduce when material fracture occurs.

In a non-linear finite element analysis all of the above physical behaviours may be approximated. The geometric non-linearity is accounted for by defining suitable finite element formulations that gives knowledge of the position occupied by the material particles comprising the body at all time [27]. The finite element formulation that is used in the major part of the present study is very briefly discussed in section 2.2.3. The material non-linearity is accounted for by defining material relations that defines the stresses in terms on strains and/or rate of strains. Material non-linearity is covered in more detail in section 2.3 as it is considered to be essential and considering the effort spent in studying the material properties of the steel structure in the present study.

Non-linear boundary conditions in an impact problem are accounted for by introducing a proper contact definition. Contact conditions are discontinuous non-linear constraints on the model allowing forces to be transmitted from one part of the model to another. The condition is discontinuous and non-linear as it is applied only when the surfaces are in contact, and when the surfaces separate the constraint is removed. Several different approaches exist for the solution of contact problems. The solution method that is used in the numerical simulations in the present study is referred to as the penalty method. The penalty method satisfies the contact condition approximately where the amount of penetration depends on a penalty parameter. The penalty parameter can be interpreted as a spring stiffness in the contact interface between two interacting bodies. Abaqus [34] which is the FEM software used in the numerical simulations in the present study specifies the penalty parameter automatically (manual input is possible). The accuracy of the solution may be checked by evaluating the amount of energy generated by the penalty solution, i.e. by integrating the contact force over the penetration depth. For the solution to be acceptable, this energy should be low and negligible compared to the internal energy of the system.

### **2.2.3 Finite element formulations**

An element's formulation refers to the mathematical theory used to define the element's behaviour. In the Lagrangian, or material, description of behaviour the element deforms with the material. In the alternative Eulerian, or spatial, description of elements are fixed in space as the material flows through them. A vast amount of different finite element formulations are available in most general purpose FEM systems and a number of aspects must be considered when selecting a proper element for the problem at hand. A successful application of FEA, lies in the combined choice of element types (i.e. mathematical model) and associated FE mesh. The most effective mathematical model will be the one which delivers the answer in a reliable manner with the least amount of effort [25].

It is well proven that elements within the shell-family are suitable for numerical simulations of stiffened steel plate fields subjected to transverse and in-plane loading. This statement is further backed by the reliable analysis results reported by e.g. Langseth et al. [13] and by Alsos et al. [7]. Shell elements are computationally effective and allow large scale structures (e.g. offshore deck structures or the hull of a ship) to be modeled with much fewer system degrees of freedom than if solid elements were used to obtain the same accuracy.

The shell element used in the numerical simulations of the stiffened steel plate in the present study is referred to as S4R in the Abaqus [34] theory guide. This element is a 4-node (quadrilateral) general-purpose shell element that provides robust and accurate solutions in all loading conditions for thin and thick shell problems. The thickness is given as a section property and the geometry of the shell is a 2D flat plate. 5 through thickness integration points for the shell element is used in the present study. Some important attributes are:

- Finite membrane strains and thickness change as a function of in-plane deformation: I.e. suitable for large strain problems.
- Uniformly reduced integration: Included to avoid shear and membrane locking and to improve computational efficiency.
- Hourglass control: No unconstrained hourglass modes or no issues with transverse shear locking.
- Converges to shear flexible theory (e.g. Mindlin-Reissner shell theory) for thick shells and classical theory (Kirchhoff-Love shell theory) for thin shells.

#### 2.2.4 Dynamic stress/displacement analysis

As mentioned in section 2.1 an impact event includes varying inertia forces and the transmission of kinetic energy into strain energy over short time duration. In order to capture these effects the dynamic equilibrium equations for the system must be solved. The general equation system of structural dynamics may be expressed as:

$$M\ddot{u}(t) + C\dot{u}(t) + F_{int}(t) = F_{ext}(t) \quad (2-1)$$

Where  $M$  is the system mass matrix,  $C$  is the damping matrix,  $u$  is the displacement vector,  $F_{int}$  is the internal forces and  $F_{ext}$  is the external forces.

As nonlinearities are present the dynamic response must be obtained by direct integration of the coupled dynamic equations of motion over the time domain (as oppose to modal superposition that may be suitable for linear systems). The various direct integration schemes are classified into the either implicit or explicit schemes.

- *Explicit methods*: The displacement at time  $t_{n+1}$  is obtained directly (explicitly) from the equilibrium conditions at one or more preceding time steps ( $t \leq t_n$ ) without solving an equation system. I.e. unknown values are obtained from information already known and the solution scheme does not require matrix inversion or iterations.
- *Implicit methods*: The displacement is obtained indirectly (implicitly) from the equilibrium condition at time  $t_{n+1}$ . I.e. equation solving is required.

It is generally established that the explicit method is preferable when dealing with high speed simulations as e.g. impact problems and when dealing with problems involving complicated discontinuous nonlinearities (complicated contact problems) [26]. The main obstacle for the explicit method is that the method is conditionally stable in the sense that a solution is

bounded only when the time increment  $\Delta t$  is less than a stable time increment  $\Delta t_{cr}$ . The stability limit is given in terms of the highest frequency of the system and a fraction of critical damping in the mode with highest frequency (if damping is included).

An approximation to the stability limit is often written as the smallest transit time of a dilatational wave across any of the elements in the mesh. This may be expressed as:

$$\Delta t_{cr} = \frac{L^e}{c_d} \quad (2-2)$$

where  $L^e$  is the characteristic length of the smallest element in the mesh, and  $c_d$  is the dilatational wave speed (speed of sound in the material). According to the analysis user guide for Abaqus [34], the dilatational wave speed for the shell elements is expressed as:

$$c_d = \sqrt{\frac{\hat{\lambda} + 2\hat{\mu}}{\rho}} \quad (2-3)$$

where  $\rho$  is the density of the material and the expression  $\hat{\lambda} + 2\hat{\mu}$  is the effective moduli for the section.  $\hat{\mu}$  and  $\hat{\lambda}$  are the Lamé constants which for an isotropic elastic material is defined in terms of the Young's modulus  $E$  and poisson's ratio  $\nu$  as:

$$\hat{\lambda} = \frac{E\nu}{(1+\nu)(1-2\nu)} \quad \text{and} \quad \hat{\mu} = \frac{E}{2(1+\nu)} \quad (2-4)$$

The final important matter that will be mentioned in this section is the need to perform energy balance check when dynamic problems are solved using the explicit method. A typical issue is that numerical instability can be hard to detect as it may be dissipated by energy-dissipating material behaviour (e.g. elastic-plastic behaviour). An energy balance for the entire FE-model may be written as:

$$E_I + E_V + E_F + E_K - E_W = E_{tot} = \text{constant} \quad (2-5)$$

Where:

- $E_I$ : Internal energy (sum of the recoverable elastic energy, energy dissipated through inelastic processes such as plastic flow, energy dissipated through viscoelasticity, and the artificial strain energy used in hourglass control and transverse shear resistance of e.g. shell elements)
- $E_V$ : Viscous energy dissipated by damping
- $E_F$ : Frictional energy dissipated
- $E_K$ : Kinetic energy
- $E_W$ : Work carried out by externally applied loads
- $E_{tot}$ : Sum of the energy components

It should be noted that the total energy is only approximately constant in a FE-model. For the solution to be acceptable the error should be generally less than 1% [26].

### 2.2.5 Static stress/displacement analysis

Non-linear static analyses are also performed as a part of the present study (analyses reported in section 3). In cases where the dynamic effects are not important, Equation (2-1) may be reduced to:

$$F_{int}(t) = F_{ext}(t) \quad (2-6)$$

An implicit equation solver will be used to solve these problems. Several methods exist to trace the equilibrium path for a non-linear static response. In the static analyses reported in this document, a displacement control algorithm will be used. This method is able to pass limit points and bifurcation points, but will stop at turning points, see Figure 2-2.

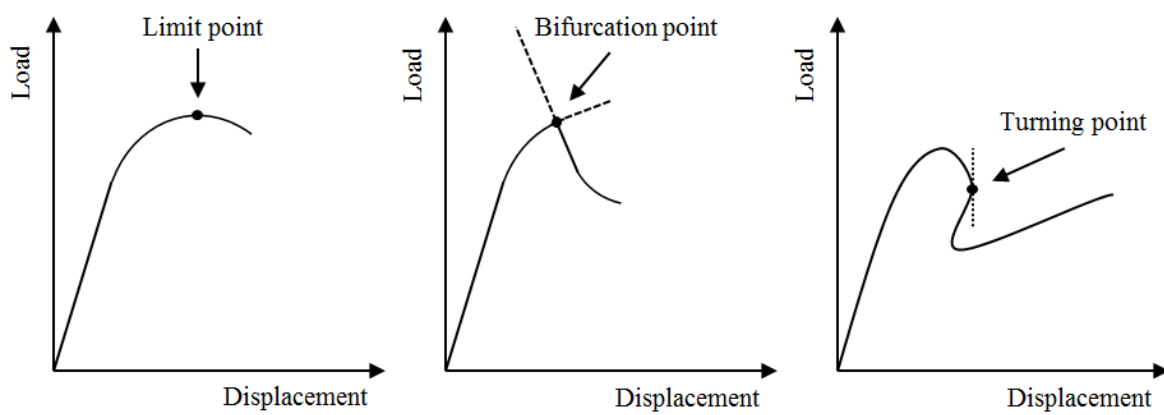


Figure 2-2: Limit, bifurcation and turning points.

## 2.3 Material modeling

### 2.3.1 General

In order to investigate the structural response (i.e. determine the internal strains and stresses and/or displacements) of a structure subject to loading, the mechanics of the used material have to be modeled. In mathematical models of material behaviour, an essential part is the relationship between the stress and strain the material exhibit. A typical stress-strain curve (engineering values) for structural steel in uniform tension is illustrated in Figure 2-3.

In the following sections, basic definitions required to create mathematical models of the behaviour of typical structural steel materials are presented. Phenomena such as necking and fracture (see Figure 2-3) will be described. Additionally, methods of how to predict fracture will be presented.

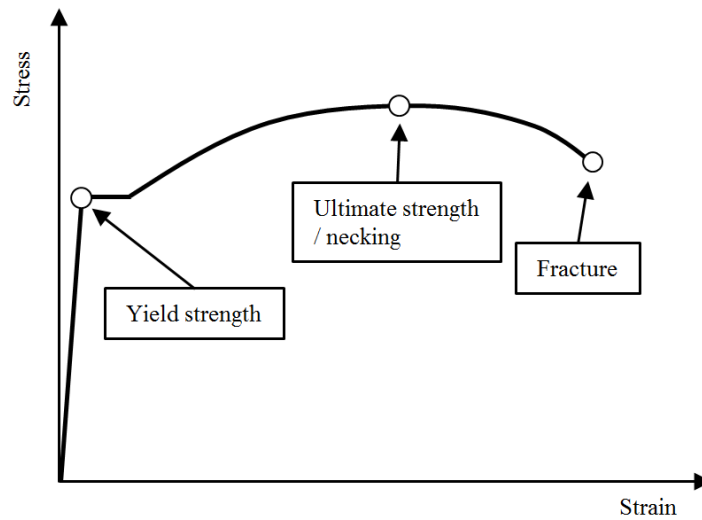


Figure 2-3: Illustration of a typical stress-strain curve (engineering values) for structural steel.

### 2.3.2 Basic definitions and relations of stress and strain

In this section the main stress and strain measures referred to throughout this report is presented. Further on, the basic relations regarding stress and strain are presented. The formulas presented in this chapter are taken from [3].

A one-dimensional uniform rod subjected to tensile loading is considered. Engineering stress  $\sigma_e$  and engineering strain  $\varepsilon_e$  is defined as:

$$\sigma_e = \frac{F}{A_0} \quad (2-7)$$

$$\varepsilon_e = \frac{\Delta L}{L_0} \quad (2-8)$$

Where  $F$  represents the axial force,  $A_0$  the initial cross-sectional area,  $L_0$  the initial length and  $\Delta L$  the incremental change in length of the specimen. The engineering stress and strain is applicable for infinitesimal (small) deformations. The relationship between stress and strain in the linear domain is given by Hooke's law:

$$\sigma_e = E\varepsilon_e \quad (2-9)$$

Where  $E$  represents the elastic modulus or Young's modulus defined as the slope of the initial linear portion of the stress-strain curve. In order to allow for finite (large) deformations, the Cauchy (or true) stress  $\sigma$  and the logarithmic (or true) strain  $\varepsilon$  is introduced as:

$$\sigma = \frac{F}{A} \quad (2-10)$$

$$\varepsilon = \int_{L_0}^L \frac{dL}{L} = \ln(L) - \ln(L_0) = \ln\left(\frac{L}{L_0}\right) \quad (2-11)$$

Where  $A$  refers to the current cross-sectional area and  $L$  refers to the current length of the specimen. By referring to the current dimensions we account for geometrical changes of the specimen during straining, and hence allow for large deformations in the stress and strain measures.

For metals the plastic deformation is in general volume preserving. By assuming volume constancy we have the following relation:

$$A = \frac{A_0 L_0}{L} \quad (2-12)$$

By combining Equations (2-8), (2-10) and (2-12) we get the following relation between the true stress and the engineering stress:

$$\sigma = \frac{F}{A} = \frac{F}{A_0} \frac{L}{L_0} = \frac{F}{A_0} (1 + \varepsilon_e) = \sigma_e (1 + \varepsilon_e) \quad (2-13)$$

Similarly, by combining Equations (2-8) and (2-11) we get the following relation between the true strain and the engineering strain:

$$\varepsilon = \ln\left(\frac{L}{L_0}\right) = \ln(1 + \varepsilon_e) \quad (2-14)$$

The relations presented in Equation (2-13) and Equation (2-14) is typically used when establishing the true stress-strain curves from a conventional tension test. First the engineering stress and strain is calculated based on the initial dimensions of the specimen and the measured force and elongation during the tension test. Then the true stress and true strain are calculated based on the established engineering values.

### 2.3.3 The constitutive equations

#### General

The equations needed in order to describe the relations between stress and strain is called the constitutive equations (or material models). For a linear elastic material this relation is given by Hooke's law, refer to Equation (2-9). However, when describing non-linear material behaviour an augmented set of equations is needed depending on what type of material behaviour that one wishes to describe. In this report both elastic-plastic and elastic-viscoplastic material models are used in the performed study. The essential theory behind the above mentioned material models are briefly presented in this chapter.

#### Plasticity

Metals typically exhibit linear elastic behaviour for small stresses and strains. However for a certain level of stress, denoted the yield stress, the material behaviour becomes elastic-plastic. Plasticity describes the material response that is irreversible, i.e. parts of the strains in the elastic-plastic domain are not recovered as the material is unloaded. Other characteristics of an elastic-plastic material are that the material response depends on the loading or the strain history and that plastic work is dissipated as heat. In addition the response is said to be rate independent, i.e. the response does not depend on the velocity of the applied loading (or straining).

In order to describe an elastic-plastic material behaviour we need three essential components [3]:

- *A yield criterion*, relates to the state of stress at onset of yielding.
- *A plastic flow rule*, describes the increment of the plastic strain during yielding in a way that ensures non-negative dissipation.
- *A hardening rule*, describe how a material is strain-hardened as the plastic strain increases.

In the material models used in the present study, the von Mises yield criterion with the associated flow rule will be assumed. The von Mises yield criterion suggests that yielding begins when the second deviatoric stress invariant,  $J_2$  reaches a critical value, hence also referred to as  $J_2$  flow theory. The associated flow rule may be expressed as:

$$\dot{\epsilon}_{ij}^p = \dot{\lambda} \frac{\partial f}{\partial \sigma_{ij}} \quad (2-15)$$

Where  $\dot{\epsilon}_{ij}$  and  $\sigma_{ij}$  denotes the plastic strain rate and stress tensor on index form,  $\dot{\lambda}$  is the plastic multiplier, and  $f$  describes the yield function.

For elastic-plastic materials the yield function  $f$  defines whether we have elastic conditions or yielding by:

$$\begin{aligned} f < 0 & : \text{elastic conditions} \\ f = 0 & : \text{yielding} \\ f > 0 & : \text{physically impossible} \end{aligned} \quad (2-16)$$

The material behaviour may typically be idealized to be elastic-perfectly plastic or elastic-linear work-hardening. In the elastic-perfectly plastic case a further straining of the material occurs without any increase in the stress. In the elastic-linear work hardening case the stress increases linearly with the strain. The yield function for an elastic-plastic material with isotropic hardening may be expressed as [3]:

$$f(\boldsymbol{\sigma}, R) = \varphi(\boldsymbol{\sigma}) - (\sigma_0 + R) \quad (2-17)$$

Where  $\sigma_0$  denotes the yield stress and  $R$  is a hardening variable as a function of the accumulated (or equivalent) plastic strain  $p$ , and  $\sigma_{eq} = \varphi(\boldsymbol{\sigma})$  is the equivalent stress measuring the magnitude of the stress state which the material is subjected, and  $\boldsymbol{\sigma}$  is the stress tensor. The equivalent plastic strain is defined to be energy conjugate to the equivalent stress.

### Viscoplasticity

The flow stress of a metallic material very often depends on the rate of the plastic straining [3]. The rate-dependent part of the theory of plasticity is referred to as viscoplasticity. This theory has various applications and one of them is impact problems which is the topic of this thesis. As for elastic-plastic materials, the material characteristics such as irreversible deformation, path dependence and energy dissipation are still valid. The idealized behaviours of elastic-perfectly viscoplastic and for elastic-viscoplastic linear work-hardening are shown



in Figure 2-4.  $\sigma_v$  is the viscous part of the flow stress and from the figure it is seen that the viscous stress increases as the strain rate increases.

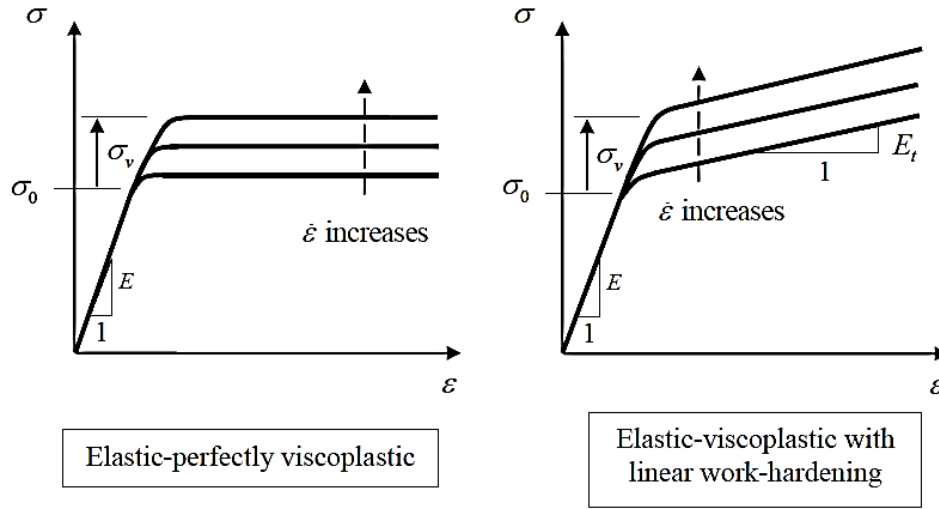


**Figure 2-4: Idealized elastic-viscoplastic behaviour. [3]**

A major difference from the theory of plasticity is that now the yield function is allowed to take values greater than zero [3]. It is now assumed that:

$$\begin{aligned} f \leq 0 & : \text{elastic conditions} \\ f > 0 & : \text{yielding} \end{aligned} \quad (2-18)$$

For an elastic-viscoplastic material we may express the flow stress as a function of the equivalent plastic strain rate  $\dot{p}$ , in addition to the yield stress and hardening variable as for elastic-plastic materials. In rate dependent  $J_2$  flow theory, the rate sensitivity may be described by either additive or multiplicative constitutive relations. In the material model that accounts for rate sensitivity in the present study, a multiplicative constitutive relation is used. Rewritten to an “additive form”, this may be expressed as [3]:

$$\sigma_{eq}(\boldsymbol{\sigma}) = \sigma_0 + R(p) + \sigma_v(\dot{p}, p) \quad (2-19)$$

where the viscous stress is expressed as [3]:

$$\sigma_v(\dot{p}, p) = (\sigma_0 + R(p)) \left( \left( 1 + \frac{\dot{p}}{\dot{p}_0} \right)^C - 1 \right) \quad (2-20)$$

and  $(C, \dot{p}_0)$  are material parameters describing the strain rate sensitivity.

### Hardening rules

In general, metals work-harden and the strength increases when they are deformed plastically [3]. There exist several different ways to account for work hardening in material models. In this thesis, isotropic work-hardening is assumed for all material models used. Isotropic hardening implies that the yield surface expands in stress space (the elastic region expands) while keeping its shape during plastic straining.

The yield function with isotropic work-hardening is shown in Equation (2-17). The hardening variable  $R$  is a function of the accumulated plastic strain  $p$ . The isotropic work-hardening rule can be expressed as [3]:

$$\dot{R} = h_R \dot{p} \quad (2-21)$$

where  $h_R = h_R(p)$  is the isotropic hardening modulus. As  $\dot{p} = 0$  in the elastic domain, it is seen from Equation (2-21) that work-hardening only occurs for plastic loading. The power law which is a general nonlinear isotropic hardening rule referred to in this thesis, may be expressed as:

$$R = Kp^n \quad (2-22)$$

where  $(K, n)$  are the hardening parameters. Alternatively, the entire flow stress may be expressed by a power expression so that:

$$\sigma_{eq} = Kp^n \quad (2-23)$$

In Equation (2-23),  $K$  is the stress at  $p=1.0$ . Due to its simple mathematical form, this expression is usually not optimal to describe the stress-strain relation when the specimen starts to neck down. However, in engineering applications, it is often used to describe the entire stress-strain relation until fracture for convenience.

#### 2.3.4 Necking

A one-dimensional uniform rod subjected to tension loading is considered.

Necking is a condition of instability in tension and occurs when the deformation due to elongation of the specimen localizes somewhere along the rod length and the cross section area  $A$  within this region decreases rapidly. Necking begins at maximum load when the increase in load-carrying ability of the material due to strain hardening is no longer sufficient to compensate for the continuing reduction in area as the specimen elongates [4].

Maximum load is reached when the incremental value of the engineering stress is equal to zero, i.e.  $d\sigma_e = 0$ . By expressing the incremental value of the engineering stress as a function of the true stress and strain (may be found by rearranging Equation (2-13) and applying the chain rule), it may be shown that necking occurs when:

$$\frac{d\sigma}{d\varepsilon} = \sigma \quad (2-24)$$

After necking has occurred the deformation in the rod is no longer uniform and the relations for stress and strain as presented in 2.3.2 is no longer valid.

The formation of a neck in the tensile specimen introduces a complex triaxial state of stress in that region. The additional radial and transverse stresses raise the value of longitudinal stress that is required to cause plastic flow [4]. For a cylindrical specimen (as the uniform rod), necking is isotropic. However, in a sheet specimen (i.e. rectangular cross section where the width of the specimen is much higher than the thickness), there are two types of tensile instabilities. The first, referred to as diffuse necking, provides a large extent of necking on the specimen similar as for the cylindrical rod. The second instability is referred to as localized

necking. Diffuse necking might terminate in fracture but is normally followed by localized necking. Localized necking is characterized as a narrow band of width equal to the specimen thickness (at initiation of local necking) and with an inclined angle towards the major principal strain direction. More details regarding localized necking and how fracture eventually will occur within the neck is covered in section 2.3.5.

### 2.3.5 Fracture criterions

#### General

Fracture is the separation, or fragmentation, of a solid body into two or more parts under the action of stress [4]. The process can be considered to be made up by two components; crack initiation and crack propagation. Further it can be classified into two general categories, brittle fracture and ductile fracture. In brittle fracture no apparent plastic deformation takes place and it is characterized by a rapid rate of crack propagation. For a ductile fracture, extensive plastic deformation (necking) takes place prior to fracture. Other characteristics for a ductile fracture are slow propagation and the absorption of large amount of energy before fracture (large plastic strains) [4].

The different stages in a ductile fracture for the previously considered rod in tension are shown in Figure 2-5.

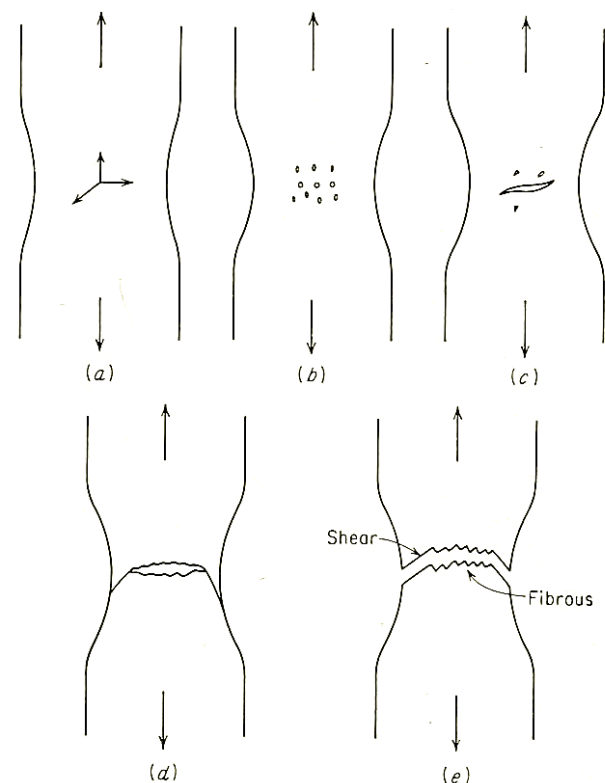


**Figure 2-5: Stages in the formation of a cup-and-cone fracture [4]: (a) Necking. (b) Forming of cavities. (c) Cavities coalesce. (d) Crack propagation. (e) Separation.**

### Predicting crack initiation and crack propagation numerically

Various approaches exist for predicting fracture initiation and fracture propagation numerically. The failure criteria in problems involving ductile materials typically express the deterioration of the material by an accumulative damage variable. Especially for solid elements several successful approaches can be found in the literature. By using several elements over the thickness of a plate the fracture initiation and propagation may be simulated in a detailed manner. Examples are the evaluation of uncoupled ductile fracture criteria for the dual-phase steel Docol 600DL as performed by Gruben et al. [17] or the evaluation of fracture criterions in projectile impact of steel plates performed by Dey et al. [19].

Fracture in sheet metal is often preceded by excessive plastic flow in narrow bands, characterized as local necks. The fracture criteria used in the present study is referred to as the Cockcroft and Latham (CL) fracture criterion and the Bressan-Williams-Hill (BWH) instability criterion. The CL criterion is a simple general criterion which also is applicable for solid elements. The BWH instability criterion gives a simplified way of determining the onset of local necking in sheet metal and is suitable for shell elements.

### The Bressan-Williams-Hill instability criterion

In an impact analysis of large-scale shell-structures it is convenient to consider the onset of local necking as a state of failure, rather than searching for fracture after local necking has occurred. The major reason for this is that in large-scale shell structures the characteristic length of the elements has to be considerable larger than the shell thickness in order to have an economical reasonable analysis in terms of computational time. The evolution of a neck cannot be followed when having a coarse mesh. The BWH criterion [8] gives a simplified way of determining the onset of local necking. The BWH criterion is a combination of Hill's local necking criterion [21] and the Bressan and Williams shear stress criterion [22]. The derivation of the BWH instability criterion will be presented in detail as this is not a typical well established method found in textbooks etc. The derivation of the criterion is obtained from the paper by Alsos et al. [8]. However, some of the formulas are derived in a more detailed manner than in the above mentioned paper.

Forming limit diagrams (FLD), where the principal strains  $(\varepsilon_1, \varepsilon_2)$  at incipient plastic instability are plotted as forming limit curves (FLC), has been the dominating method for estimating failure for metal sheets in industrial forming processes for a long time. Proportional strain paths are assumed when generating such diagrams, i.e. the ratio between the minor and major principal strain,  $\beta = d\varepsilon_2 / d\varepsilon_1$ , is constant. However, due to various effects such as material hardening, geometry changes and contact, the loading path may alter, i.e. we get non-proportional strain paths with a resulting change in the FLD. A way of circumventing this problem is to introduce stress based forming limit curves. The basic idea is that a stress based criteria remains more or less unaffected by altered strain paths. The assumptions on the stress based forming limit approach can be summarized as:

- Plane stress condition is assumed.
- $J_2$  flow theory is assumed.
- The yield function and the potential for plastic flow are assumed identical, and the relations between strain rates and stresses can be found from the associated flow rule.
- Elastic strains are neglected.
- Proportional loading is assumed at the final stage just prior to the instability, thus used in the derivation of the criterion. Otherwise non-proportional loading is allowed for.

As the associated flow rule is adopted, refer to Equation (2-15), the ratio of the strain increments will be the same as the ratio of the deviatoric stresses [5], i.e.

$$\frac{d\varepsilon_1}{\sigma'_1} = \frac{d\varepsilon_2}{\sigma'_2} = \frac{d\varepsilon_3}{\sigma'_3} \quad (2-25)$$

or

$$\frac{d\varepsilon_1}{2-\alpha} = \frac{d\varepsilon_2}{2\alpha-1} = \frac{d\varepsilon_3}{-(1+\alpha)} \quad (2-26)$$

where  $\alpha = \sigma_2 / \sigma_1$ , i.e. ratio between the minor and major principal stress.

If a material is deforming in plane stress in a proportional process, Equation (2-26) can be integrated and expressed in terms of the strains [5], i.e.

$$\frac{\varepsilon_1}{2-\alpha} = \frac{\varepsilon_2}{2\alpha-1} = \frac{\beta\varepsilon_1}{2\alpha-1} = \frac{\varepsilon_3}{-(1+\alpha)} = \frac{-(1+\beta)\varepsilon_1}{-(1+\alpha)} \quad (2-27)$$

In the derivation above it is used that  $\varepsilon_3 = -\varepsilon_1(1+\beta)$  which is valid considering volume conservation and proportional strain paths. From Equation (2-27), we obtain the relation between the stress and strain ratios:

$$\alpha = \frac{1+2\beta}{\beta+2} \quad (2-28)$$

Examples of strain based FLD and stress based FLD is shown in Figure 2-6. As seen from the figure the stress based FLC remains more or less fixed in stress space for non-linear strain paths, while the strain based FLC varies for different combinations of non-proportional strain paths.

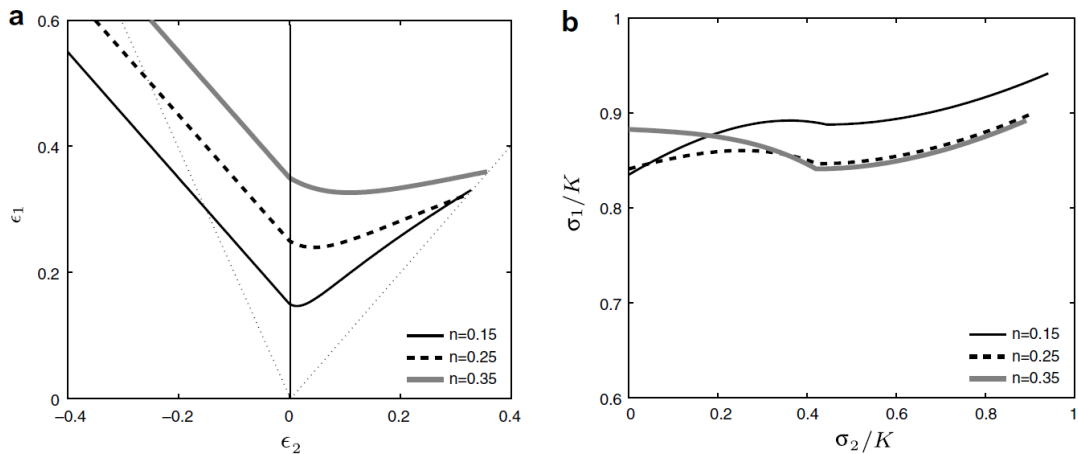


**Figure 2-6: Forming limit diagrams: (a) in strain space, (b) in stress space. Both figures illustrate the same materials.  $K$  and  $n$  refers to power law parameters. [8]**

Hill's local necking criterion:

Hill's analysis [21] shows that a local neck will form with an angle  $\phi$  to the direction of the major principal stress as a function of the strain rate ratio  $\beta$ , see Equation (2-29):

$$\phi = \tan^{-1} \sqrt{-\beta} \quad (2-29)$$

At the angle  $\phi$ , the neck is in plane strain, i.e. the normal strain along the neck is zero. At the instant a local neck is formed, the effects from strain hardening and the reduction in thickness balance each other exactly. This gives traction increments within the material equal to zero,  $dT_1 = 0$ , at the point of necking. The following expression for local necking may be derived by differentiating the expression for the major principal tension in the sheet,  $T_1 = \sigma_1 t$ , where  $t$  is the thickness of the element [5].

$$\frac{dT_1}{T_1} = \frac{d\sigma_1}{\sigma_1} + \frac{dt}{t} = \frac{d\sigma_1}{\sigma_1} + d\varepsilon_3 = \frac{d\sigma_1}{\sigma_1} - (1 + \beta)d\varepsilon_1 = 0 \quad (2-30)$$

In the derivation above it is used that  $d\varepsilon_3 = -d\varepsilon_1(1 + \beta)$  as we have volume conservation.

The von Mises stress for plane stress may be expressed as [5]:

$$\sigma_{eq} = \left( \sqrt{1 - \alpha + \alpha^2} \right) \sigma_1 \quad (2-31)$$

Further it is assumed that the material stress-strain curve follows a Power law expression,  $\sigma_{eq} = K\varepsilon_{eq}^n$ , where  $(K, n)$  are material parameters and  $(\sigma_{eq}, \varepsilon_{eq})$  are equivalent stress and strain. The major principal stress may then be expressed as:

$$\sigma_1 = \frac{K\varepsilon_{eq}^n}{\sqrt{1 - \alpha + \alpha^2}} \quad (2-32)$$

The equivalent strain increment may be expressed as [5]:

$$\begin{aligned} d\varepsilon_{eq} &= \left[ \frac{2}{3} (d\varepsilon_1^2 + d\varepsilon_2^2 + d\varepsilon_3^2) \right]^{1/2} \\ &= \left[ \frac{2}{9} \left( (d\varepsilon_1 - d\varepsilon_2)^2 + (d\varepsilon_2 - d\varepsilon_3)^2 + (d\varepsilon_3 - d\varepsilon_1)^2 \right) \right]^{1/2} \end{aligned} \quad (2-33)$$

Further the equivalent strain increment may be expressed in terms of the major principal strain increment and the strain ratio as [5]:

$$d\varepsilon_{eq} = \sqrt{\frac{4}{3} (\beta^2 + \beta + 1)} d\varepsilon_1 \quad (2-34)$$

By using Equation (2-30), (2-32) and (2-34), the following expression for the equivalent strain at local necking is found:

$$\begin{aligned}
\frac{d\sigma_1}{d\varepsilon_1} &= \frac{\partial\sigma_1}{\partial\varepsilon_{eq}} \frac{\partial\varepsilon_{eq}}{\partial\varepsilon_1} = \sigma_1(1+\beta) \\
\frac{nK\varepsilon_{eq}^{n-1}}{\sqrt{1-\alpha+\alpha^2}} \frac{\partial\varepsilon_{eq}}{\partial\varepsilon_1} &= \frac{K\varepsilon_{eq}^n}{\sqrt{1-\alpha+\alpha^2}}(1+\beta) \\
\Rightarrow \varepsilon_{eq} &= \frac{n}{(1+\beta)} \frac{\partial\varepsilon_{eq}}{\partial\varepsilon_1} = \frac{2n}{\sqrt{3}} \frac{\sqrt{\beta^2+\beta+1}}{1+\beta}
\end{aligned} \tag{2-35}$$

This gives the equivalent stress at local necking:

$$\sigma_{eq} = K \left( \frac{2\tilde{n}}{\sqrt{3}} \frac{\sqrt{\beta^2+\beta+1}}{1+\beta} \right)^n \tag{2-36}$$

The power law exponent in the expression for the equivalent strain is indicated with a tilde ( $\tilde{n}$ ) as it may be given element size dependent qualities. This will be further described later on.

This result in the following expression for the major principal stress:

$$\begin{aligned}
\sigma_1 &= \frac{\sigma_{eq}}{\sqrt{1-\alpha+\alpha^2}} \\
\Rightarrow \sigma_1 &= \frac{2K}{\sqrt{3}} \frac{1+\frac{1}{2}\beta}{\sqrt{\beta^2+\beta+1}} \left( \frac{2}{\sqrt{3}} \frac{\tilde{n}}{1+\beta} \sqrt{\beta^2+\beta+1} \right)^n
\end{aligned} \tag{2-37}$$

From Equation (2-29) it is noted that the expression for the angle  $\phi$  only yields reasonable results for negative values of  $\beta$ . It follows that the Hill's local necking criterion only yields rational results for a tension-compression strain state.

Bressan-Williams shear criteria:

For positive values of  $\beta$  (i.e. a tension-tension strain state), a different approach is needed. The main mechanism of plastic deformation is slip arising from shear on certain preferred combinations of crystallographic planes and directions. In the paper by Bressan and Williams [22], it is mentioned that experimental observations shows that the fracture planes in sheet metal lies in a direction near to that of maximum shear stress. These observations suggest that the application of a shear criterion may be useful in determining the onset of local necking in a shell type structure. The basis for the Bressan-Williams shear criterion follows three main assumptions.

1. The shear instability is initiated in the direction through the thickness at which the material element experiences no change in length.
2. Instability is initiated by a local shear stress which exceeds a critical value.
3. Elastic strains are neglected (small compared to the plastic strains at local necking).

An illustration of local shear instability in a material element is shown in Figure 2-7a. It is seen from the figure that there is no elongation of the material in the  $x_1$  direction. This indicates that the strain increment  $d\varepsilon_1$  equals zero.

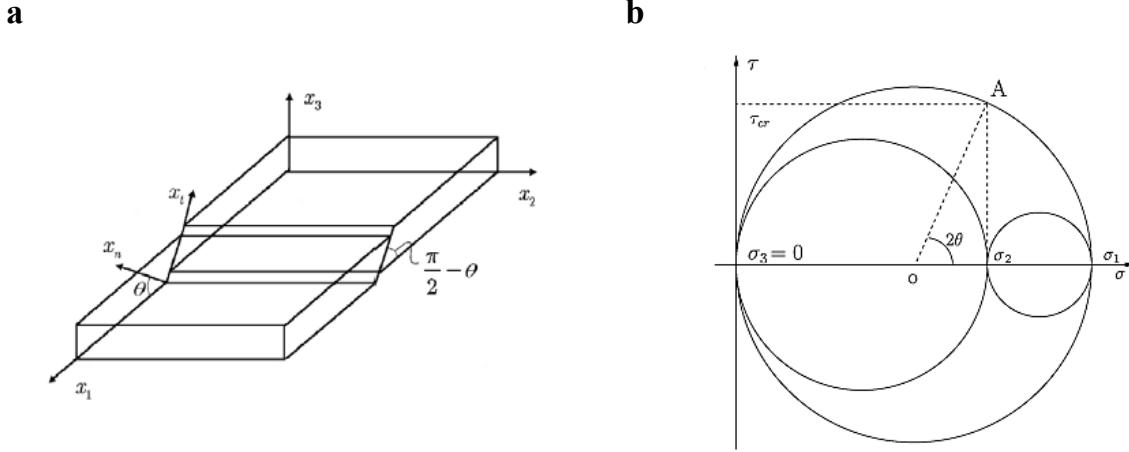


**Figure 2-7: (a) Local shear instability in a material element. (b) Mohr's circle for the state of stress at the onset of necking. [8]**

Additionally as illustrated in Figure 2-7a, the shear plane forms an angle  $\pi/2 - \theta$  to the element horizontal plane. Considering this, we have the following relationship between the angle of the inclined plane and the principal strains (may be found from the analysis of a Mohr's circle for the strain increments).

$$d\varepsilon_1 = \frac{d\varepsilon_1 + d\varepsilon_3}{2} + \frac{d\varepsilon_1 - d\varepsilon_3}{2} \cos 2\left(\theta + \frac{\pi}{2}\right) = 0 \quad (2-38)$$

As  $\cos 2(\theta + \pi/2) = -\cos 2\theta$ , we may write

$$\cos 2\theta = \frac{d\varepsilon_1 + d\varepsilon_3}{d\varepsilon_1 - d\varepsilon_3} \quad (2-39)$$

Assuming volume constancy,  $d\varepsilon_3 = -d\varepsilon_1(1 + \beta)$ , the angle  $\theta$  can be expressed as a function of the strain ratio  $\beta$

$$\cos 2\theta = -\frac{\beta}{2 + \beta} \quad (2-40)$$

From the Mohr's circle for the state of stress at onset of necking as shown in Figure 2-7b, one might find the following relation between the inclined plane and the stresses involved

$$\tau_{cr} = \frac{\sigma_1}{2} \sin 2\theta \quad (2-41)$$

where  $\tau_{cr}$  is the critical shear stress. By combining Equation (2-40) and (2-41) we get the expression that gives the Bressan-Williams criterion



$$\sigma_1 = \frac{2\tau_{cr}}{\sqrt{1 - \left(\frac{\beta}{2 + \beta}\right)^2}} \quad (2-42)$$

The critical shear stress is a value that may be calibrated at plane strain, i.e.  $\beta = 0$  [8]. If calibrated from Hill's expression at plane strain given in Equation (2-37), the critical shear stress takes the form

$$\tau_{cr} = \frac{K}{\sqrt{3}} \left( \frac{2}{\sqrt{3}} \tilde{n} \right)^n \quad (2-43)$$

The Bressan-Williams criterion is indented for positive values of the strain rate ratio (biaxial stretching) [22]. The validity of the expression as a fracture criterion for negative values of the strain rate ratio becomes questionable [8].

Bressan-Williams-Hill criterion:

To summarize, the BWH criterion uses Hill's instability criteria for negative values of  $\beta$  and the Bressan-Williams shear criteria for positive values of  $\beta$ . The resulting expression for the major principal stress at incipient instability yields:

$$\sigma_1 = \begin{cases} \frac{2K}{\sqrt{3}} \frac{1 + \frac{1}{2}\beta}{\sqrt{\beta^2 + \beta + 1}} \left( \frac{2}{\sqrt{3}} \frac{\tilde{n}}{1 + \beta} \sqrt{\beta^2 + \beta + 1} \right)^n, & \text{if } \beta \leq 0 \\ \frac{2K}{\sqrt{3}} \frac{\left( \frac{2}{\sqrt{3}} \tilde{n} \right)^n}{\sqrt{1 - \left( \frac{\beta}{2 + \beta} \right)^2}}, & \text{otherwise} \end{cases} \quad (2-44)$$

For additional information on the BWH instability criteria than what is presented herein it is referred to the paper on sheet metal instability by Alsos et al. [8].

Accounting for element size sensitivity when using BWH criterion:

A coarse mesh might not detect the proper stress concentration. This is especially the case in zones with large strain gradients typically present at structural intersections, e.g. close to a stiffener. A consequence of this might be that the BWH criterion predicts instability too late, thus leading to non-conservative results. In order to get a robust failure response of coarsely meshed shell structures, a mesh scaling rule to overcome the shortcomings of a too coarse mesh is required.

If the flow curve for a material is given by the power law of Equation (2-23), it may easily be shown that necking occurs for a strain equal to the strain-hardening coefficient  $n$  when considering uniaxial tension. Hill's analysis would give the equivalent plastic strain at onset of necking equal to  $2n$  in uniaxial tension (found by inserting  $\beta = -0.5$  into Equation (2-35)).

In the paper on the resistance to penetration of stiffened plates by Alsos et al. [7], the following geometric scaling of  $\tilde{n}$  in Equation (2-44) is proposed:

$$\tilde{n} = \frac{n}{2} \left( \frac{t_e}{l_e} + 1 \right) \quad (2-45)$$

where  $t_e$  is the element thickness and  $l_e$  is the element length measured at the initial condition of the element. This implies that as the thickness/length ratio is approaching zero, the equivalent plastic strain at local necking approaches  $\tilde{n}$ , i.e. the same as the necking strain.

This is a simple approach, implemented with success in the numerical analysis of stiffened steel panel indentation tests reported in the above mentioned paper.

With this scaling rule, a coarse mesh will reduce the critical stress in Equation (2-44). It should be noted that, in a case where stress concentrations are properly captured by the coarse mesh, the proposed mesh scaling rule, will underestimate the stress at instability, thus trigger instability too early. This scaling of the critical stress will be referred to as geometric scaling when used in the remaining part of this report.

#### Cockcroft and Latham fracture criterion

Cockcroft and Latham [20] proposed a very simple fracture criterion based on a combination of stress and strain and not on either of these quantities separately. The criterion was originally based on total plastic work per unit volume, but was later modified to account for the influence of hydrostatic tension stress (the equivalent stress in the plastic work equation depends only on the deviatoric stress). The concept is that damage accumulates during straining and fracture is reached when the energy measure per unit volume  $W_1$  reaches a critical value  $W_{cr}$ . The measure  $W_1$  is defined as

$$W_1 = \int_0^p \langle \sigma_1 \rangle dp \leq W_{cr}, \quad \langle \sigma_1 \rangle = \max(\sigma_1, 0) \quad (2-46)$$

where  $\sigma_1$  is the major principle stress. The value of the equivalent plastic strain at  $W_{cr}$  is referred to as the failure (or fracture) strain.

With the above formulation, fracture will depend both on shear stresses (that gives rise to plastic deformation and work hardening) and on the tensile stresses. The CL criterion requires only one simple tensile test in order to determine the material constant  $W_{cr}$ . Where the BWH criterion defines onset of local necking as failure, the CL criterion will allow the neck to evolve before the failure criterion is reached. The drawback when using the CL criterion on shell structures is that it becomes computational demanding as it requires a high number of small elements. The characteristic initial width of a local neck equals the thickness of the plate. For the evolution of a neck to be captured in a simulation using 4-node shell elements, the element characteristic length should be approximately equal to the plate thickness.

### 3 MATERIAL PROPERTIES

#### 3.1 Material tests

##### 3.1.1 General

Tension tests are performed in order to provide the necessary information on the strength and ductility of the steel material used in the plate components subjected to loading in the present study. The plate delivery was accompanied by a certificate stating its mechanical properties and chemical composition. The material used is of steel grade DOMEX 355 MC E. DOMEX 355 MC E is a hot-rolled structural steel with minimum yield strength of 355MPa and the material displays good welding, cold forming and cutting performance. Three flat tension specimens were cut out, parallel to the rolling direction, from a 3mm thick plate. The nominal geometry of the tension specimen is shown in Figure 3-1.

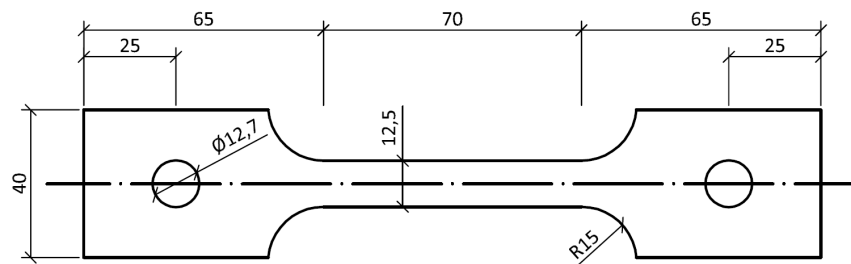


**Figure 3-1: Standard nominal geometry of the specimen [mm].**

The actual width ( $b$ ) and thickness ( $t$ ) were measured at the end of the gauges and at the midpoint by using a micrometer. The measurements revealed no variations in the gauge area when considering a precision of two decimals after comma. The measured values for the three specimens are shown in Table 3-1.

**Table 3-1: Measured geometry of gauge area.**

Specimen	$b$ [mm]	$t$ [mm]
1	12.58	3.02
2	12.57	3.02
3	12.58	3.02

##### 3.1.2 Test set-up

The tests were performed by using *Instron 5982* test machine which has a capacity of 100kN. The tests were run at a crosshead velocity of 5mm/min, corresponding to a strain rate of:

$$\dot{\epsilon} = \frac{\text{crosshead speed}}{\text{gauge length}} (\text{s}^{-1}) = 1.2 \cdot 10^{-3} \text{s}^{-1}$$

within the 70mm long gauge area.

A clip-on extensometer was used to measure the change in length to be used in strain calculations. The distance between the clips of the extensometer was 37.5mm. In addition a camera was set up to record images while the test specimen was loaded to allow Digital Image Correlation (DIC) to be used. DIC is a tool than can be used for measurements of displacements and strain fields based on analysis of recorded digital images. The eCorr DIC software [39] developed at SIMLab, NTNU will be used. The user places a mesh on the image to mark the area from where information should be collected.

The images from the camera recording (one each second) were logged together with time, force, cross-head displacement measured by the test machine and displacement measured by the extensometer. The test set-up is shown in Figure 3-2.

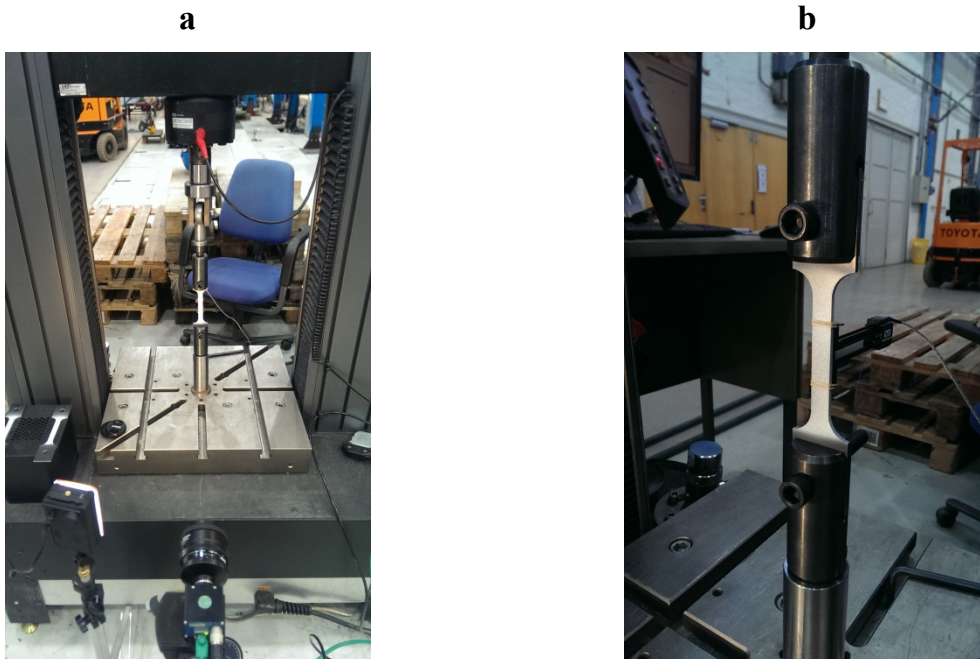


**Figure 3-2: Material test set-up. (a) shows the specimen installed in the test rig with the camera in the lower part of the picture. (b) shows a close up view of the installed specimen with an attached clip-on extensometer.**

### 3.1.3 Test results

The test samples were pulled in tension until fracture occurred. For all three tests, fracture occurred approximately at the midpoint and the crack was perpendicular to the longitudinal direction (not inclined with an angle in a narrow band as could have been the case if the width/thickness ratio was higher, refers to section 2.3.4).

Based on the data recorded relevant material properties have been identified and are shown in Table 3-2. As measurements of the elastic modulus,  $E$  and Poisson's ratio,  $\nu$  requires special procedures, and considering that these values is only slightly affected by alloying conditions, heat-treatment, cold-rolling etc., the steel nominal values of  $E=210\ 000\text{MPa}$  and  $\nu = 0.33$  is used. The tabulated value of the elongation corresponds to the engineering strain within the uniform gauge length at maximum force.

**Table 3-2: Measured material properties.**

	Mean value	Std. Dev.
Yield stress, $f_y$ [MPa]	404	2.2
Ultimate stress, $f_u$ [MPa]	478	0.6
Elongation, $\epsilon_u$ [%]	20	0.4

DIC analysis was performed for each tensile test in order to generate engineering stress-strain curves until fracture and to calculate the elongation at maximum force. Figure 3-3a and b shows a vector drawn on the undeformed and deformed mesh at maximum force for tensile specimen 2. Figure 3-3c shows the specimen just prior to fracture. By measuring the vector elongation throughout the test, an engineering stress-strain curve could be established. The initial length of the vector is similar for all three specimens (600 pixels, estimated to be 28.2mm) assuring the curves are comparable. The extensometer measurements (extensometer was removed just prior to maximum force) were only used as a validation of the results from DIC analysis. By comparing engineering stress strain curves from DIC analysis with those obtained with measurements from the extensometer, a very good agreement is found.

The engineering stress strain curves are shown in Figure 3-4. The curves have been corrected for the nominal elastic modulus. As seen from Figure 3-4b the yield plateau ends approximately at the same magnitude of engineering strain for all three tests. The yield stress for each test specimen was determined based on the average stress of 5 data points approximately evenly distributed within the yield plateau.

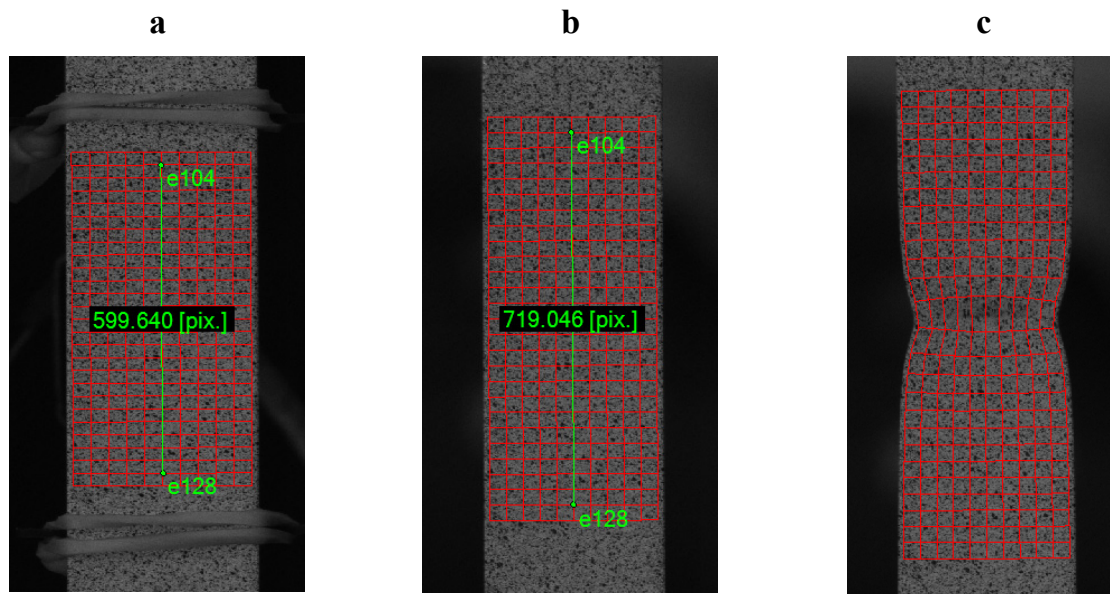


**Figure 3-3: Results from tension tests - DIC analysis of test 2: (a) shows a vector drawn on the undeformed mesh. (b) shows the elongated vector at maximum force. (c) shows the deformed mesh just prior to fracture.**

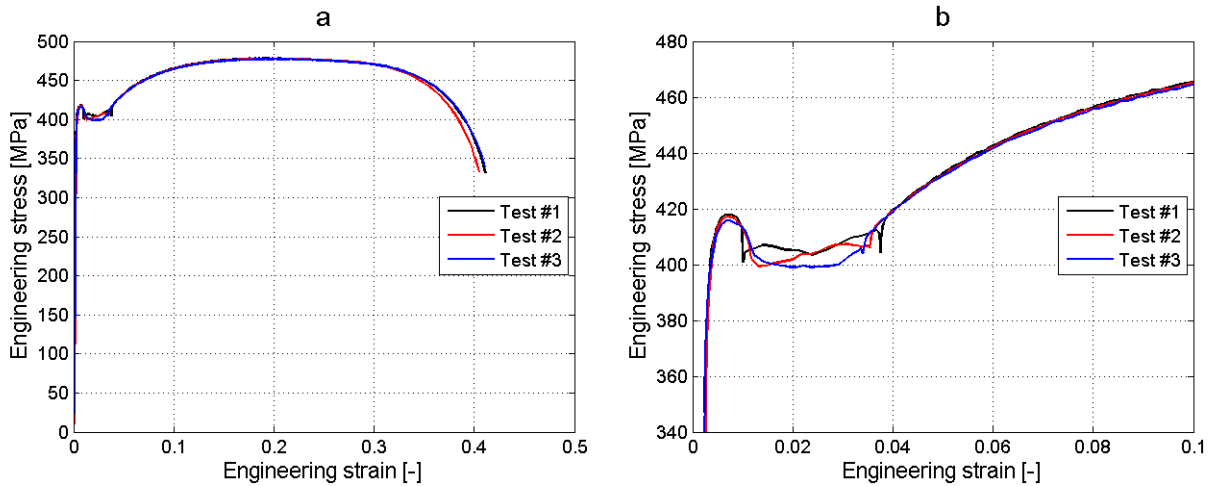


**Figure 3-4: Results from tension tests: (a) shows the engineering stress-strain curves based on DIC analysis, while (b) shows a close up view of the yield plateaus of the same curves.**

## 3.2 Material models

### 3.2.1 General

Based on the information obtained from the material tests reported in section 3.1, two material models have been created. The first material model (MAT1a) is based on a power law expression that includes a yield plateau, while the second (MAT1b) is a strain rate sensitive version of the first one. The material models have been curve fitted to the true stress-strain curve from tension tests up to maximum force that marks the end of the uniform straining of the gauge length (engineering strain of approximately 20%). As described in section 2.3.3 the power expression is usually not optimal for the phase after the specimen begins to neck down. However, as an engineering approach, the material curves are extrapolated based on the defined mathematical expression. This is considered to produce sufficiently accurate results for the present study.

An evaluation of the material models accuracy and the approach to determine the strain rate sensitivity parameters will be shown in section 3.2.2, where a tension test is simulated with the finite element method.

As shown in Figure 3-4 the results from the three tension tests are similar. Both material models have been based on results from tension test 2. This test was chosen as the yield stress calculated was closest to the mean yield stress. Detailed description of the material models is given in Table 3-3. Figure 3-5a shows the power law model curve fitted to the tension test, while Figure 3-5b shows true stress-plastic strain curves for MAT1a and MAT1b for a few chosen values of the plastic strain rate. For both material definitions, the steel density  $7.85 \text{ tonnes/m}^3$ , and the steel elastic properties in terms of a Young's modulus of  $210000 \text{ MPa}$  and a Poisson's ratio of  $0.33$  is utilized.

**Table 3-3: Material models – Overview.**

Material name	Description
MAT1a	<p>Elastic-plastic with isotropic hardening:</p> <ul style="list-style-type: none"> <li>The equivalent stress-strain relationship is represented by a modified power law formulation that includes a yield plateau.</li> </ul> $\sigma_{eq} = \begin{cases} \sigma_0 & \text{if } p \leq \varepsilon_{plat} \\ K(p + \varepsilon_0)^n & \text{otherwise} \end{cases}$ <p>where <math>\varepsilon_{plat}</math> is the equivalent plastic strain at the plateau exit. The strain <math>\varepsilon_0</math> allows the plateau and power law expression to intersect at <math>(\varepsilon_{plat}, \sigma_0)</math> and is obtained by:</p> $\varepsilon_0 = \left(\frac{\sigma_0}{K}\right)^{\frac{1}{n}} - \varepsilon_{plat}$ <p>The constants are: <math>\sigma_0 = 404\text{MPa}</math>, <math>K = 772\text{MPa}</math>, <math>n = 0.1733</math>, <math>\varepsilon_{plat} = 0.024</math></p>
MAT1b	<p>Elastic-viscoplastic with isotropic hardening:</p> <ul style="list-style-type: none"> <li>Multiplicative constitutive relation, refer to Equation (2-19) and (2-20). The flow stress described by the modified power law formulation in MAT1a is extended with a viscous stress and is defined as</li> </ul> $\sigma_{eq} = \begin{cases} \sigma_0 \left(1 + \frac{\dot{p}}{\dot{p}_0}\right)^C & \text{if } p \leq \varepsilon_{plat} \\ K(p + \varepsilon_0)^n \left(1 + \frac{\dot{p}}{\dot{p}_0}\right)^C & \text{otherwise} \end{cases}$ <p>The additional constants are: <math>C = 0.01</math> and <math>\dot{p}_0 = 0.0025\text{s}^{-1}</math>.</p>

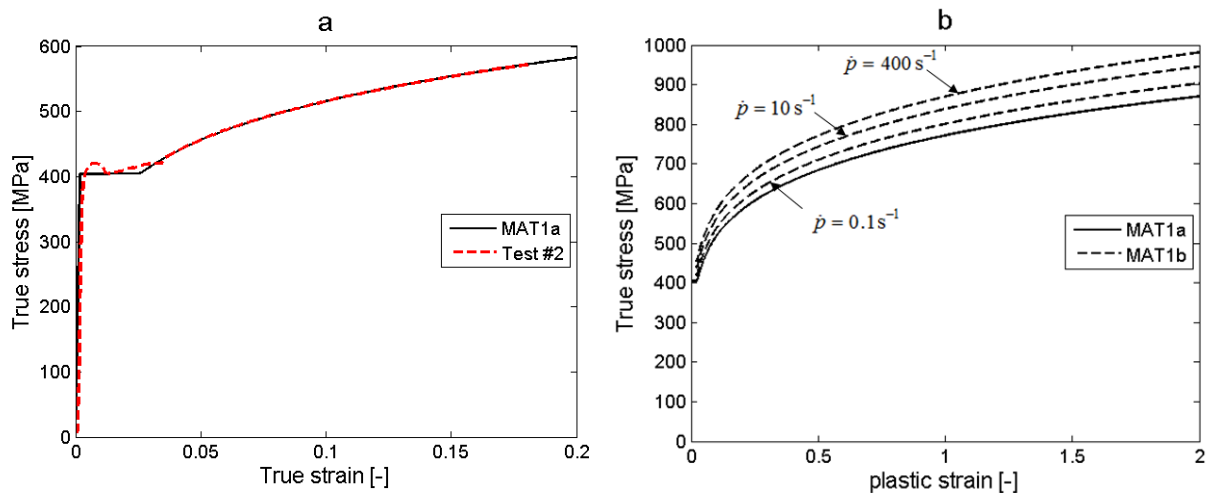


**Figure 3-5: Material models: (a) shows the power law model curve fitted to tension test 2, while (b) shows the true stress-plastic strain relations.**

### 3.2.2 Validation of material models

#### General

As mentioned in section 3.2.1, the material models were curve fitted to test results up to maximum force (20% engineering strain). In the numerical simulations of the stiffened steel plates subjected to impact loading, strains are expected to be significant higher, thus the curves are extrapolated. As an evaluation of the accuracy of the material models, and in order to estimate  $W_{cr}$  in the Cockcroft and Latham fracture criteria, tension test 2 was simulated using Abaqus.

#### FE-model

A FE-model with the standard tension test specimen geometry as shown in Figure 3-1 is utilized. The main part of the input file used to create the FE-model is based on a standard input file that is used in the research work at SIMLab, NTNU, and which is not created during the present study. The FE-model is shown in Figure 3-6.

One symmetry plane is utilized and only half the thickness is modeled (1.5mm). The mesh consists of a total of 80130 C3D8R elements. C3D8R is an 8-node, linear brick element with reduced integration and hourglass control. The mesh density is very high at the center of the gauge area, and less dense towards the specimen ends. In each of the specimen pin holes, an analytical rigid surface is created simulating the pin. One of the analytical surfaces is fixed for all DOF's (indicated as BC1 on Figure 3-6). The other analytical surface is fixed for all DOF's except y-direction (indicated as BC2 on Figure 3-6). In the interface between the analytical rigid surfaces and the deformable solid elements, contact formulations are assigned and a friction coefficient of zero is specified in the tangential direction. In order to compare numerical and experimental results, a set containing two nodes at approximately the same location as the DIC vector is created. These are located 28.2mm apart and are indicated in Figure 3-6 (reference nodes).

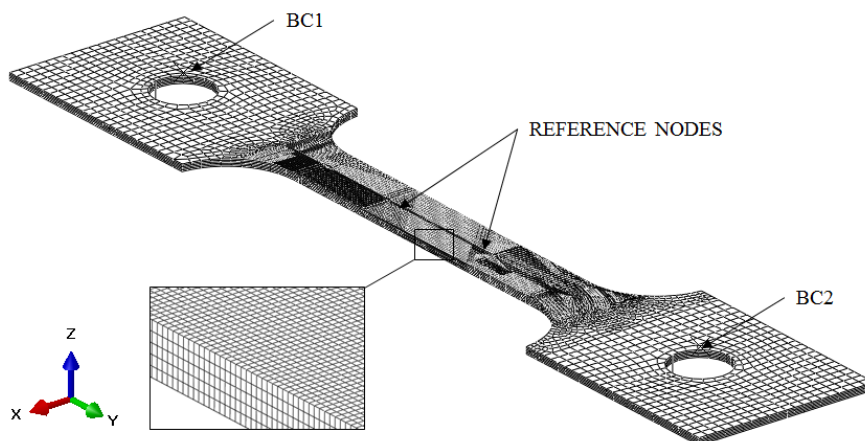


**Figure 3-6: FE-model of the tension test specimen.**



### Analysis results and approach to determine strain rate parameters

Non-linear static simulations are performed. A displacement of 22mm in positive y-direction is specified at the analytical surface simulating the pin at the location of BC2, refer to Figure 3-6.

First, an analysis using the elastic-plastic material model (MAT1a) is reported. Figure 3-7a shows the results in the way of engineering stress-strain from the FEA with the material model MAT1a compared against the tension test. The elongation from the FEA is extracted from two nodes that correspond to the vector length from DIC analysis as described previously. By inspecting the results, it is seen that the FEA accurately reproduce the tension test up to maximum force. However, when the specimen gauge area starts to neck down, the force drops faster in the FEA than what was observed in the tension test. An explanation may be that strain rate effects probably were present in the last phase of the test (during necking). Even if the tension test were run at a slow speed, a slight increase of the flow stress due to strain rate effects causes the evolution of the neck to be postponed. Further, the power law equation that describes the stress-strain relation up to necking accurately, does not perfectly describe the stress-strain relation during the last phase of the strain hardening. The deviation is most likely due to a combination of the above mentioned explanations, with the heaviest influence from strain rate effects.

Based on the assumption made regarding strain rate effects present in the tension tests, the rate parameters shown in Table 3-3 were established in an iterative way. I.e. the rate parameters were modified until the engineering stress-strain curve from the FEA moved as close as possible to the engineering stress-strain curve from the test. When performing analysis with strain rate sensitivity, the real time period from the tension test (275sec) was specified.

Figure 3-7b shows the results from the FEA with material model MAT1b compared against the tension test. As seen from the figure, the engineering stress-strain after necking from the FEA is now closer to the measured values from the experiment. It is underlined that more correct information on the rate parameters may be determined by performing tension tests at elevated strain rates. However, for the present study the rate parameters based on the simplified method reported herein will be used. When implementing the strain rate sensitive material model in the validation phase of the present study, it will be checked that the model gives conservative estimates on the additional strength due to strain rates. Similarly, the reduced ductility due to higher strain rate sensitivity than estimated will be considered.

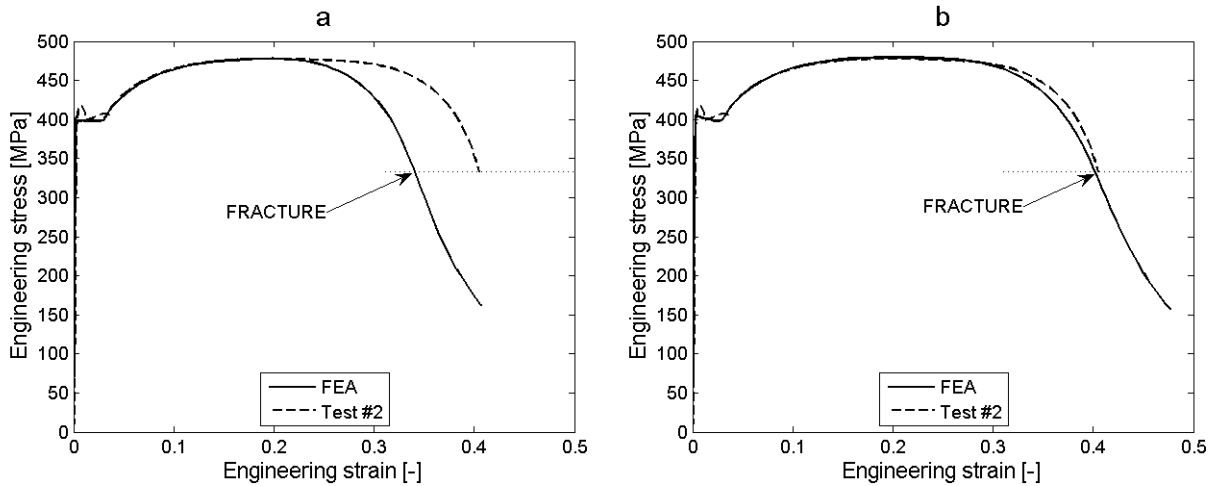


**Figure 3-7: FEA compared against tension test 2: (a) shows the power law model (MAT1a), while (b) shows the same model extended with strain rate sensitivity (MAT1b).**

### 3.2.3 Determination of $W_{cr}$ in CL fracture criterion

In order to estimate a reasonable value for the critical energy measure per unit volume that defines the CL criterion,  $W_{cr}$ , refer to Equation (2-46), the curve from the analysis should be as close as possible to the test results all the way until fracture. It is difficult to modify the constants of the Power law to achieve this, due to the simple form of the mathematical expression. But as discussed above, the material model extended to account for strain rate sensitivity (MAT1b) predicts the stress-strain course of the tensile test satisfactorily until fracture.

From Equation (2-46) it is seen that  $W_I$ , that should reach  $W_{cr}$  at fracture, is defined as the integral of the major principal stress over the plastic equivalent strain. The integral upper limit is set as the load level at fracture in the tests (indicated with a dotted line in Figure 3-7, omitting the further deformation that occurs for a load level below this line in the FEA). In order to calculate  $W_{cr}$ , the required data is extracted from the integration point of the most onerous loaded element in the analysis. The most onerous loaded element is assumed to be located in the geometrical center of the neck. Four elements as shown in Figure 3-8 is chosen for further analysis, and the maximum  $W_I$  resulting from these elements is taken as  $W_{cr}$ .

For the analysis with the rate independent material model (MAT1a), the calculated value  $W_{cr}$  is found to be approximately 1450 MPa, while for the rate dependent material model (MAT1b),  $W_{cr}$  is found to be approximately 1109 MPa. The  $W_{cr}$  value from the rate dependent approach is the most correct one as this originates from the analysis that best fits the experiments, thus the value that will be used when predicting fracture with the CL criterion in the numerical simulations of the stiffened steel plates.

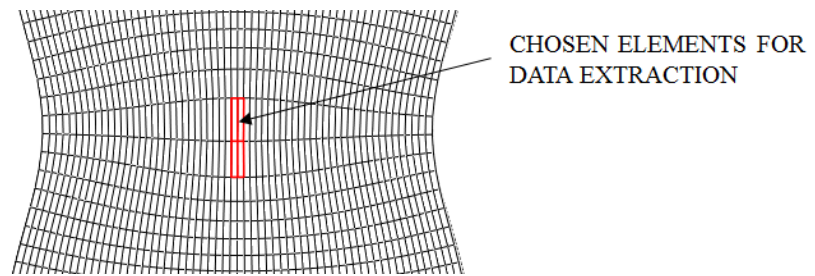


Figure 3-8: Critical elements within the neck.

### 3.2.4 Stress based forming limit diagram according to BWH criterion

Based on the established power law constants  $K$  and  $n$ , the stress based forming limit curve according to BWH instability criterion in Equation (2-44) can be calculated. The diagram is shown in Figure 3-9. Tabulated values of the FLC will be used when implementing the BWH instability criterion in the numerical simulations of the stiffened steel plates.

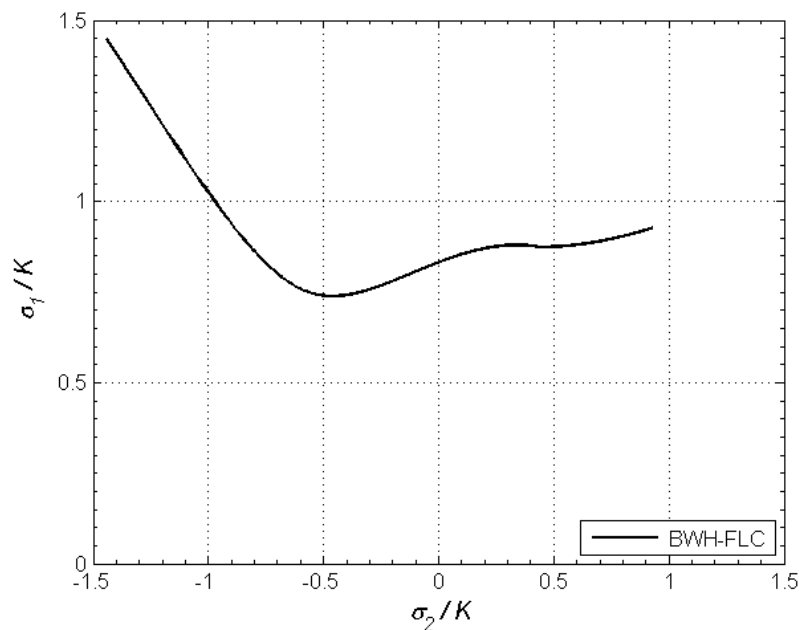


Figure 3-9: Stress based FLD.



## **4 DESIGN AND SET-UP OF COMPONENT TESTS**

### **4.1 General**

Experimental tests of stiffened steel panels subjected to loading from a concentrated load were carried out in the present study. Both quasi-static tests and dynamic tests were conducted. The quasi-static tests were performed to study the relationship between the dynamic impact behaviour and the corresponding static ones. In addition, the quasi-static tests were used as a reference when determining impact energies appropriate for the dynamic tests.

A considerable amount of time and effort was spent on the design of the tests. The major choices regarding the design included support conditions, plate size, contact area between the load and the plate and the size of the load. In this chapter the initial considerations made regarding model selection will be discussed. Next, the details on the test specimen, support conditions and the indenter used to create the concentrated load will be presented. Further, a summary of the design history will be given. Next, preliminary analyses that were performed prior to the execution of the tests are reported. Finally the experimental set-up and test program will be presented.

### **4.2 Initial considerations and model selection**

When designing the tests, the experimental set-up used in similar research work was studied. Both the experimental set-up used by Alsos et al. [6] and Liu et al. [11] was considered. In both these cases the test specimen, which is a stiffened steel panel, is welded to a strong steel frame. This solution is a good approach when the aim is to simulate local indentation of a single panel in the ship's hull. In this situation, longitudinal and transverse girders remain undamaged. The strong steel frame in this set-up, assures that a significant in-plane restriction is imposed on the stiffened panel, similar as would be the case in the real situation. Further, this could have been a good approach for the present study as the geometry of a topside deck structure might resemble that of a ship's hull, with stiffened panels continuously welded on top of longitudinal and transverse girders.

Simultaneously as the present study, there was a separate on-going master thesis by two students regarding the impact behaviour of stiffened aluminium plates. Due to similarities in the scope of work regarding tests in the laboratory, it was reasonable to collaborate with the above mentioned students in the design of the tests. Most importantly the aim was to have a common set-up of the tests in terms of a test rig frame which impose the selected boundary conditions on the specimen. As a result of the collaboration an important prerequisite in the design work was that the interface between the frame and the test specimens had to function for both separate projects.

Considering that a welded interface between plate and support would be difficult when dealing with both steel and aluminium, and considering it was desirable to perform generic testing of several stiffened panels, it was decided to follow a different approach allowing the tests to be carried out without having to weld the plate to the support frame. This emphasizes

a more efficient and economical execution of the experiments, as more tests may be performed in a shorter time period.

Langseth et al. [12] and [13] studied the plugging capacity of both simply supported plates and clamped plates. The clamped support was obtained by clamping the plate between SHS members bolted to a rigid base. No restrictions were imposed on the in-plane deformation of the plates. With this approach, the supports do not need to resist the in-plane membrane action from the plates directly, which can be severe depending on the type of applied loading. Another possible solution is to use bolts to restrain the in-plane deformations at the support, similar as used in the experimental set-up of a rectangular stiffened plate used by Villavienco and Soares [10].

As a motivation for the present study, it was desirable to represent an area of the external deck on the Edvard Grieg platform. The chosen geometry consists of a 12mm thick steel plate supported on girders with distances 3600mm and 10000mm apart in the length and width direction respectively. The plate is stiffened with Bulb flats HP260x12 oriented in the direction of the shortest span and are given center distances 625mm. It was decided to perform the tests in scale 1:4, which implies the test specimen would consist of 3mm thick plates. Behind this decision, the limitations of the laboratory equipment with regard to size and allowable forces were essential factors.

Also when deciding on the size of the contact area between the plate and concentrated force a few considerations were made. For the steel plate it was desirable to study both the effect of a relatively large size object striking the plate field, and to study the effect of a more locally applied load between the stringers. Description of these will be given in more detail later on.

After reviewing different approaches with regard to boundary conditions and size of the test specimen, it was concluded on some major guidelines. The guidelines can be summarized as:

- The plate should be clamped but with no restrictions imposed on the in-plane deformations of the specimen
- The plate field size should be at least 1000x1000mm and stiffened with 4-6 stringers oriented in the same direction
- Highest strains and probability of fracture should be at the center of the plate field (fracture at the supports is not desired)

### **4.3 Test specimen, support frame and indenter geometry**

#### **4.3.1 Test specimen geometry**

The test specimen geometry is shown in Figure 4-1. Detailed drawings are found in Appendix A. The test specimen consists of a rectangular plate and six stringers that are welded onto the plate. Intermittent fillet welds with throat size 3mm, weld length of 15mm and a distance of 45mm between the centers of the welds is used. Application of the dimensions of the intermittent fillet welds is shown in Figure 4-2. The plate width and length are 1250mm and 1375mm respectively. Nominal thickness of the plate is 3mm. The stringers are positioned in the transverse direction and have angle shaped geometry with a height of 65mm, a width of 18 mm and a nominal thickness of 3mm. The dimension of the stringer is chosen to obtain similar section properties as a scale 1:4 version of a Bulb flat HP260x12. The material used is of steel grade DOMEX 355 MC E as described in section 3.

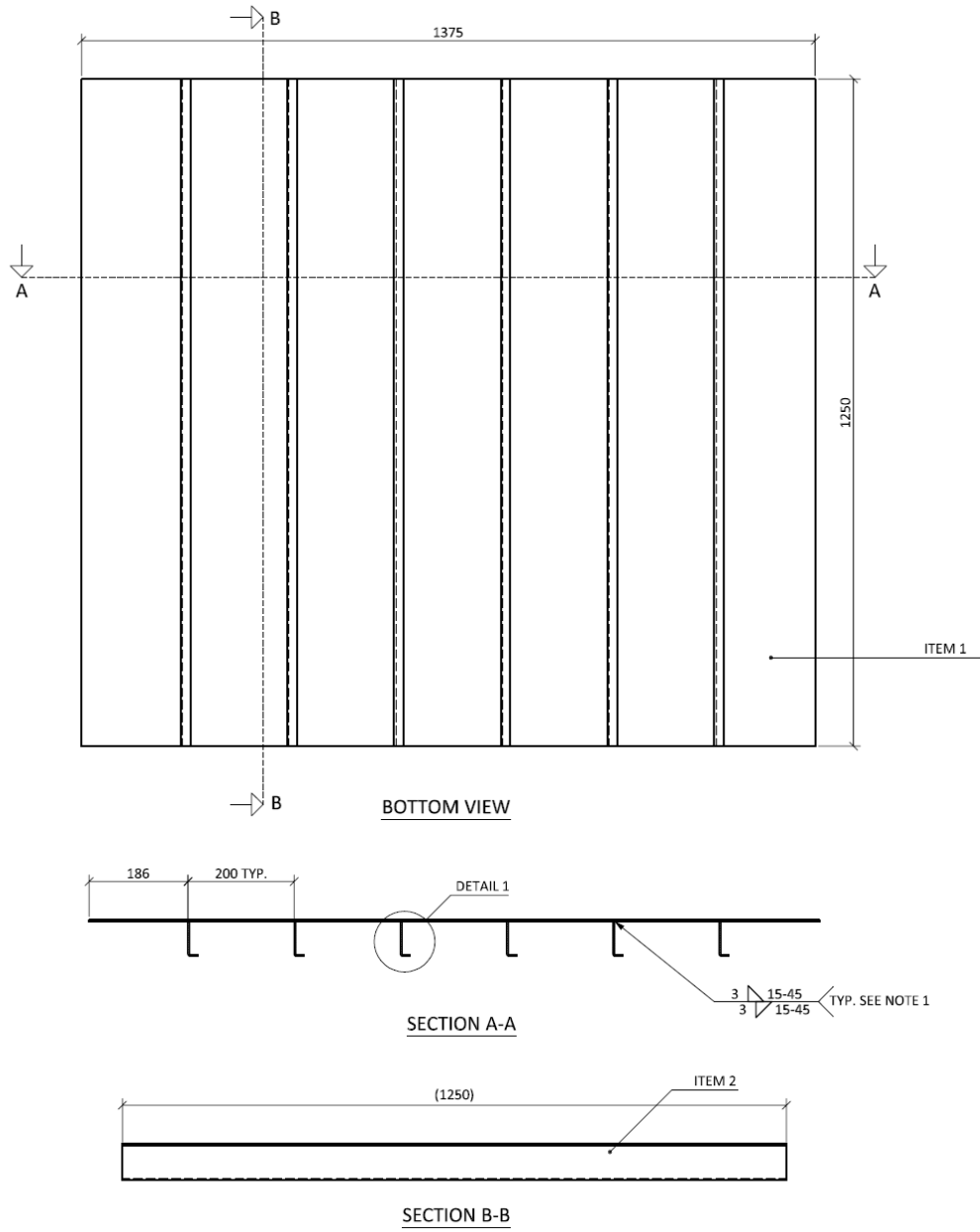


Figure 4-1: Test specimen geometry.

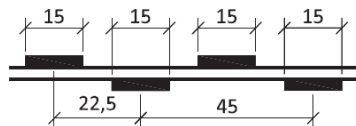


Figure 4-2: Application of dimensions to intermittent fillet welds.

#### **4.3.2 Test rig frame and test rig assembly**

To allow the execution of generic testing in the laboratory, a test rig frame is designed and constructed. A sketch of the complete assembly of test rig frame with specimen installed is shown in Figure 4-3. Detail design drawings of both the test rig frame and the complete assembly are found in Appendix A.

The test rig frame (also referred to as support frame) consists mainly of a top and a bottom frame that is bolted together after the test specimen is installed on top of the bottom frame. In total 8 off M16 bolts in property class 12.9 is utilized to ensure that the plate is properly clamped between the two frame parts. At the interface between the plate and the frame, Teflon sheets are added in order to reduce the effects from friction forces to a minimum. 50mm wide cut-outs are provided in the bottom frame so that the stringers may be continuous into the supports, and 8mm thick shim plates are used to ensure that the test specimen is supported as much as possible, by reducing the gap from 50mm, to approximately 10mm. The top frame is equipped with attachment points to enable handling with a fork lift. In addition pad eyes were welded on both the top and bottom frame to enable lifting and handling by a crane. The pad eyes are not showed on the drawing.



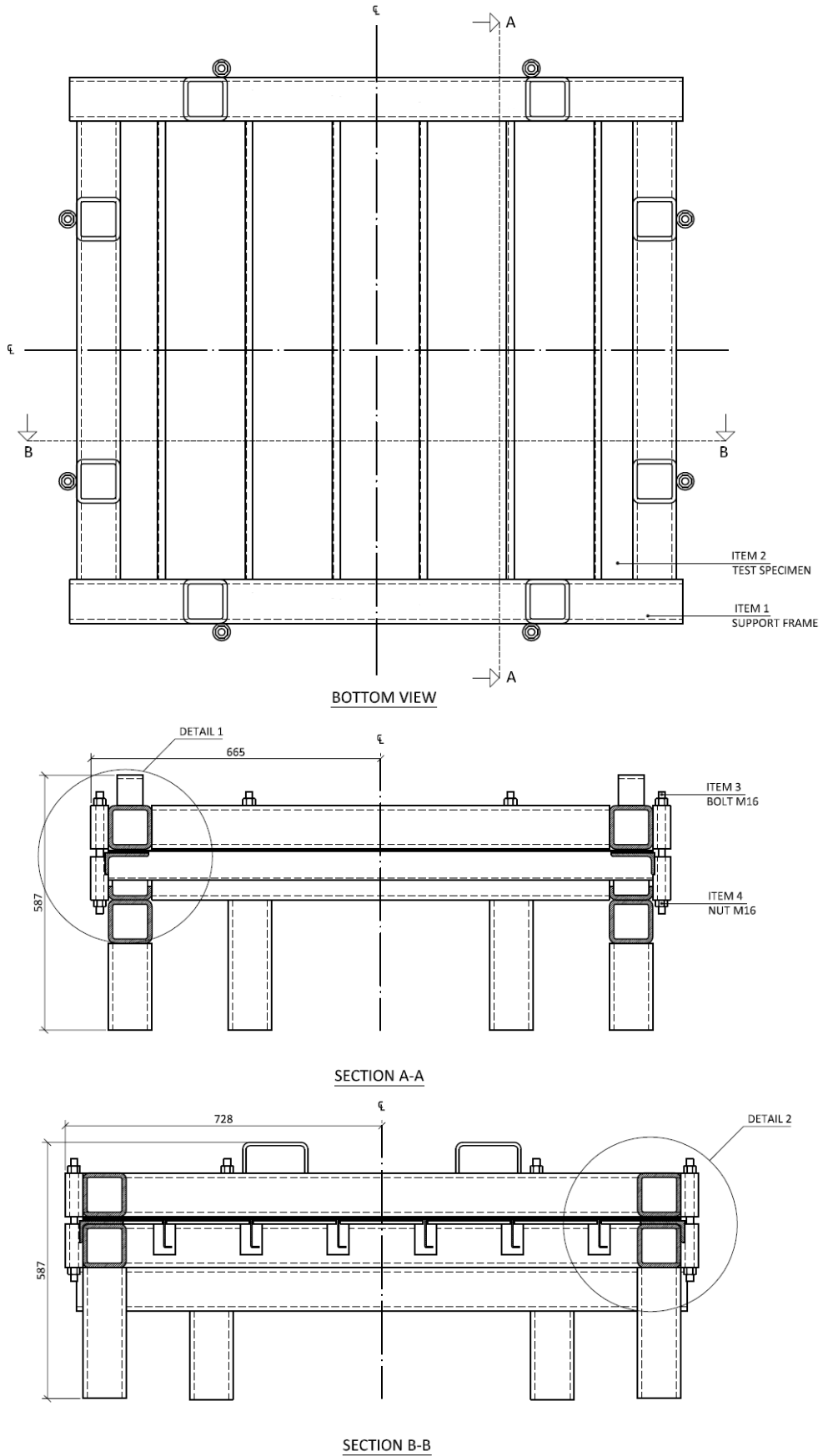
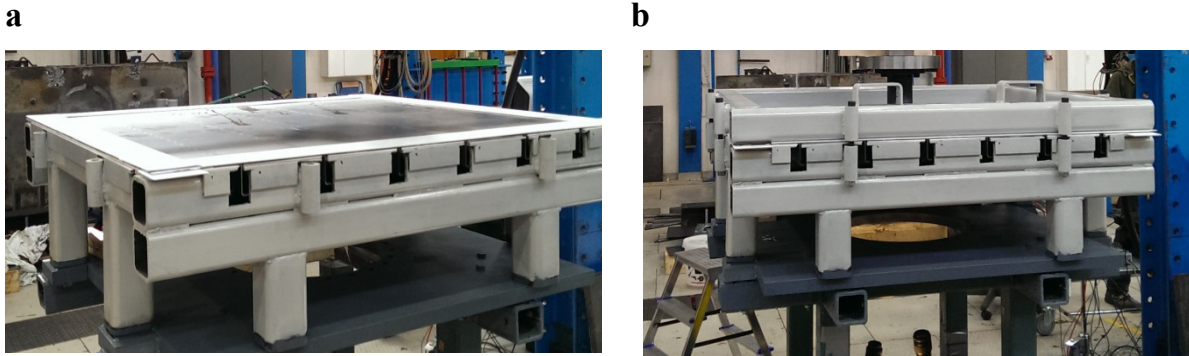


Figure 4-3: Test rig frame with specimen installed.

Figure 4-4a shows a picture of the test rig bottom frame with the specimen installed. The white sheets that may be seen resting on top of the plate are the Teflon sheets. Similar Teflon sheets are also positioned under the plate resting on the shim plates. Figure 4-4b illustrates the complete assembly.



**Figure 4-4: (a) Picture of test rig bottom frame with specimen installed. (b) Picture of complete assembly.**

#### **4.3.3 Corresponding idealized support conditions for specimen**

If disregarding the fact that the stringers are continuous into the supports, thus introducing varying support conditions along the frame, the idealized support conditions may be stated to be:

- The plate is clamped
- There are no restrictions imposed on the in-plane deformations of the specimen

However, the continuous stringers and cut-outs in the frame are important parts of the support conditions and will be included when establishing numerical models in the present study.

#### **4.3.4 Indenter geometries**

Two types of indenter geometries have been selected for the present study. The geometries does not simulate any specific real life objects but are mainly selected to achieve the desirable size of the concentrated loading. Both types of loads will be applied to the geometrical center of the plate field.

The first indenter, denoted indenter A, is an oblong shaped geometry with rounded surfaces. The length of 350mm is sufficient to ensure that contact occurs directly above two of the center stringers of the plate field and as a result, a global deformation pattern occur. The second indenter, denoted indenter B, is a hemispherical geometry. The main reason it was introduced was to study the effect of a more locally applied load between the stringers. Figure 4-5 and Figure 4-6 illustrates indenter A and B respectively.

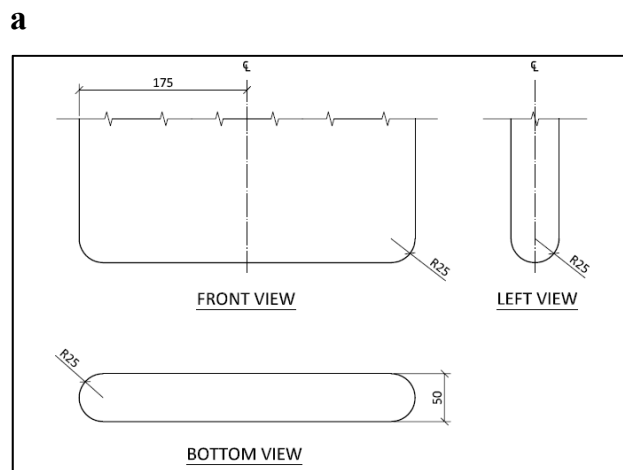


**Figure 4-5: (a) Sketch of indenter A. (b) Picture of indenter A.**

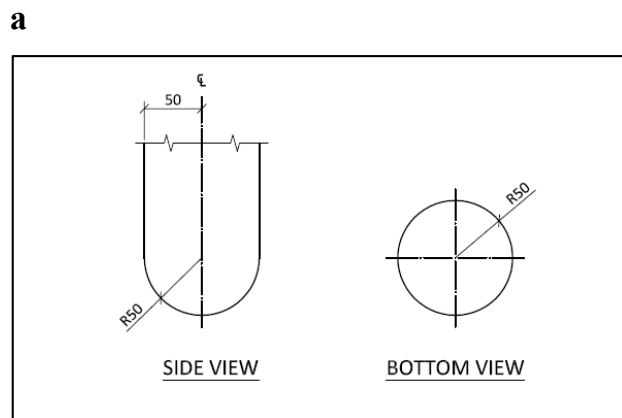


**Figure 4-6: (a) Sketch of indenter B. (b) Picture of indenter B.**

#### 4.4 Summary of design history

The support frame and geometry of the stiffened plate were changed several times due to various considerations that emerged during the design phase. In order to emphasize the amount of work done, the different design concepts and solutions that were considered will be briefly described in this section.

The main tasks during the design phase can be summarized as below:

- Literature study of previous work on the topic
- Choices regarding test specimen geometry and support conditions
- Measurements of laboratory equipment in order to determine allowable dimensions of the test rig
- Decide on dimensions and generate drawings
- Preliminary analysis
- Design reviews

There was a continuous evolution of the design; however, the major changes can be categorized into three revisions. A few details and remarks on the early designs are summarized below.

##### Revision 1

Figure 4-7 shows an illustration of the layout. The support frame in the first design revision comprised a bottom and top frame with SHS100x10 members. The frame internal and external measurements were 1050x1050mm and 1250x1250mm respectively. The plate outer dimensions were 1350x1350mm, i.e., the plate extended beyond the frame. This solution was chosen to achieve increased in-plane stiffness. The 3mm thick plate was stiffened with six stringers with center distances 160mm. This stringer spacing was in 1:4 scale of the stringer spacing on the chosen geometry on the Edvard Grieg platform. A distance of 25mm between the end of the stringers and the frame was included to avoid contact due to rotation during loading. Two transverse stiffeners were added as shown in the illustration. These stiffeners were added to constrain the stringers towards lateral rotation at the ends.

The top and bottom frame was connected using M16 bolts in each corner and midpoint of the frame members (8 off in total). Cut-outs and slotted holes for bolts were provided in the plate.

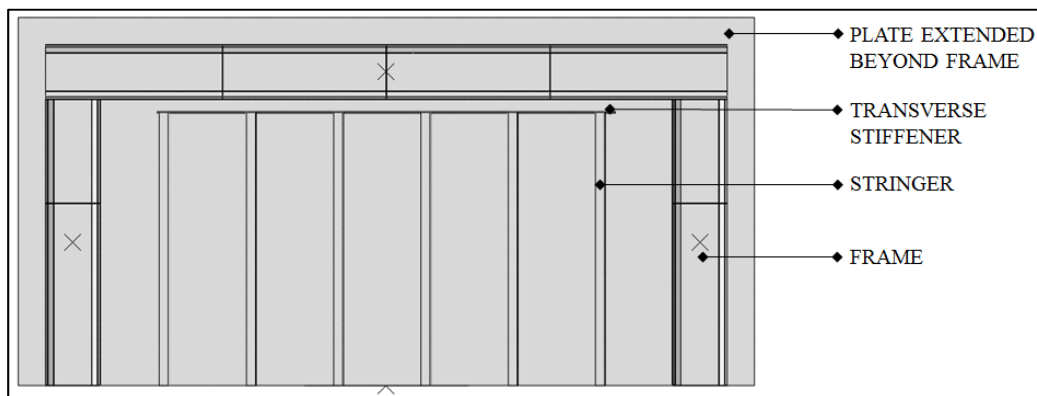
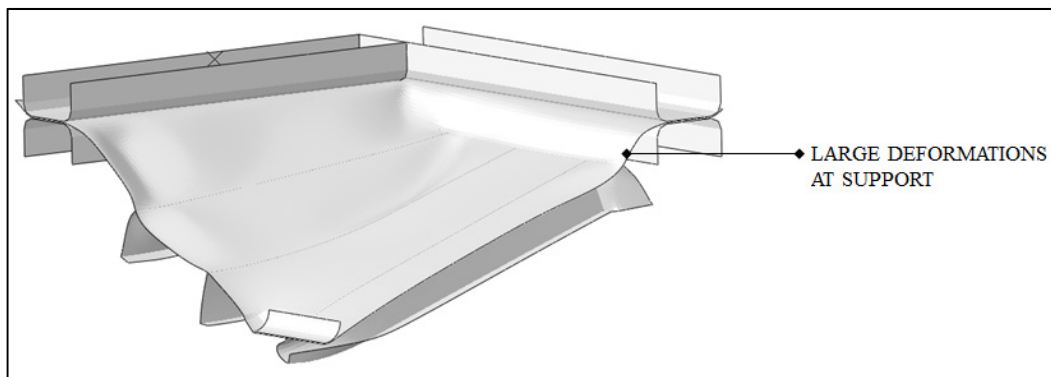


Figure 4-7: Design revision 1 - Illustration of design.

In the initial design phase of the plate field and the support frame the indenter was assumed to be an oblong shaped geometry similar shown in Figure 4-5. However, the parts that provide rounded surfaces on the short sides were included at a later stage to avoid unwanted high strain concentrations due to sharp edges on the indenter (parts that are bolted on may be seen by inspecting Figure 4-5b).

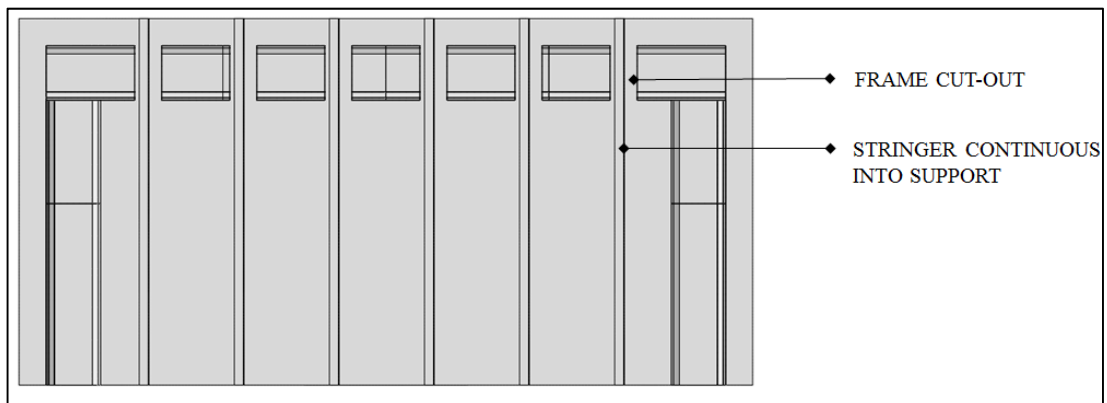
With the chosen layout the plate failed in bending at the supports and undesirable large displacements in those regions occurred for the applied loading. The reason for this was that the stringers were not continuous into the supports. I.e. there was a significant reduction in the out-of plane stiffness just in front the supports. This is illustrated in Figure 4-8.



**Figure 4-8: Design revision 1 - Illustration of large deformations at support.**

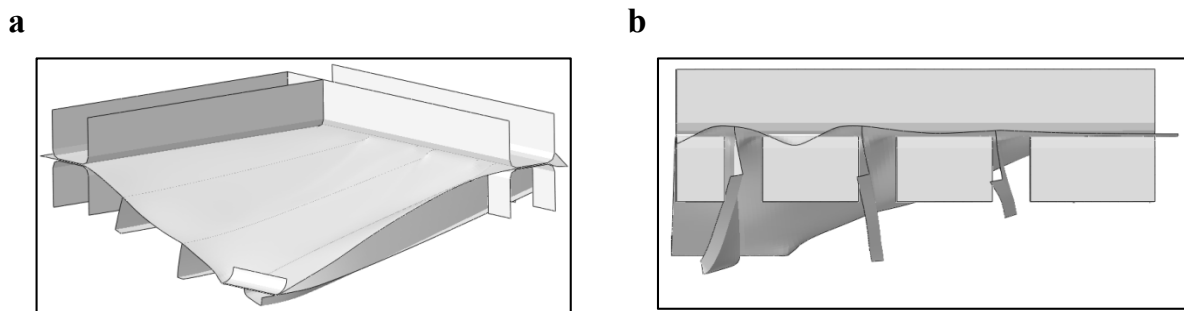
### Revision 2

Figure 4-9 shows an illustration of the layout in the second design revision. Rectangular cut-outs in the frame (50x70mm) were added to enable continuous stringers beyond the supports. To ensure sufficient strength and stiffness of the frame, additional SHS100x10 members were added below the members with cut-outs. In addition to these main modifications of the design, the center distances between stringers were increased to 175mm. This modification was done to match the geometry of the stiffened aluminium plate as it would simplify the design regarding frame cut-outs. Otherwise there were no major modifications to the design.



**Figure 4-9: Design revision 2 - Illustration of design.**

As the stringers became continuous the global vertical displacement close to the supports was reduced. However, significant local deformation of the plate occurred at the supports due to the loss of support surface (no support to restrain buckling at the location of the frame cut-outs). This is illustrated in Figure 4-10. Adding stiff transverse stiffeners (6mm) to the plate on the outside of the frame prevented this issue. This was found to be a plausible design solution for the steel plate. However it was disregarded as it was not easy to implement on the aluminium plate which displayed the same issue.



**Figure 4-10: Design revision 2: (a) Illustrates the improvement when having stringers continuous into the support. (b) Illustrates deformations at cut-outs.**

At this design stage, preliminary analyses using different indenter geometries were carried out. Both large cone shaped and circular flat bottom shaped geometries were tested in addition to the oblong indenter described previously. Loading the stiffened steel plates until fracture was of great interest for the present study. It was suspected that the initially chosen combination of plate field size and support conditions would not result in fracture in the steel plate for a large size indenter. Preliminary analyses showed that the plate might completely slide off its supports before fracture occurred. If fracture occurred in the analysis, it was at very local areas due to sharp edges on the indenter, which was not very interesting for the present study. Nevertheless, the chosen geometry and support conditions turned out to be suitable for the parallel study on stiffened aluminium plates that shared the test set-up, and it was decided not to change the design due to this. These considerations were the main reason that the hemispherical indenter geometry as shown in Figure 4-6 was introduced. With this geometry, the effect of a more locally applied load between the stringers could be studied.

### Revision 3 (final revision)

The final design and layout of the plate field and support frame is already presented. However, a few comments in relation to the design history are given in this part. Due to an updated geometry of the aluminium plates the stringer center distances had to be increased to 200mm. The updated geometry of the stiffened plates resulted in a requirement to increase the width of the frame, which was increased from 1050mm to 1175mm.

The plate is no longer extended beyond the frame. This was necessary for the design concept that was chosen for the locking mechanism. In the final design the top and bottom frame is connected using an arrangement where the 8 off M16 bolts are positioned on the outside of the frame. With this solution the bolts are not run through the plate, and cut-outs or slotted holes in the test specimen could be avoided. The shim plates were added to reduce the deformations that are illustrated in Figure 4-10b.

## 4.5 Preliminary analysis

### 4.5.1 General

In order to acquire knowledge of the expected behaviour and response of the stiffened steel plates subjected to concentrated loading, preliminary analyses were performed using Abaqus. Two main conditions are relevant, the quasi-static tests and the dynamic tests. The preliminary analyses were directly used in the design phase of the tests, i.e. design of the plate-field, design of the support frame, determination of indenter size, mass and velocities etc. Several analyses were run with various modifications to the general arrangement that was proposed during design reviews. All analysis reported in this section is based on the final plate-field and support frame design and are performed prior to the experiments.

Two main approaches are followed when creating computer models for numerical simulations of the quasi-static and the dynamic tests. In the first approach, both the indenter and the frame is considered to be infinitely stiff, hence the load response only depends on the behaviour of the finite elements simulating the stiffened steel plate. In the second approach, the frame stiffness is simulated, while the indenter is still considered to be infinitely stiff. A basic computer model for each of the two main approaches has been created. The models are denoted basic computer model 1 (BM1) and basic computer model 2 (BM2) for rigid and deformable frame respectively. The main purpose of the basic computer model is to have a common analysis set-up. For each separate analysis, the basic computer model is modified with analysis specific input, i.e. material definitions, indenter velocities, mesh sizes etc.

### 4.5.2 Basic computer model 1 (rigid frame)

#### Geometry model and mesh

Plate field:

Symmetry is utilized and only half the plate field is modeled. Section thickness of plate and stringers are taken as 3mm. The geometry is assumed to be mathematically perfect (i.e. no imperfections are applied). The S4R element in Abaqus is assigned to the plate field. As described in section 2.2.3, this is a 4-node thin or thick shell element with reduced integration, hourglass control and finite membrane strains. The plate field is divided into several regions, to enable differential mesh density assignments if required. In the basic computer model the default mesh size is taken as 12mm for the entire part, which corresponds to 4-times the thickness of the plate sections. The meshed plate field part is shown in Figure 4-11.

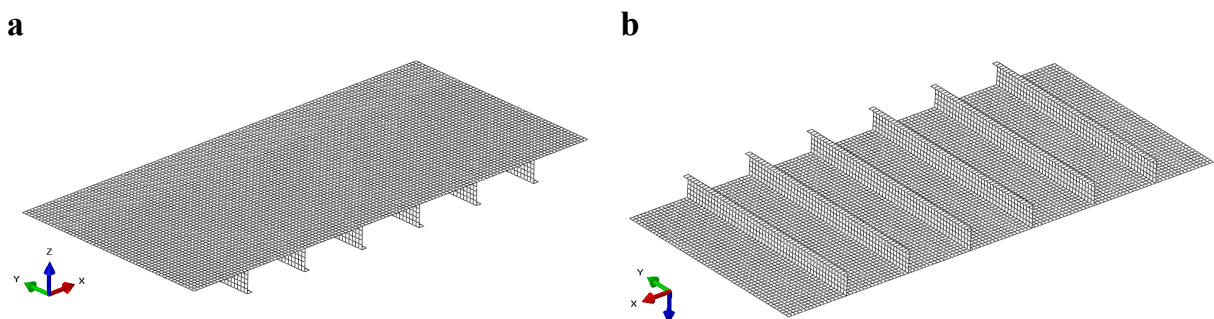


**Figure 4-11: BM1 - Plate field with mesh. (a) and (b) shows the upper and lower side of the finite element model respectively.**

Indenter:

Two indenter geometries as described in section 4.3.4 are utilized in the present study. Both indenters are assumed to be infinitely stiff and modeled using discrete rigid surfaces (R3D element in Abaqus). Only the relevant geometries of the indenter, i.e. regions that may interact with the plate field are modeled. The rigid surfaces are given a mesh size of 6mm. The indenter is given a more dense mesh than the plate field in order to simulate the rounded surface properly. The two different meshed indenter parts are shown in Figure 4-12.

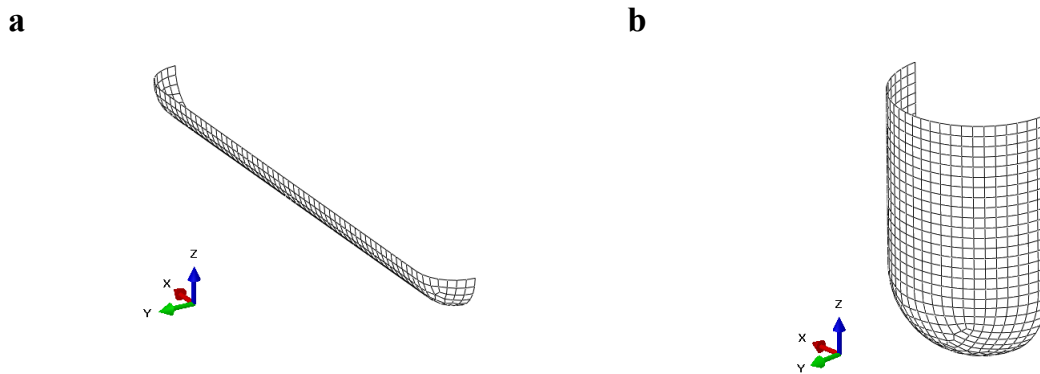


**Figure 4-12: BM1 - Indenters. (a) shows indenter A. (b) shows indenter B.**

Support frame:

The support frame is assumed to be infinitely stiff and modeled using discrete rigid surfaces (R3D element in Abaqus). As for the indenter geometry, only the relevant parts of the support frame, i.e. regions that may interact with the plate field, is modeled. An initial gap of 0.01mm is introduced between the plate field and the discrete rigid surfaces. The frame simulation surfaces are given a mesh size of 15mm. The meshed frame simulation surfaces together with the plate-field and indenter A is illustrated in Figure 4-13.

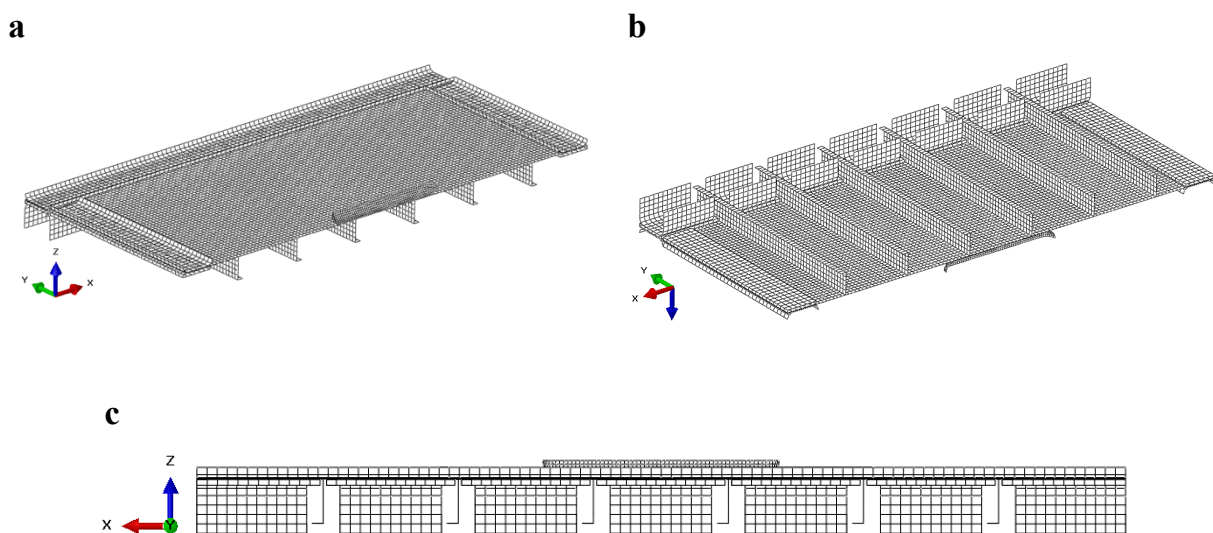


**Figure 4-13: BM1 - Assembly with mesh. (a) and (b) shows the upper and lower side of the finite element model respectively. (c) shows the front side of the model.**



Material model

A material definition denoted MAT1-prelim is assigned to the stiffened steel plate part in the computer model. This is the material model that is used in the major part of the preliminary analysis and it was defined prior to performing material tests on the actual material. The material curve for MAT1-prelim is obtained from tension tests performed on S355 material in previous research work performed at SIMLab, NTNU (unpublished). The yield limit is 336MPa, and the plastic behaviour includes a yield plateau and a strain hardening based on a power law expression. MAT1-prelim is given the steel density 7.85tonnes/m<sup>3</sup>, and the steel elastic properties in terms of a Young’s modulus of 210000MPa and a Poisson’s ratio of 0.33. For the preliminary dynamic analysis, a possible strain rate effect on the material behaviour is neglected. The plastic properties of material model MAT1-prelim is shown in Figure 4-14.

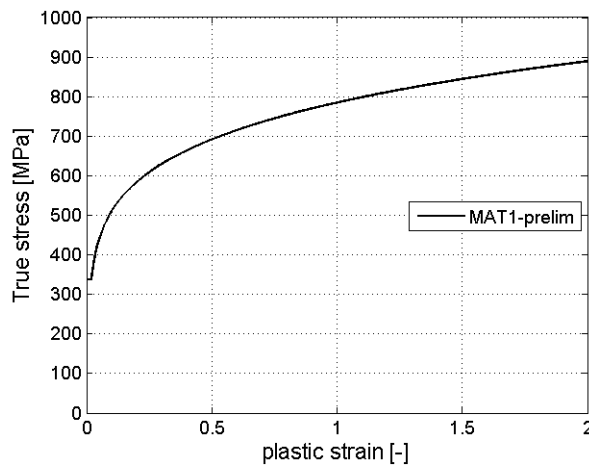


**Figure 4-14: BM1 - Plastic material behaviour of MAT1-prelim.**

Interactions

Three contact properties are defined. The contact properties are shown in Table 4-1. A general contact definition that includes all surfaces is defined and given the global contact property “IntProp-1”. An individual contact property, “IntProp-2”, is specified at the interface between the plate and the Teflon sheets mounted on the frame. In the interface between the indenter and the plate, the individual property “IntProp-3” is specified.

**Table 4-1: BM1 - Contact properties.**

Contact property name	Normal behaviour	Tangential behaviour
IntProp-1	Hard contact (penalty)	Penalty, friction $\mu_1=0.3$
IntProp-2	Hard contact (penalty)	Penalty, friction $\mu_2=0.0$
IntProp-3	Hard contact (penalty)	Penalty, friction $\mu_3=0.3$

Boundary conditions

The locations of the boundary conditions used in the analysis are shown in Figure 4-15, while the properties are listed in Table 4-2. The discrete rigid surfaces simulating the support frame is fixed for all degrees of freedom. The indenter is fixed for all degrees of freedom except translation in z-direction. The properties of BC1 correspond to a symmetry condition in y-direction.

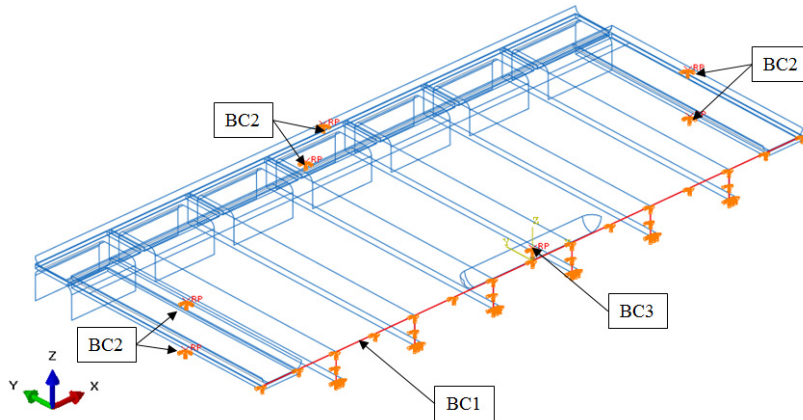


**Figure 4-15: BM1 - Boundary conditions.**

**Table 4-2: BM1 - Displacement/rotation boundary conditions.**

	<b>UX</b>	<b>UY</b>	<b>UZ</b>	<b>URX</b>	<b>URY</b>	<b>URZ</b>
BC1	Free	Fixed	Free	Fixed	Free	Fixed
BC2	Fixed	Fixed	Fixed	Fixed	Fixed	Fixed
BC3	Fixed	Fixed	Free	Fixed	Fixed	Fixed

Loads and load steps

The basic computer model is used in simulations of both dynamic and quasi-static tests. Both types of simulations are performed using explicit dynamics. An analysis load step named “step-1” with the explicit dynamic procedure is created. Description of the load step is given in Table 4-3. As mentioned in the table, input such as time period and indenter velocities are specified in the basic model, but this will also be given as analysis specific input. In addition an initial load step is created by Abaqus by default. The boundary conditions described above are assigned to the initial load step.

**Table 4-3: BM1 - Loads and load steps.**

<b>Load condition</b>	<b>Description</b>
Dynamic	<ul style="list-style-type: none"> <li>• Non-linear geometry is applied.</li> <li>• The indenter is given a mass of 750 kg in the computer model (equivalent to 1500 kg when considering the full geometry).</li> <li>• The indenter is given an initial velocity of 6m/s in negative z-direction and a time period of 0.04 sec is specified (will be varied as analysis specific input).</li> </ul>
Quasi-static	<ul style="list-style-type: none"> <li>• Non-linear geometry is applied.</li> <li>• Time scaling is utilized and the massless indenter is given a constant velocity of 6m/s in negative z-direction. A time period of 0.04 sec is specified</li> </ul>

**4.5.3 Basic computer model 2 (deformable frame)**

Geometry model and mesh

Plate field and indenter:

The plate field and indenter geometries and mesh in the computer model with deformable frame are identical as for the computer model with rigid frame as described in section 4.5.2.

Support frame:

The support frame is modeled using deformable elements and is shown in Figure 4-16. The SHS100x10 members are modeled using the previously described S4R shell element in Abaqus. The section radius is omitted in order to simplify the mesh, and mesh size 15mm is specified. The shim plates (angle 100x50x8) are also modeled using S4R elements with mesh size 15mm. The pipe sections that together with the M16 bolts forms the locking mechanism between the top and bottom frame is modeled using the S4R element and a mesh size of 10mm. The M16 bolts are modeled with beam elements (B31 in Abaqus) with a mesh size of 10mm.

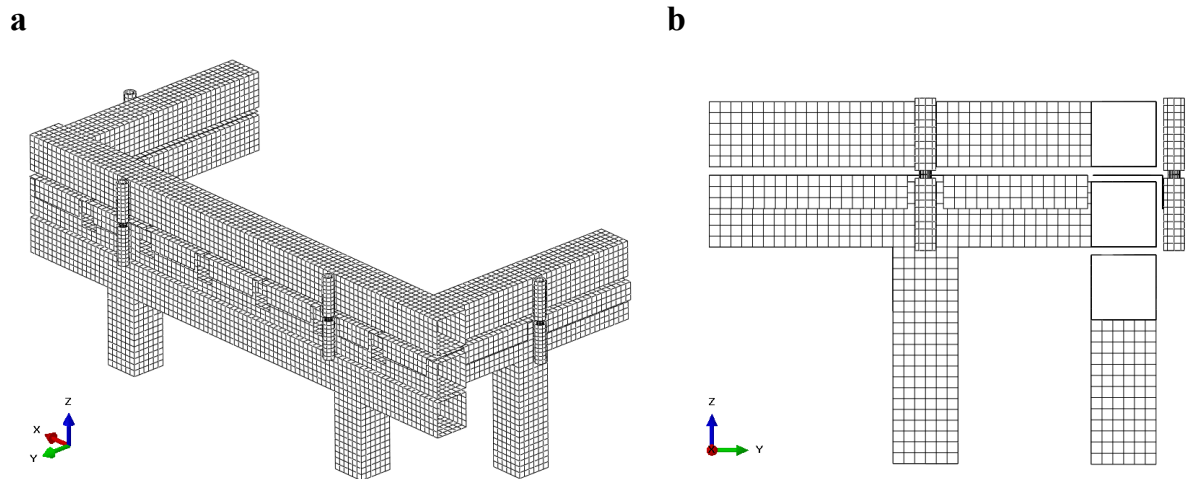


Figure 4-16: BM2 - Frame model with mesh: (a) Perspective view. (b) Side view.

Material models

Table 4-4 shows an overview of the different materials that are defined in the basic model. As for the basic computer model with rigid frame, a material definition denoted MAT1-prelim is assigned to the plate field. In addition a purely elastic and an elastic-perfectly plastic material model is defined and assigned to elements simulating the frame assembly. The decision of using an elastic-perfectly plastic material on the frame members and shim plates is based on that plastic strains, hence also the strain hardening, are expected to be low for these elements. An elastic material definition for the bolts is evaluated to be sufficient considering the simplifications made in the modeling of these elements. All materials in the model are given the steel density 7.85tonnes/m<sup>3</sup>, and the steel elastic properties in terms of a Young’s modulus of 210000MPa and a Poisson’s ratio of 0.33.

Table 4-4: BM2 - Material overview.

Material name	Description	Assigned to part
MAT1-prelim	Preliminary material model. Elastic-plastic with isotropic hardening.	Plate field
MAT2	Elastic-perfectly plastic. Yield limit of 355MPa.	All support frame shell elements
MAT3	Elastic	Beam elements simulating bolts

The plastic properties of the material definitions MAT1-prelim is identical as for basic computer model 1.

Interactions

The contact definitions in the computer model with deformable frame are identical as for the computer model with rigid frame as described in section 4.5.2.

In addition to the contact definitions, several constraints are needed in this extended version of the computer model. Figure 4-17 shows the constraints that are used in the modeling of the locking mechanism between the top and bottom frame. A master-slave node technique is utilized and all applicable DOF's are constrained.

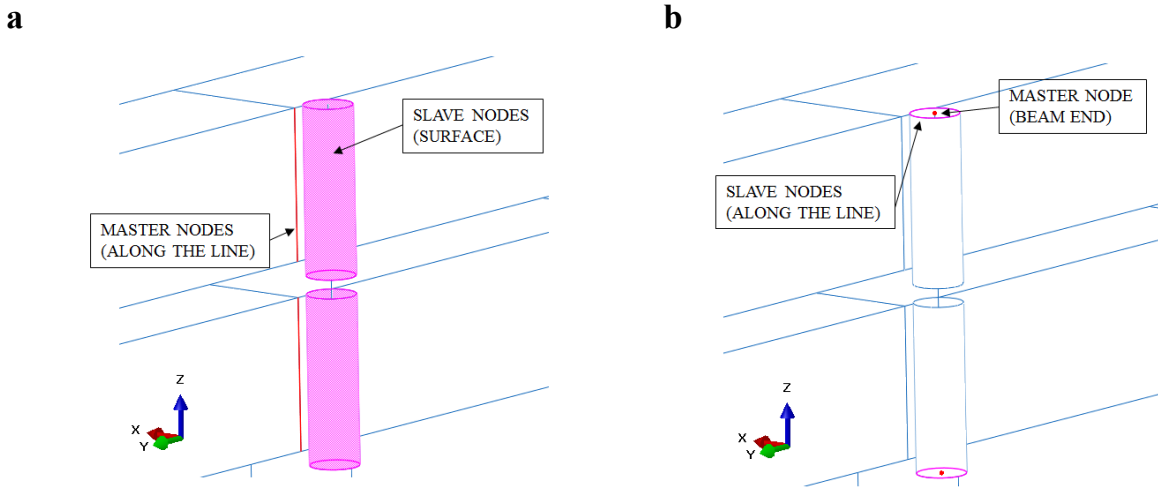


**Figure 4-17: BM2 - Modeling of locking mechanism: (a) Constraint between the surfaces simulating the frame and the pipe section. (b) Constraint between the surface simulating the pipe section and the beam element simulating the M16 bolt.**

As shown in Figure 4-18, the surfaces simulating the lower horizontal SHS100x10 member are tied to the remaining part of the bottom frame by a master-slave constraint along two lines (at the location of welds). Also as shown in Figure 4-18, the shim plates are constrained to the surfaces simulating the top flange of the bottom frame in the basic computer model. The constrained approach will be somewhat stiffer than the real situation. This was used in the preliminary phase as the decision of leaving the shim plates unfastened was not yet made. The shim plates may alternatively be covered by the general contact formulation, using the global interaction property. The unconstrained approach will be considered when comparing results with the experiments and will be specified if used.

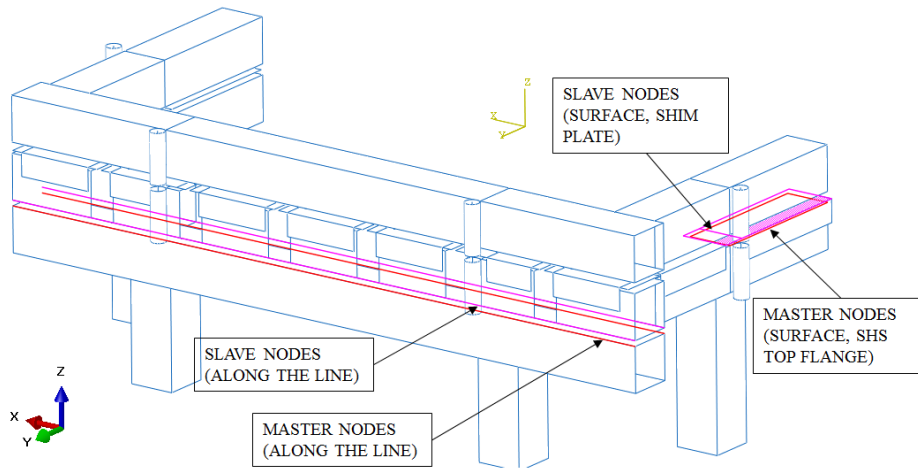


**Figure 4-18: BM2 - Various constraints.**

Boundary conditions

The locations of the boundary conditions used in the analysis are shown in Figure 4-19, while the properties are listed in Table 4-5. As seen in the figure, boundary conditions at the elements simulating the supports of the frame (BC2) are applied at one of the square hollow section edges, simulating the welding that is applied towards the foundation. The indenter is fixed for all degrees of freedom except translation in z-direction. The properties of BC1 correspond to a symmetry condition in y-direction.

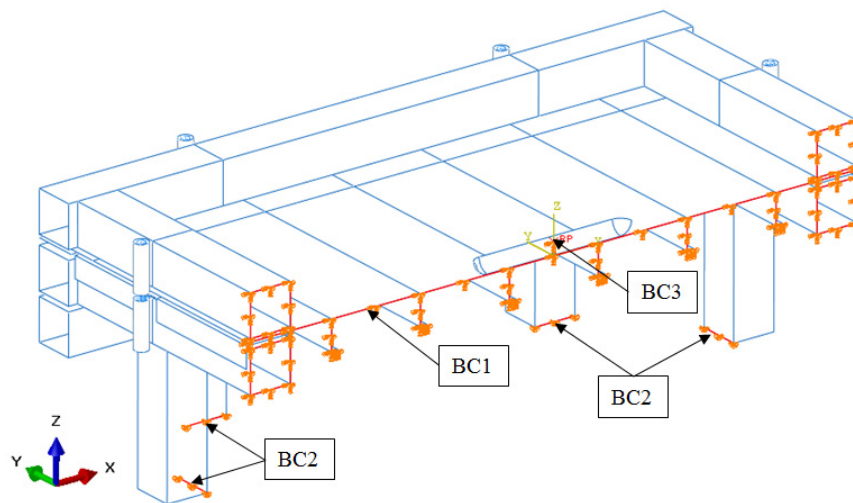


**Figure 4-19: BM2 - Boundary condition locations.**

**Table 4-5: BM2 - Boundary conditions.**

	UX	UY	UZ	URX	URY	URZ
BC1	Free	Fixed	Free	Fixed	Free	Fixed
BC2	Fixed	Fixed	Fixed	Fixed	Fixed	Fixed
BC3	Fixed	Fixed	Free	Fixed	Fixed	Fixed

### Loads and load steps

The loads and load steps in the computer model with deformable frame are identical as for the computer model with rigid frame as described in section 4.5.2.

## **4.5.4 Preliminary simulations of dynamic tests**

### General

In addition to acquire knowledge of the expected behaviour and response of the stiffened steel plates subjected to concentrated loading, the purpose of the preliminary analyses is to identify and evaluate the most important input parameters. The parameters identified as relevant for a parametric study of the dynamic simulation are mesh size, friction coefficients, indenter velocities, support stiffness, and material properties. Simulations are performed using both variants of the basic computer models and by two indenter geometries. However, it is found that parametric studies performed on plate/indenter mesh and the friction coefficients using BM1 also is applicable for BM2 due to similarities.

Fracture or instability criteria are not implemented in the preliminary analysis reported in this section. However, the approximate load level at onset of necking accompanied by fracture is estimated based on engineering judgement and evaluation of plastic strain levels and by inspecting the rate of the plastic strains. This is mainly done by performing analysis with a mesh size equal to the plate thickness so that all relevant strain concentrations may be followed.

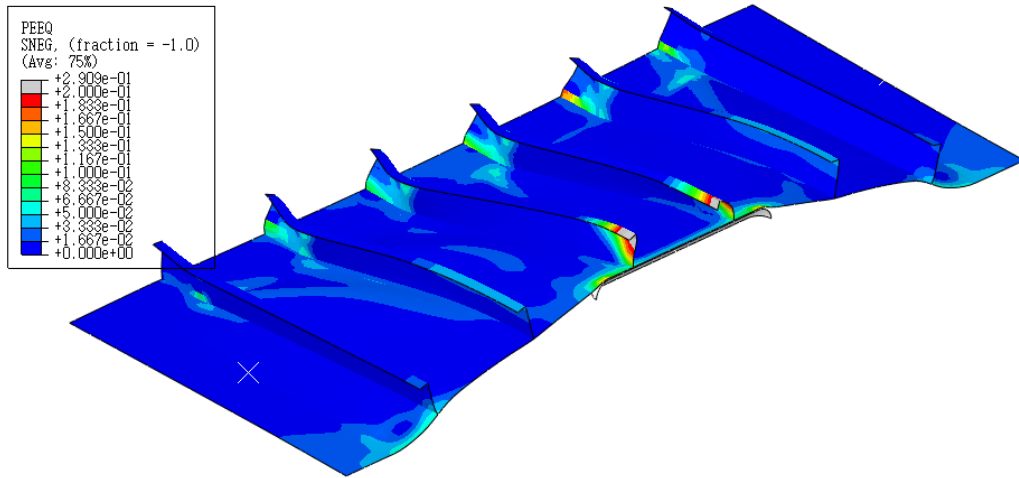
It should be noted that in the result presentations in the following sections, reported forces and energies represent values applicable for the full geometry. In the force-displacement curves, the force is taken as the interface force between the indenter and the plate, and the displacement corresponds to the indentation of the indenter in negative z-direction.

### Simulations using basic computer model 1 with default input

As a first approach, analyses using the input as described in section 4.5.2 are run. The dynamic analysis using basic model 1 with indenter A is denoted “RigDynRunA\_01”, while the corresponding analysis with indenter B is denoted “RigDynRunB\_01”

The initial stable time increment used in these analyses is 1.7e-06sec, while the total number of increments used is 6679 and 6880 for indenter A and B respectively. The equivalent plastic strains at the end of the two simulations are shown in Figure 4-20. Figure 4-21a shows force-displacement curves while Figure 4-21b shows the force-time curves. The energy histories are shown in Figure 4-22.

a



b

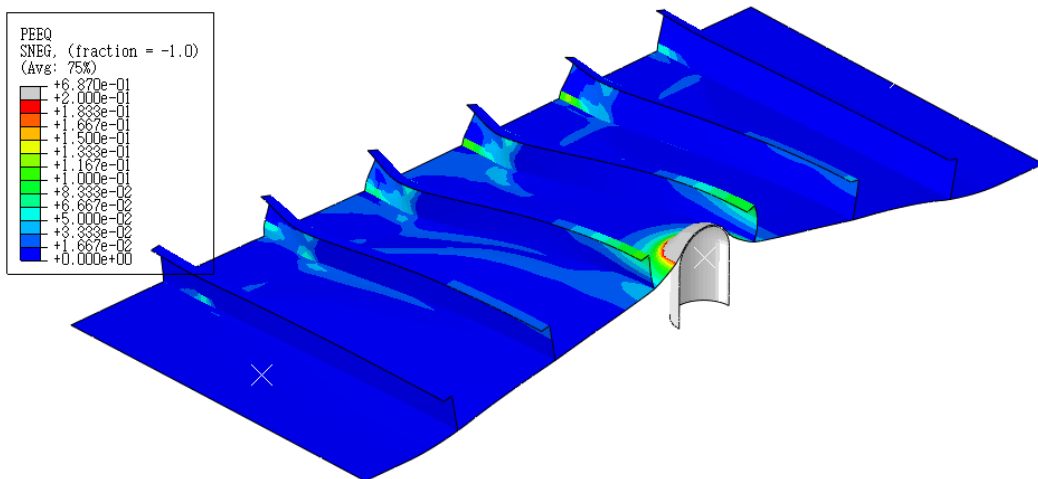


**Figure 4-20: Preliminary dynamic run using BM1 with default input. (a) and (b) shows equivalent plastic strain plots of plate field at the end of the simulations for indenter A and B respectively.**

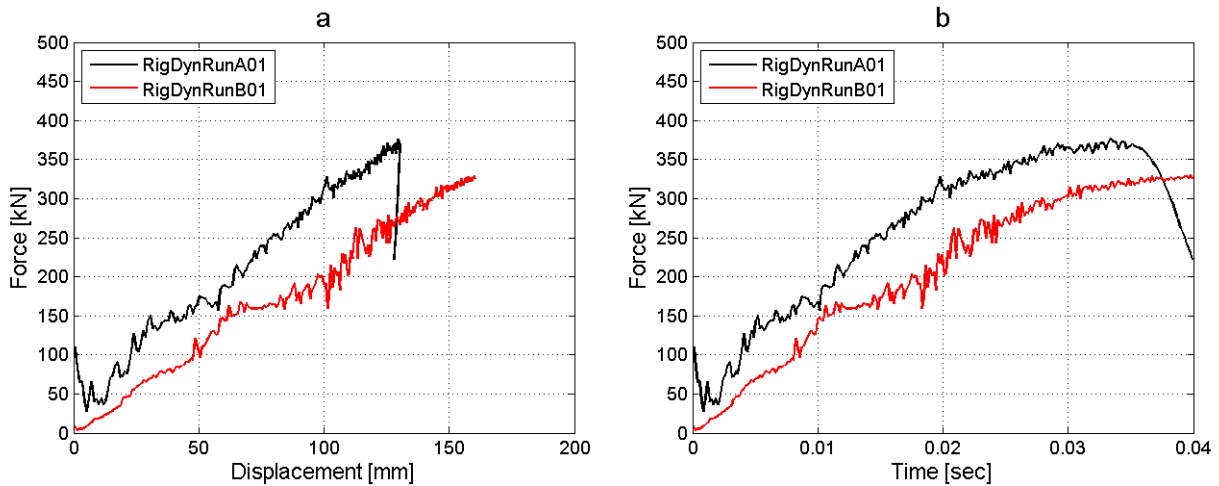


**Figure 4-21: Preliminary dynamic run using BM1 with default input. (a) shows force-displacement curves for indenter A and B. (b) shows force-time curves for indenter A and B.**

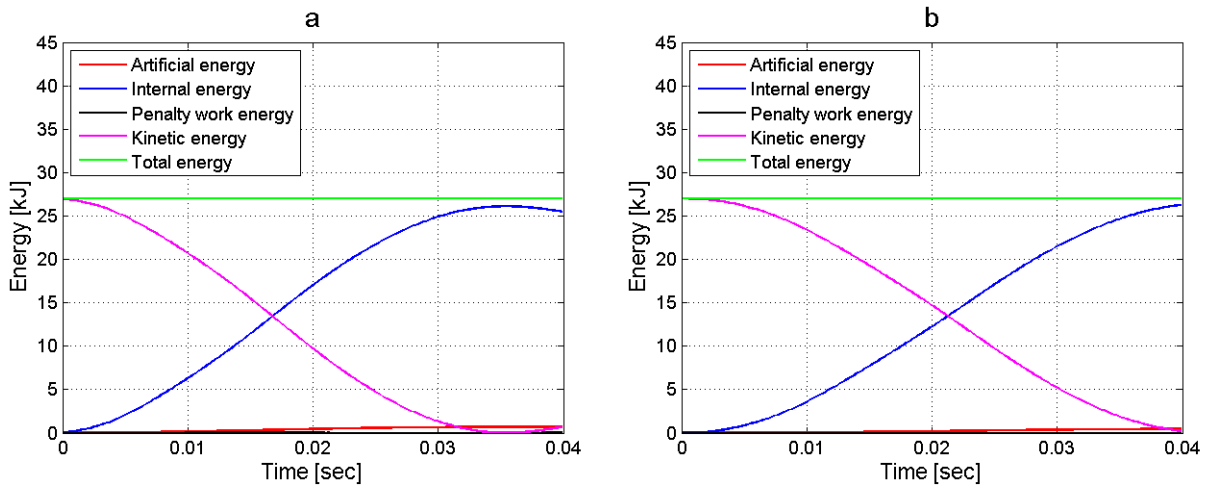


**Figure 4-22: Preliminary dynamic run using BM1 with default input. (a) and (b) shows the energy history for indenter A and B respectively.**

From the plastic strain plots it is seen that for indenter A the two stringers directly below the indenter experience the most onerous straining and that a global deformation pattern occur, while indenter B produces a more localized deformation with high strains in the region between the stringers. It is also noted that the stringers starts to tip over to the side as the load increases. Part of this may be explained by the unsymmetrical cross section of the stringers, but this behaviour is also a result of the rotation of the plate plane during the indentation.

As a preliminary method to predict the onset of necking, the strain level at maximum load in a uniaxial stress state is calculated based on the stress-strain relation of the preliminary material model, and by using Equation (2-24). The resulting strain at onset of necking using this method is found to be 20%. All regions with a plastic strain level above this value are indicated on Figure 4-20 (plotted as grey). The bottom flange of the stringers may be argued



to be close to a uniaxial stress state, and if assuming so, necking has initiated in the flange for the load condition that comprises indenter A.

The difference in the response for the two types of loading is also clearly seen in the force-displacement or force-time curves. As contact occurs directly on the stringers with indenter A, a bending and shear resistance is experienced in the initial stage, resulting in a higher load. The load remains higher throughout the entire impact and the maximum force is approximately 370kN. This increased stiffness in the initial phase also produces dynamic oscillations in the interface load until the support is activated at 0.002sec.

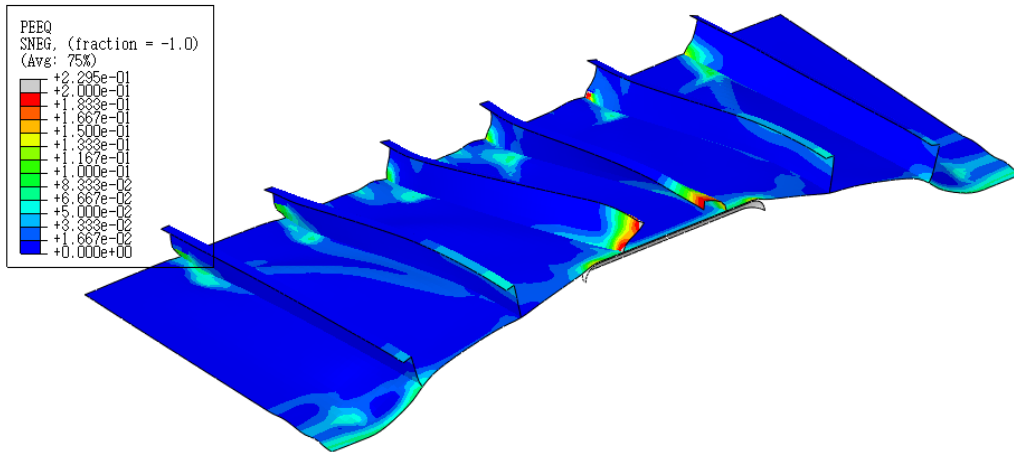
From the energy histories it is seen that for indenter A, all the impact energy has been absorbed at the maximum force, while for indenter B a small amount of kinetic energy remains at the end of the simulation indicating that the time period should be increased. It is also seen that the artificial energy used to avoid hourglass modes in the mesh, and the penalty energy used by the contact formulation is low and negligible compared to the internal energy. The artificial energy will increase when the mesh size increases and reduce when the mesh is refined. Additionally the energy balance (total energy) in the simulations is close to constant, demonstrating that the computed solution is stable.

#### Results of simulations using basic computer model 2 with default input

As a comparison, simulations using the same input as reported in the previous section are performed using the computer model with deformable frame described in section 4.5.3. The analysis with indenter A is denoted “DefDynRunA\_01”, while the corresponding analysis with indenter B is denoted “DefDynRunB\_01”

In the analyses using deformable elements in the frame, the initial stable time increment is 1.4e-06sec. The equivalent plastic strains at the end of the simulations are shown in Figure 4-23. Figure 4-24a shows force-displacement curves while Figure 4-24b shows the force-time curves. The energy histories are shown in Figure 4-25.

**a**



**b**

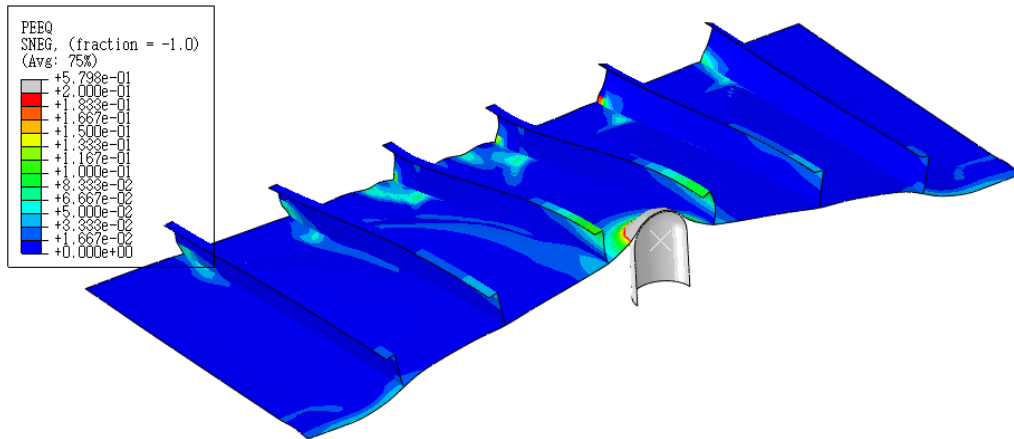


**Figure 4-23: Preliminary dynamic run using BM2 with default input. (a) and (b) shows equivalent plastic strain plots of plate field at the end of the simulations for indenter A and B respectively.**

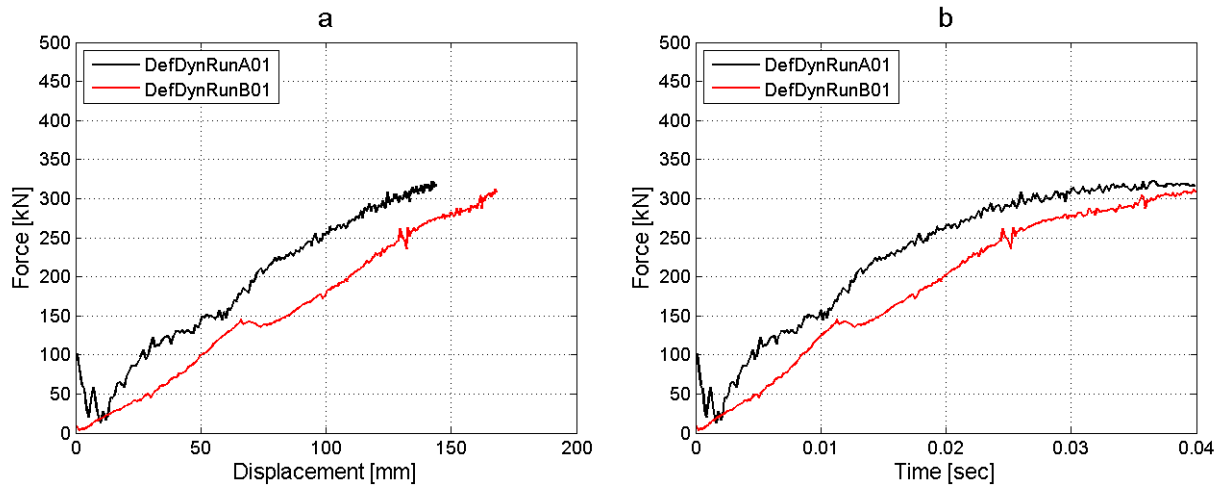


**Figure 4-24: Preliminary dynamic run using BM2 with default input. (a) shows force-displacement curves for indenter A and B. (b) shows force-time curves for indenter A and B.**

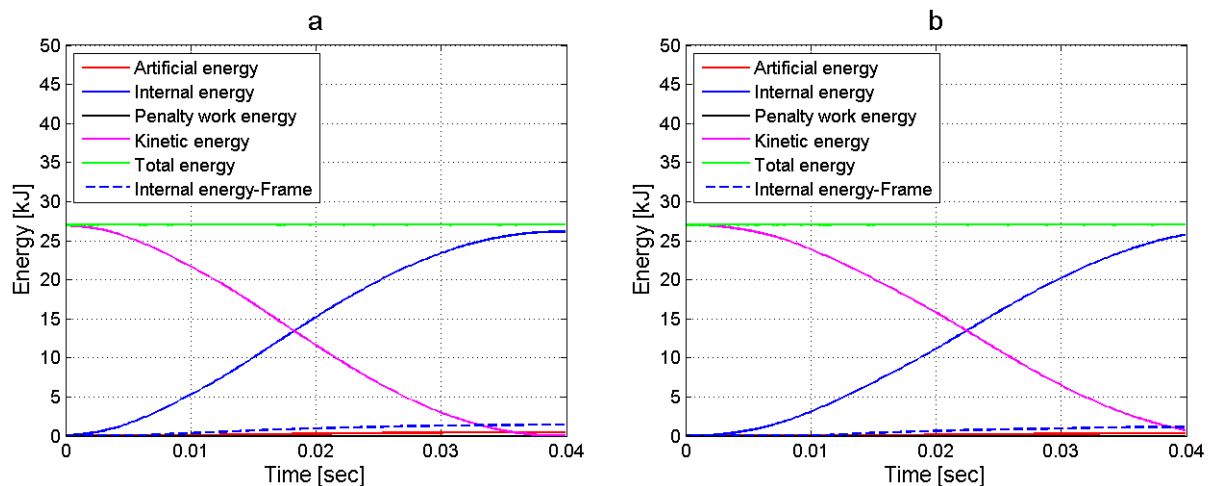


**Figure 4-25: Preliminary dynamic run using BM2 with default input. (a) and (b) shows the energy history for indenter A and B respectively.**

By inspecting the plastic strain plots it is observed that the general deformation pattern is similar to those obtained using the computer model with rigid frame. However, the magnitudes of the equivalent plastic strains are smaller. This is a direct result of the reduced stiffness of the system with corresponding increased ability to absorb the impact energy. Part of the reduced stiffness occurs due to limited plate buckling at the supports. The buckling will directly reduce in-plane stiffness of the plate. The buckling is illustrated in Figure 4-26.

The reduced stiffness and increased ability to absorb the impact is also clearly seen from the force-displacement and force-time curves, where the force is lower than the corresponding force from analysis using BM1. However, it is noted that the difference is smaller for the load condition comprising indenter B. This is due to the more localized deformation, which causes less deformations of the frame.

As for the simulations using BM1, the energy balance is close to constant, and the artificial energy and the penalty energy used by the software is small and negligible compared to the total internal energy. From the energy histories, it is also seen that the internal energy in the frame is small compared to the total internal energy. The internal energy in the frame comprises mainly of elastic strain energy. The expected structural behaviour of the frame during the dynamic tests is discussed further later on.

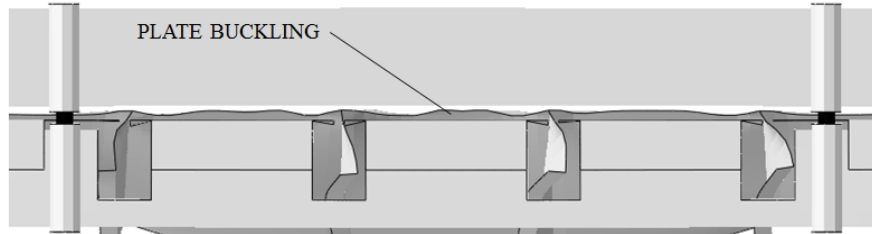


**Figure 4-26: Preliminary dynamic run using BM2 - Illustration of plate buckling at the supports.**

#### Evaluation of mesh density parameters

The first parameter that is studied is characteristic element size,  $l_e$ , in the plate field mesh. BM1 is utilized, and due to similarities the mesh parameter study performed is considered to be applicable also for BM2. Four different characteristic element sizes (also referred to as mesh sizes),  $l_e=(30, 18, 6, 3)$ mm, are investigated in addition to the element size of 12mm defined in the basic computer model. In order to improve contact modeling, the mesh of the indenter is adjusted according to the plate mesh (found to reduce numerical noise). For simulations with mesh sizes 30mm and 18mm, the indenter mesh size is adjusted to 12mm. For mesh size 3mm, the indenter mesh size is taken as 3mm. For mesh size 12mm and 6mm, the indenter mesh size is taken as 6mm (as defined in basic computer model).

Table 4-6 and Table 4-7 present the results from the mesh parameter study performed on simulations using indenter A and B respectively. The results are obtained by simulating a dynamic load condition as defined in the basic computer model ( $v_0=6$ m/s,  $M=1500$ kg). Figure 4-27 and Figure 4-28 shows plots of the deformed center region of the stiffened plate field for three different mesh sizes.

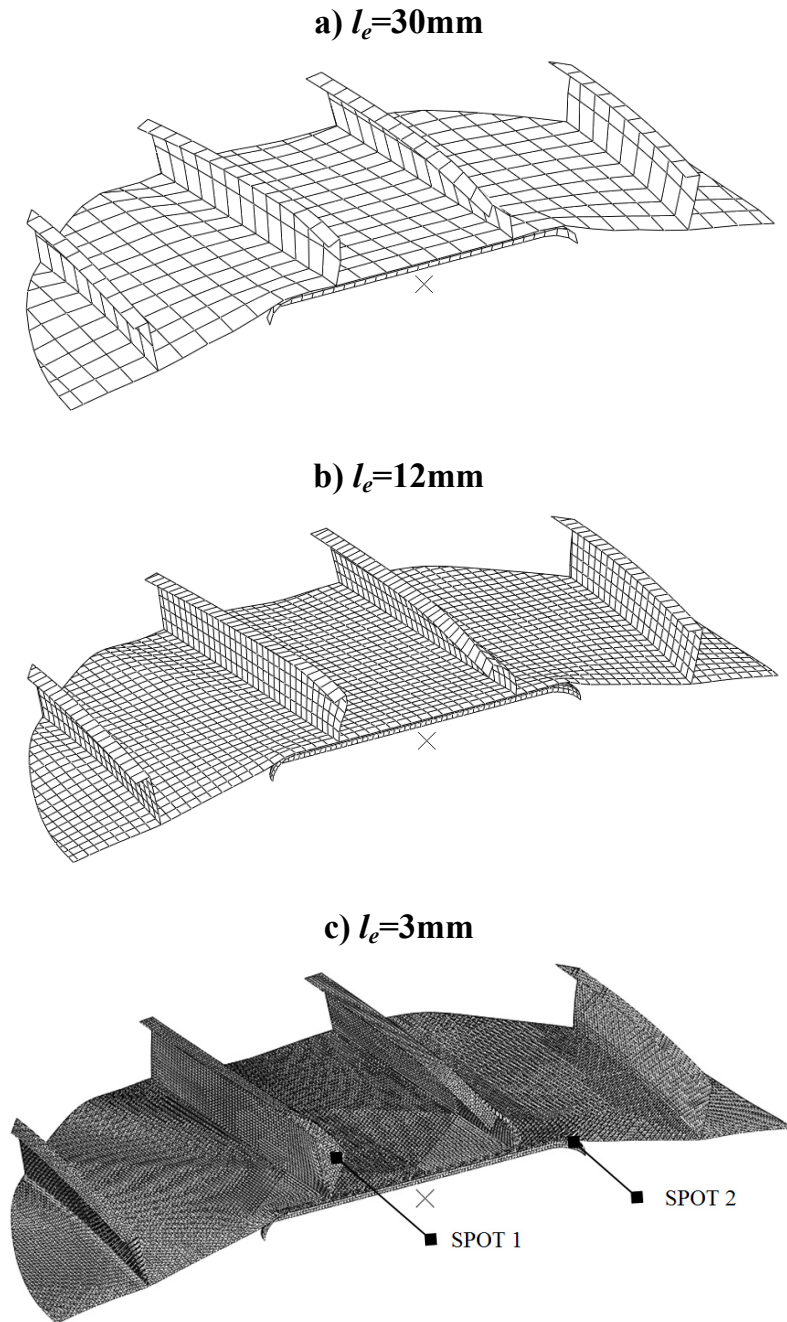


Figure 4-27: Mesh parameter study A: Deformed center region at 125mm indentation.

Table 4-6: Mesh parameter study - Results from simulations with indenter A.

Run	$l_e$ [mm]	Max force [kN]	Max displ. [mm]	$p$ <sup>1)</sup> [-]	$\Delta t_{cr}$ [sec]
RigDynRunA_11	30	390	126	0.25	2.6e-06
RigDynRunA_12	18	365	129	0.26	2.3e-06
RigDynRunA_01	12	360	130	0.29	1.8e-06
RigDynRunA_13	6	353	135	0.30	8.8e-07
RigDynRunA_14	3	342	139	0.33	4.3e-07

1) Maximum equivalent plastic strain in the plate field center region extracted from element integration points.

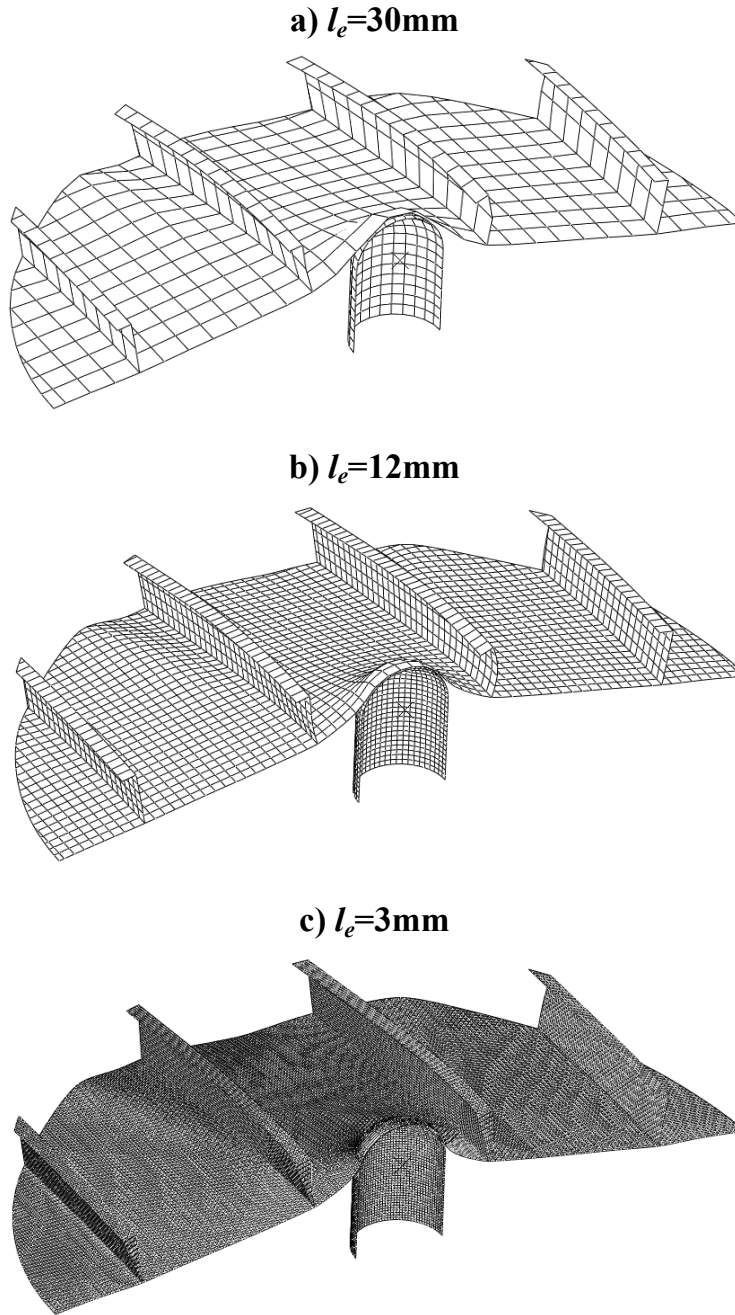


Figure 4-28: Mesh parameter study B: Deformed center region at 155mm indentation.

Table 4-7: Mesh parameter study - Results from simulations with indenter B.

Run	$l_e$ [mm]	Max force [kN]	Max displ. [mm]	$p^{1)}$ [-]	$\Delta t_{cr}$ [sec]
RigDynRunB_11	30	348	155	0.60	2.6e-06
RigDynRunB_12	18	328	158	0.65	2.3e-06
RigDynRunB_01	12	325	160	0.76	1.8e-06
RigDynRunB_13	6	288	164	1.94	8.8e-07
RigDynRunB_14	3	260	-	>2	4.3e-07

1) Maximum equivalent plastic strain in the plate field center region extracted from element integration points.

As expected it is seen that the general pattern is that the force reduces and the displacement and strains increases as the mesh is refined. However, the increase in strains is smaller for indenter A than indenter B. As described in section 2.3.5, a mesh size equal to the plate thickness should be able to describe the evolution of a local neck. Therefore, the analysis using mesh size 3mm provides reliable information whether local necking accompanied by fracture will occur for the applied loading. For simulations using indenter B, a rapid increase in the plastic strains is observed, followed by a reduction of the load. Based on this it is reasonable to assume that fracture will occur for less impact energy than the current 27kJ (1500kg, 6m/s). Tests using indenter A will require higher impact energy.

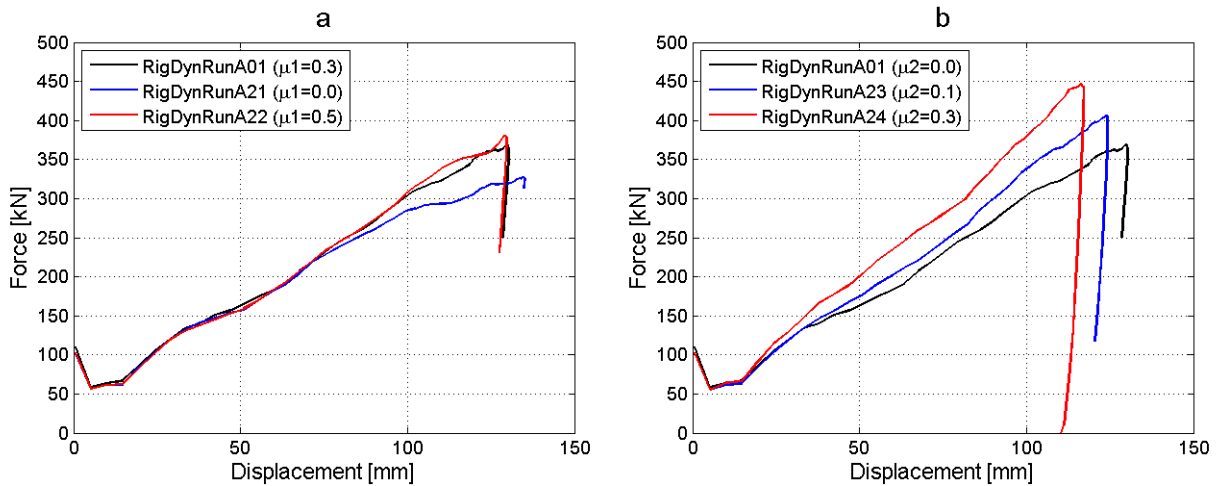
As may be seen, when specifying a characteristic element length 30mm, it results in only two elements over the stringer height and only one element over the width of the flange. For the mesh with characteristic element length 12mm, five elements are used over the web height, while the flange is still covered by only one element. For all simulations with indenter A, it is the stringer flange which displays the highest strains in the plate field center region (location indicated as “SPOT 1”). For the load level present in these simulations, it seems that even the coarsest mesh is able to represent a reasonable estimate of the strain level in the stringer flanges, which almost experience uniaxial tension. For the simulations with a dense mesh, higher strains are observed at the supports. This is in general compressive strains thus not relevant for tensile failure. In addition, high strains are observed at the interface towards the indenter ends (indicated as “SPOT 2”). This is a very local strain concentration, which would require a very dense mesh to capture accurately.

As expected the computational time increases significantly for the finest mesh due to the reduced critical time step (depend on the smallest element in the mesh) and the increase in the number of system DOF's. An approach with a refined mesh only in the regions that experience the largest strains will be considered when simulating the actual tests.

#### Evaluation of friction coefficient parameters

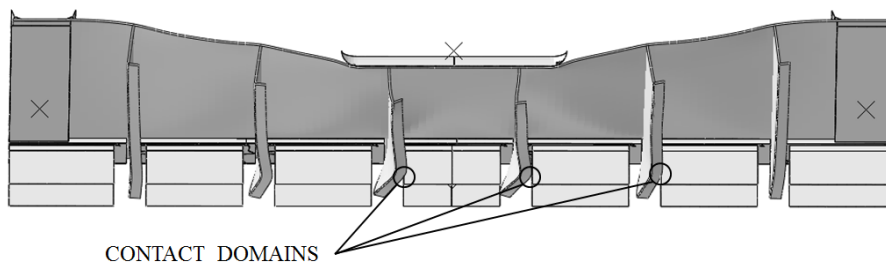
The intention of this part is to study the sensitivity of the friction parameters for the tangential behaviour between the relevant contact regions. First the global friction coefficient ( $\mu_1$ ) that comprises self-contact and the contact between stringers and frame is varied. Next, the friction coefficient ( $\mu_2$ ) between the plate and the Teflon layer on the frame is varied. Finally, the friction coefficient ( $\mu_3$ ) between the indenter and the plate is varied. The two first configurations are studied using indenter A, while the last is studied using indenter B. As for the mesh parameter study, BM1 is utilized, and the general findings from the study are considered to be applicable also for BM2. The dynamic load condition ( $v_0=6\text{m/s}$ ,  $M=1500\text{kg}$ ) and mesh size (12mm) is as defined in the basic computer model.

Figure 4-29 shows force-displacement curves with varying friction parameters for simulations using indenter A. The curves have been smoothed for a clearer result representation.



**Figure 4-29: Friction parameter study, indenter A: (a) Varying global friction coefficient ( $\mu_1$ ). (b) Varying local friction coefficient at supports ( $\mu_2$ ).**

From the force-displacement curves with varying global friction coefficient ( $\mu_1$ ) it is seen that the response is similar until an indentation of approximately 75mm. From there on, the curve that originates from the analysis with zero friction clearly deviates from the two analyses that include friction. At 75mm indentation, the stringers has deformed and tipped sufficiently so that contact with the frame occurs. This is indicated in Figure 4-30. Eventually all the stringers obtain contact with the frame as the indentation increases. Additionally the stringer web is pushed towards the rigid shim plates. The frictional forces due to this contribute to the overall stiffness and the force increases, as clearly seen in Figure 4-29a. Increasing the friction coefficient to 0.5 does not affect the results significantly compared to the results with a friction coefficient of 0.3.



**Figure 4-30: Friction parameter study - Illustration of contact domain between stringers and frame at 75mm indentation.**

By increasing the friction coefficient between the plate and the Teflon layer ( $\mu_2$ ), an increase in the force occurs. Adding friction at the supports, results in restrictions on the in-plane deformations of the plate, hence an increased stiffness occurs. These results demonstrate the importance of adding the Teflon layer. Without it, the response would have been very dependent on using the correct friction properties. However, the static and dynamic Teflon-steel friction coefficient is not zero. A value of at least 0.04 should be expected assuming clean and dry surfaces [33]. This will be considered when comparing results from the component tests with results from analysis.



From Figure 4-31 it is seen that varying the friction coefficient between indenter and plate may also affect the results. Specifying zero friction seems to reduce the maximum load. The explanation for why this happens is illustrated in Figure 4-32. In the simulations with a friction factor the highest strained elements are located at some distance from the geometrical center, and thus a better load distribution occurs. For the simulation with zero friction, the highest strained elements are located at the geometrical center, and the loading is more concentrated. This clearly results in a more onerous condition for this particular mesh.

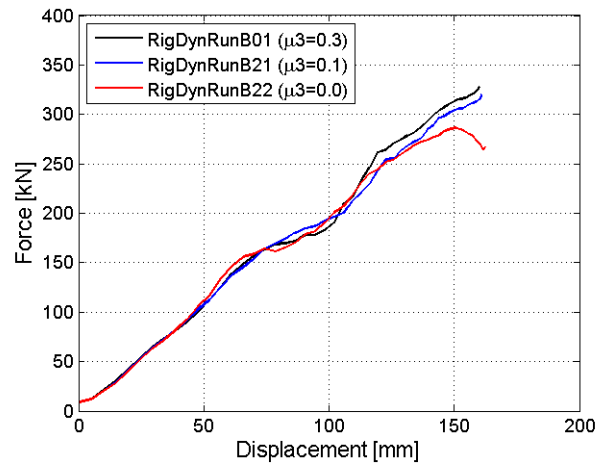


**Figure 4-31: Friction parameter study, indenter B - Varying local friction coefficient between the indenter and the plate ( $\mu_3$ ).**

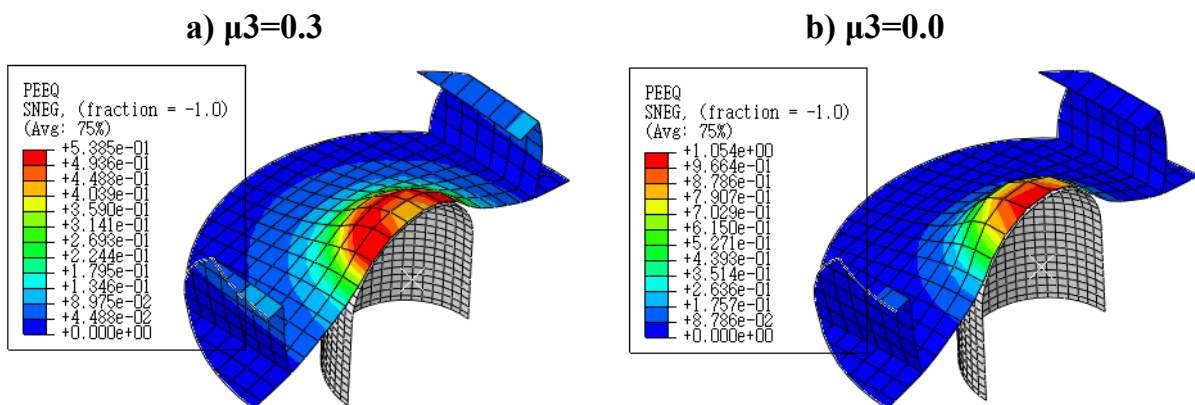


**Figure 4-32: Friction parameter study, indenter B - Varying friction coefficient between indenter and plate ( $\mu_3$ ). Plastic equivalent strains at 145mm indentation.**

Evaluation of the influence of strain hardening

In order to obtain a rough estimate of the influence the strain hardening has on the response of the stiffened steel plate; two simulations using a linear-perfectly plastic material model are performed and compared with the corresponding simulation using the preliminary material model. For the linear-perfectly plastic material model the yield limit is specified as 336MPa, which is the same as the preliminary material model. Additionally a density of 7.85tonnes/m<sup>3</sup> and the elastic properties in terms of a Young's modulus of 210000MPa and a Poisson's ratio of 0.33 is specified. BM1 with both types of indenters is utilized and except for the material definition, the input is as described in section 4.5.2.

From Figure 4-33a it is seen that the force-displacement relation does not vary significantly for simulations with and without strain hardening when the plate is loaded using indenter A. A large part of the load is taken as membrane stretching in the plate and the general strain level is low, thus no significant strain hardening occurs globally. The large strains that occur, accompanied by high degree of strain hardening, are located in relatively small regions in the center stringers or in local areas at the short ends of the oblong indenter.

In Figure 4-33b it may be observed that the results vary in a greater extent when comparing simulations with and without strain hardening for a load by indenter B. Due to severe element deformations for large displacements in the simulation without strain hardening, the results are only presented up to 125mm. Global membrane stretching is a large contributor for the load capacity also in this case. However, at a certain level of indentation, the load bearing capacity of the local plate region between the stringers gets more important as large strains accompanied by a high degree of strain hardening occur in the region that are directly supporting the load.

It is underlined that for a much higher displacement, a greater difference probably would have occurred also in the case with indenter A. However, the performed study gives some further knowledge on the behaviour of the plate subjected to these two different concentrated loads.

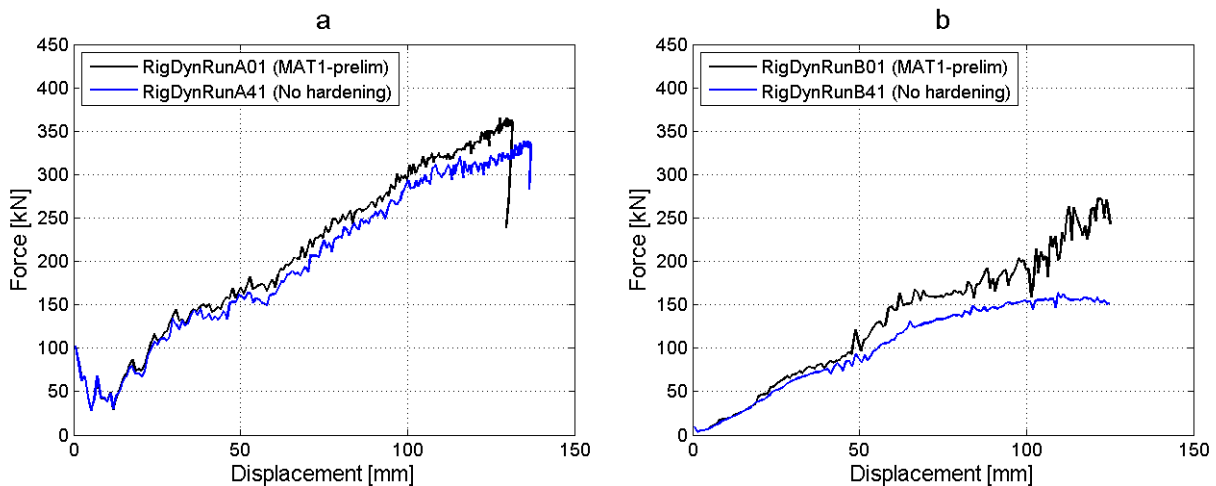


**Figure 4-33: Material parameter study: (a) Results for simulations with indenter A. (b) Results for simulations with indenter B.**

Evaluation of required impact energy

In order to determine reasonable indenter velocities in combination with the predefined mass of 1500kg (preliminary) to be used in the experiments, the impact response for different values are studied. Based on the findings in the previous sections, the approach of modeling the frame with deformable elements is assumed to produce the most reasonable results when the aim is to determine the indenter velocities in the experimental tests in the laboratory. For the simulations with indenter B, a refined mesh (characteristic element size 3mm) is used as this is considered to be critical in order to determine a reasonable velocity. For the simulations with indenter A, the mesh size from the basic computer model is used.

Table 4-8 shows the results from the velocity evaluations for simulations using indenter A. It is noted that the plastic strains in the center region only increases slightly for significant higher impact energies. It is realized that increasing the mesh density (especially at the interface towards the indenter) will increase the strains to some extent, refer to Table 4-6. However, by inspecting the results from the simulations, it is found that while the deformation increases significantly at the supports for an indentation above 150mm, the center region will experience a rigid body translation without any significant increase in the strain level. It is believed that the plate will slide of the supports prior to fracture in the center region for this load condition. The plate deformation at different levels of indentation is illustrated in Figure 4-34.

**Table 4-8: Velocity parameter study - Results from simulations with indenter A.**

<b>Run</b>	<b><math>v_0</math> [m/s]</b>	<b><math>E_{k0}</math><sup>1)</sup> [kJ]</b>	<b>Max force [kN]</b>	<b>Max displ. [mm]</b>	<b><math>p</math><sup>2)</sup> [-]</b>
DefDynRunA01	6	27	322	144	0.23
DefDynRunA31	7	37	356	172	0.25
DefDynRunA32	8	48	400	201	0.28
DefDynRunA33	9	61	414	230	0.30

2) Initial kinetic energy.

3) Maximum equivalent plastic strain in the plate field center region extracted from element integration points.

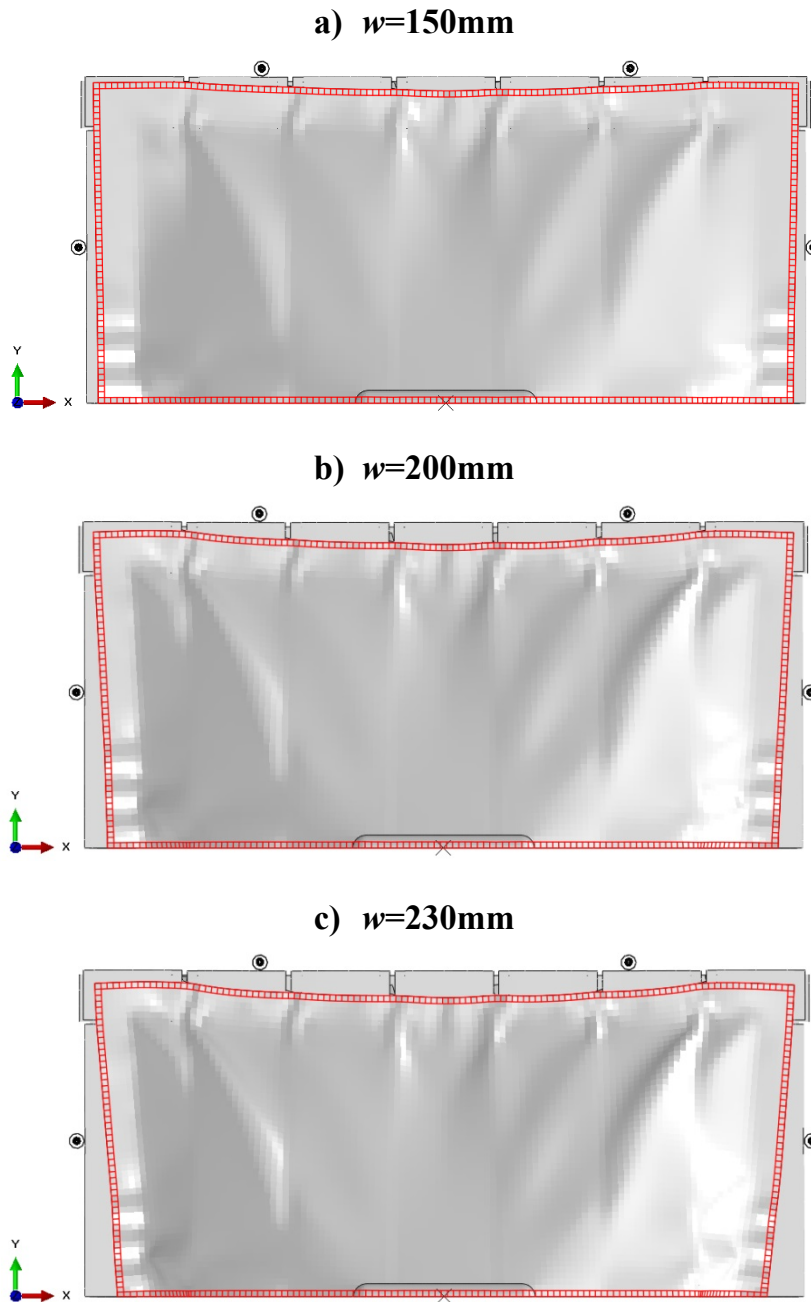


**Figure 4-34: Illustration of plate deformation at supports for a load from indenter A.**

Table 4-9 shows the results from the velocity evaluations for simulations using indenter B. As discussed previously, local necking may be predicted when using element size 3mm for this plate. Based on this, it is estimated that local necking followed by a rapid increase in plastic strains will occur for an impact close to 19kJ.

**Table 4-9: Velocity parameter study - Results from simulations with indenter B.**

Run	$v_0$ [m/s]	$E_{K0}$ <sup>1)</sup> [kJ]	Max force [kN]	Max displ. [mm]	$p$ <sup>2)</sup> [-]
DefDynRunB31	5.5	23	260	-	> 2
DefDynRunB32	5.0	19	260	148	1.21
DefDynRunB33	4.5	15	240	134	0.54

1) Initial kinetic energy.

2) Maximum equivalent plastic strain in the plate field center region extracted from element integration points.

Figure 4-35 shows force-time curves with varying indenter velocity for simulations using indenter A. In Figure 4-35a, it is indicated when the support is activated, defining the end of the fully transient phase of the impact. For all impact velocities it is seen that the oscillations of the foundation reaction force is moderate and that force equilibrium with the indenter contact force is generally maintained throughout the impact duration. Therefore, from a structural dynamic point of view, the frame may be modeled as rigid as it is seen that the dynamic vibrations of the frame (and the plate) is not severe and the response will be almost quasi-static.

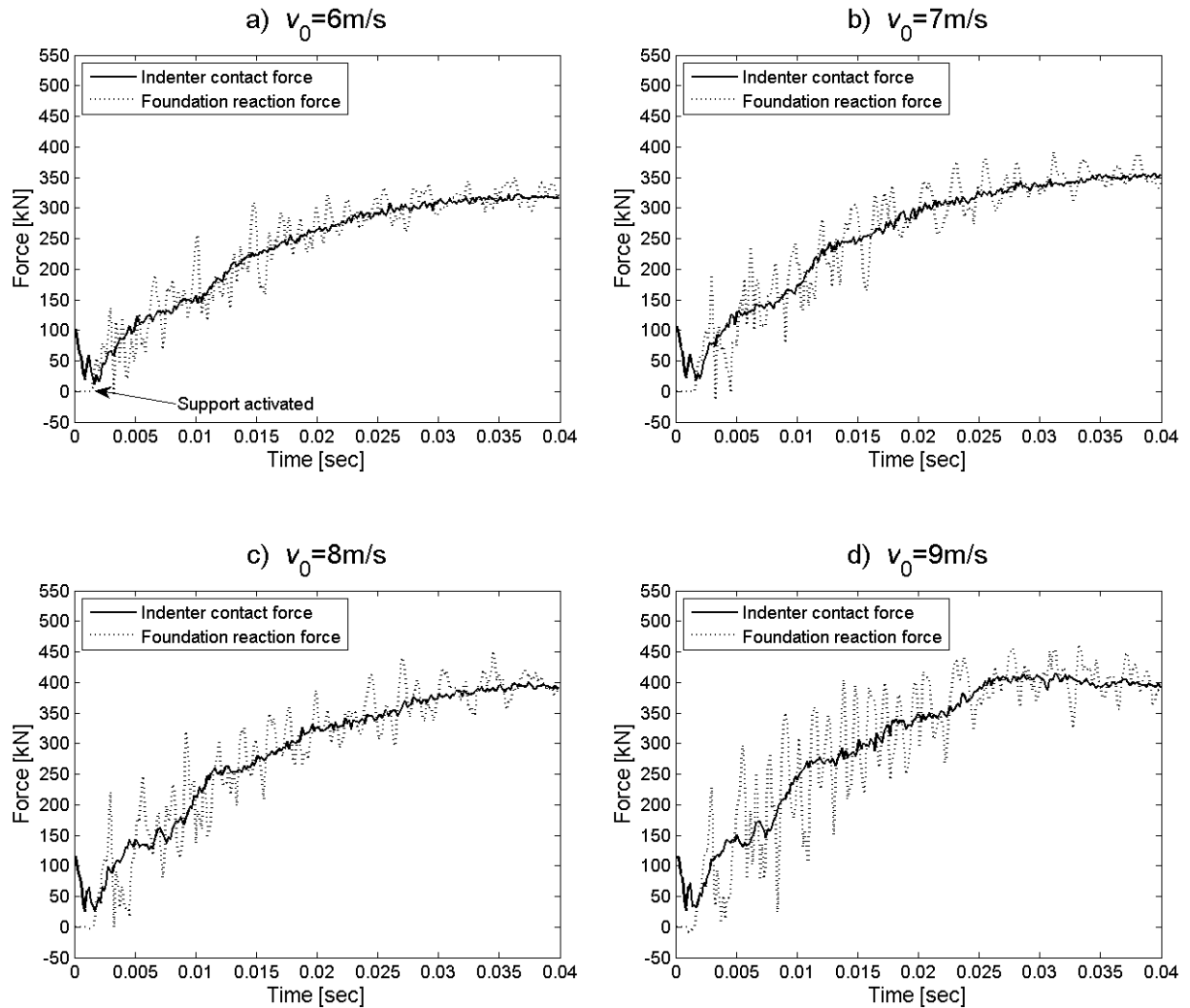


**Figure 4-35: Velocity parameter study. (a), (b), (c) and (d) shows force-time curves for indenter A and varying indenter initial velocity.**

### Evaluation of support frame structural integrity

To demonstrate that the support frame has sufficient capacity to withstand the applied loading during the tests, and to study the structural behaviour of the frame, a design load condition for the frame is established and the corresponding structural response is presented. The analysis chosen as the design load condition for the frame is the dynamic test using indenter A, with an impact of 61kJ (1500kg, 9m/s). This is labeled “DefDynRunA33”, refer to Table 4-8. This condition is evaluated to be governing as it is the impact with the highest energy and the condition that produces the maximum reaction force (414kN).

The equivalent plastic strains in the frame at the end of the simulations are shown in Figure 4-36a. Figure 4-36b shows the von Mises stress at the peak force (0.026sec), while Figure 4-36c shows the deformed frame with a scale factor of 10 and the magnitude of the frame displacements. The force-time curve for this load condition is shown in Figure 4-35d.

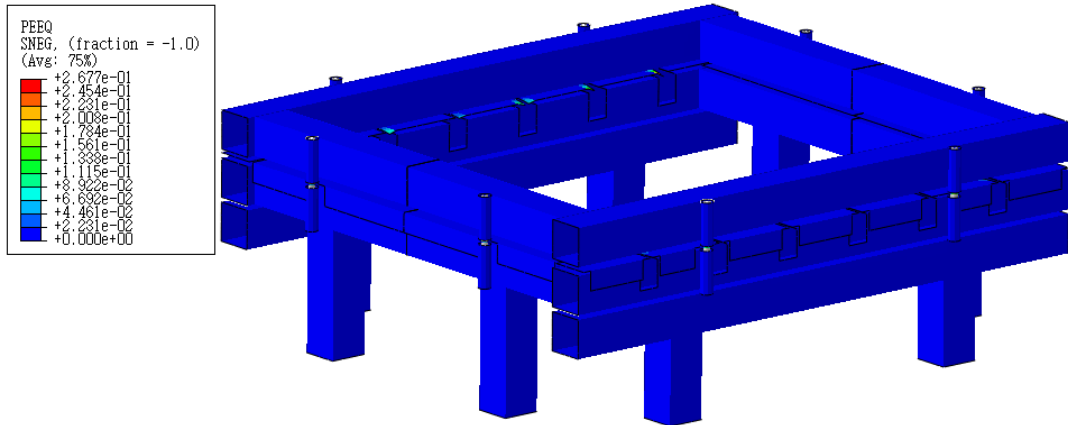
As may be observed the general response of the frame is in the elastic domain. Plastic strains are observed only at local areas at the supports. The shim plates experience a major vertical deformation at the cantilever part due to the action from the plate. However, the effect this permanent deformation has on the overall response of the tests is assumed to be negligible. Considering a ultimate limit state the cross sections of the frame will have sufficient reserve capacity. Nevertheless, a loading above the characteristic load the frame is checked for herein, will be avoided in the experiments to ensure that large permanent deformations does not occur in the frame members.

By inspecting the displacement plot, it is seen that both the top and bottom frame experience global elastic deformations, and this will allow the plates to buckle slightly at the supports due to the axial compression that occurs (as opposed to completely clamped for out-of plane deformations in the idealized model)

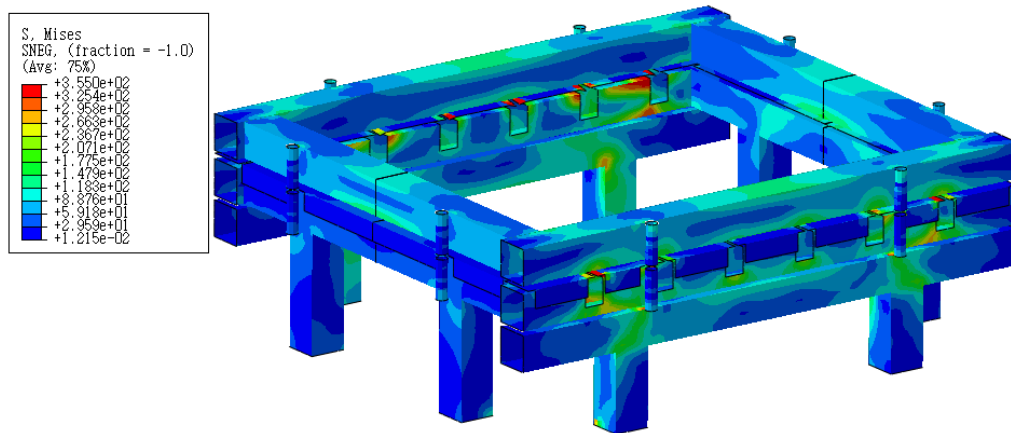
The maximum tension force experienced by the M16 bolts in the analysis is 105kN. The bolts used are in property class 12.9 and has a minimum characteristic tension resistance of 192kN according to ISO 898-1 [31] when considering a coarse standard pitch thread ( $A_s=157\text{mm}^2$ ). This yields a global safety factor of  $192/105=1.82$ . This is evaluated to be sufficient when accounting for uncertainties both on the load and the resistance side, i.e. modeling uncertainties, material properties of the bolt, material properties and strain rate effects of the stiffened steel plate resulting in an increased loading etc.

By simplified calculations and the use of engineering judgement, all welds are found to have sufficient capacity to withstand the applied loading.

a



b



c

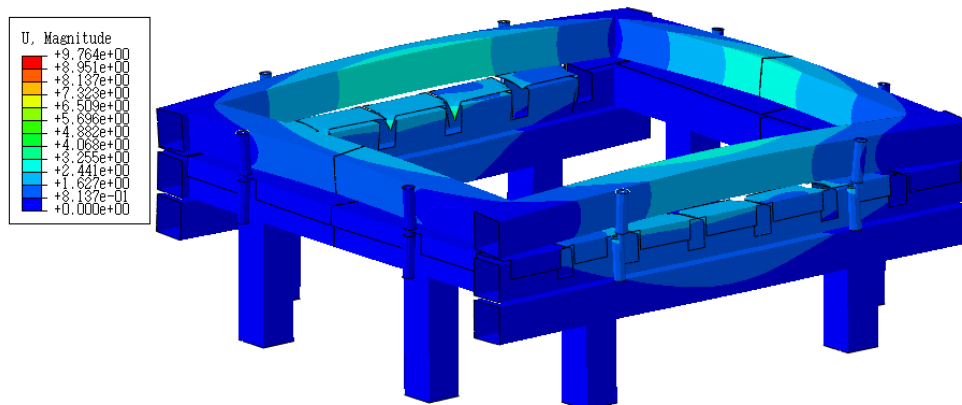


**Figure 4-36: Design condition for frame using indenter A and indenter velocity  $v=9\text{m/s}$ . (a) Equivalent plastic strains of the frame. (b) von Mises stress at 0.026sec. (c) Displacements at 0.026sec (deformed body scale factor 10). The model is mirrored in order to show both sides.**

### Concluding remarks on preliminary simulations of dynamic tests

By comparing the force-displacement curves from simulations using BM1 and BM2 found in Figure 4-21 and Figure 4-24, a few remarks can be made:

- In general, as the force increases the difference in the response from the two basic computer models increases. This is assumed to be mainly caused by elastic deformations of the frame allowing the plate to rotate and buckle slightly at the supports (as opposed to completely clamped for out-of plane deformations in the rigid frame approach).
- At an indentation of 100mm, the force from simulations with indenter A using BM1 is approximately 20% higher than the corresponding simulations using BM2.
- The equivalent difference at 100mm from simulations using indenter B is only 5% as the force is lower with corresponding less deformations of the frame.

The most important findings from the preliminary analysis related to the execution of the experimental programme are summarized below:

- For tests with indenter A, 150mm should be set as the maximum indentation due to the development of severe deformations at the supports for higher indentation, while the center region experience a large degree of rigid body translation without a significant increase in the strain level. An indentation of 144mm is assumed to be achieved for an impact of approximately 27 kJ (1500kg, 6m/s) with a corresponding contact force of 322kN, refer to Table 4-8.
- Based on evaluations of strain levels and distributions, fracture will probably occur for an impact of approximately 19 kJ (1500kg, 5m/s) for tests using indenter B. The corresponding maximum contact force is 260kN, refer to Table 4-9.

Possible strain rate effects are neglected in the preliminary dynamic analysis. Additionally the material properties assumed in the preliminary analysis may differ from those from the actual material that is used. Therefore an approach where the impact energy is gradually increased in the tests will be reasonable.

### **4.5.5 Preliminary simulations of quasi-static tests**

#### General

Analogous to the dynamic simulations reported in section 4.5.4, preliminary simulations of quasi-static tests are performed. Due to similarities, the already performed evaluations regarding mesh density, friction parameters and general computer model accuracy, are considered to be applicable also for the simulations reported in this section.

An evaluation of the indenter velocity for the time scaled quasi-static simulations was performed. The detailed results will not be reported, but will be briefly discussed.

#### Simulations using basic model 1 and 2 with default input

Figure 4-37a shows force-displacement curves for the quasi-static simulations using BM1. The quasi-static analysis using BM1 with indenter A is denoted “RigQSRunA\_01”, while the corresponding analysis with indenter B is denoted “RigQSRunB\_01”.



Figure 4-37b shows force-displacement curves for the quasi-static simulations using BM2. The quasi-static analysis using BM2 with indenter A is denoted “DefQSRunA\_01”, while the corresponding analysis with indenter B is denoted “DefQSRunB\_01”.

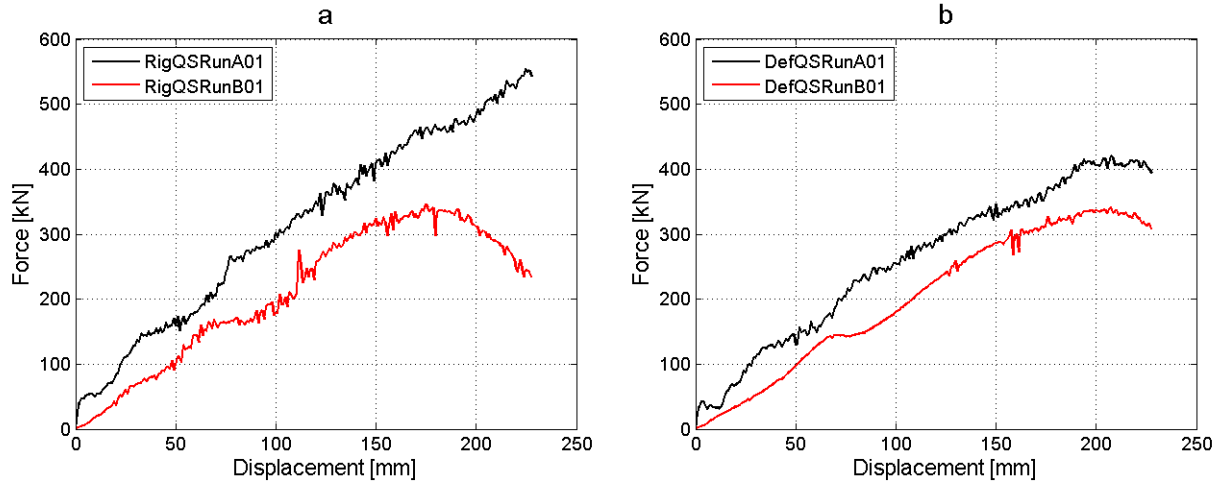


**Figure 4-37: Preliminary quasi-static run with basic computer model default input: (a) Results for BM1. (b) Results for BM2.**

#### Concluding remarks on preliminary simulations of quasi-static tests

By inspecting the force-displacement curves from the preliminary quasi-static simulations, and comparing with the force-displacement curves from the preliminary dynamic simulations, a few remarks can be made:

- Except from the initial transient phase before the supports are activated in the dynamic simulations using indenter A, the force-displacement relation from the dynamic and quasi-static simulations have similar slope. For indenter B, neither the initial or global phase of the force-displacement relation differs significantly from the corresponding dynamic simulation.
- The difference in the load response from quasi-static simulations using BM1 and BM2 is similar as those identified for the dynamic simulations.
- The remarks regarding proposed values of indentation and expected forces to occur in the dynamic tests are also applicable for the quasi-static tests.

The dynamic response due to the time scaling is evaluated. Based on the findings it is concluded that the basic model default indenter velocity of 6m/s should be used as the maximum value for this specific simulation in order to obtain sufficiently accurate results. By studying the energy history for this time period, the kinetic energy is found to be in general low throughout the analysis. However, it is found that by reducing the velocity, the slope of the force-displacement curves in the initial phase reduces (approximately up to 10mm displacement). This is especially noted for simulations using indenter A which displays a more global load response. Otherwise the response of the curves has converged, and the analysis can be accepted as quasi-static. Using a lower velocity in the analysis will be considered when comparing results with those obtained from tests. Alternatively a more gradual increase in the velocity will be considered.

As for the dynamic simulations, the energy balance is checked to be close to constant and the artificial energy and penalty energy is very low compared to the internal energy.

**4.5.6 Calculation of stiffened steel plate initial bending capacity**

As previously discussed, initial bending and shear resistance occurs when the stiffened steel plate is loaded from a concentrated load using indenter A. In this section this initial resistance that occurs for small displacements is estimated by simplified hand calculations in order to obtain further knowledge of the behaviour of the stiffened steel plates.

In the following calculations it is assumed that only the center region of the plate field that involves two stringers contribute to the resistance. This is reasonable considering the distribution of the applied load. The bending and shear capacity is calculated considering the stringer with plate as a beam. Local buckling of the subpanels between stringers is accounted for by calculating an effective width of the compression part according to NS-EN-1993 1-5 [32]. The resulting effective cross section of one “beam” is shown in Figure 4-38:

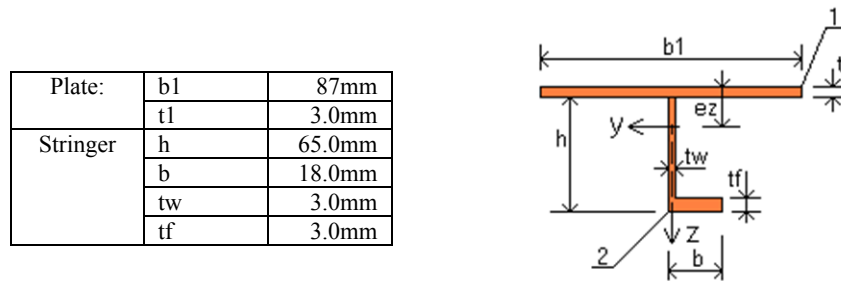


**Figure 4-38: Cross section geometry of effective beam.**

In the cross section shown, the elastic neutral axis is located 20.6mm from the top while the plastic neutral axis is located 2.9mm from the top. Assuming the yield strength from the preliminary material model, 336MPa, the corresponding characteristic elastic and plastic bending resistance is 2.14kNm and 3.22kNm respectively. The plastic shear resistance is 36.08kN.

Based on the rotation of the cross-section shown in Figure 4-39a, which originates from the preliminary simulations, it is reasonable to assume a simply supported beam as shown in Figure 4-39b when calculating the load capacity based on initial bending. As the stringer is not restrained at the support, it is only the out-of plane bending resistance of the plate which resists rotation of the considered beam cross section at the support. Considering a simply supported beam of length 1.05m subjected to a point load, the corresponding combined characteristic load capacity for the two center beams is given in Table 4-10.

**Table 4-10: Characteristic load capacity of effective cross sections.**

Analysis	Characteristic load capacity [kN]
Elastic	16.3
Plastic	24.5

The load level when considering a fully plasticized cross section coincides well with the initial load level observed from the quasi-static simulations; refer to the force-displacement curve in Figure 4-37. However, by inspecting the stress distribution in the numerical simulations it is observed that membrane stresses in the plate and bending stresses in the

remaining stringers have arisen before the center cross sections are fully plasticized. The performed calculations are very conservative due to the simplifications made when neglecting the fact that the plate is clamped at the support and neglecting the contribution from the remaining parts of the plate field, and should not be compared directly with the real situation. Nevertheless, the calculations give some insight in the very initial phase of the behaviour of the stiffened steel plate subjected to a load from indenter A.

It is of course possible to further assess the bending capacity for large displacements by means of plastic hinges and yield lines. However, such analytical methods usually rely on idealized support conditions different than those in the current model and are therefore suspected to give inaccurate results.

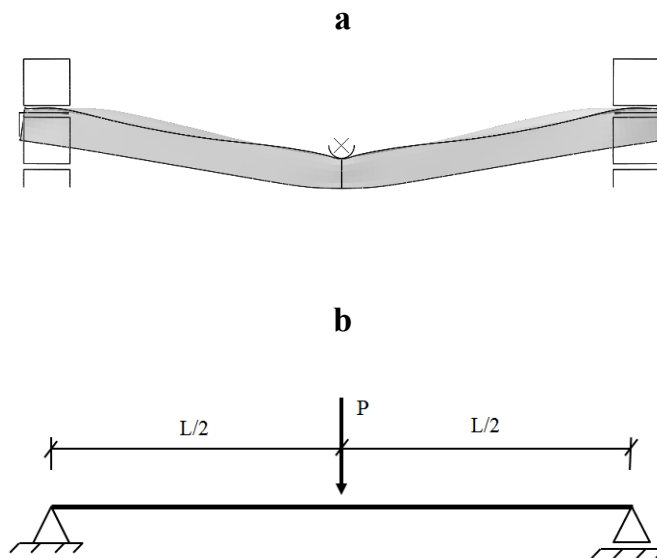


**Figure 4-39: (a) Deformation of center stringers subjected to point load from numerical simulations. (b) Simply supported beam with point load  $P$ .**

## 4.6 Set-up of quasi-static tests

The quasi-static tests are conducted in the rig illustrated in Figure 4-40. The support frame designed for the current study, is positioned onto an existing steel frame for practical reasons. Plate indentation is enforced by a hydraulic jack *RDP-Howden-Ltd* with a capacity of 1000kN. The plates are loaded in displacement control at a rate of 10mm/min.

An *HBM UI5/1MN* load cell (maximum capacity of 1000kN) is attached to the cross head of the cylinder to measure the contact force towards the plate. For displacement measurements it is desirable to measure the relative distance between the cross head/load cell and the supports of the test specimen. The displacement of the jack cross head is measured by the cylinder itself. However, these measurements will not be used. Due to the size of the rig and the large forces involved, the rig is expected to stretch making these displacements higher than the real displacements.

Instead it was decided to measure the relative distance between the load cell and two appropriate locations on the bottom frame. The two locations were chosen based on results from preliminary analyses which showed they would only experience very small displacements during loading. These locations are the two ends without cut-outs for stringers. The small displacements at these locations may be seen from Figure 4-36. The displacement between the bottom frame and the load cell was measured by using an optical displacement sensor (ODS) with a measuring range of 200mm attached to the bottom frame. The targets for the two optical displacement sensors were taken as a horizontal bar attached to the load cell. Figure 4-41a shows the load cell with the attached horizontal bar, while Figure 4-41b shows the ODS pointing towards the bar.

It is worth mentioning that in the very first test that was performed, the displacement was only measured at one side of the frame. However, it was detected that a slight tilt of the entire cross-head occurred during loading. Based on this, it was decided to measure the displacement at two locations, allowing the magnitude of the tilt to be recorded.

Additionally two cameras are set up to record images every 1sec. The cameras are located below the support frame and may be seen in Figure 4-40. Only a small region at the center of the plate is covered by the cameras.



Figure 4-40: Quasi-static test - Support frame installed in test machine.

a



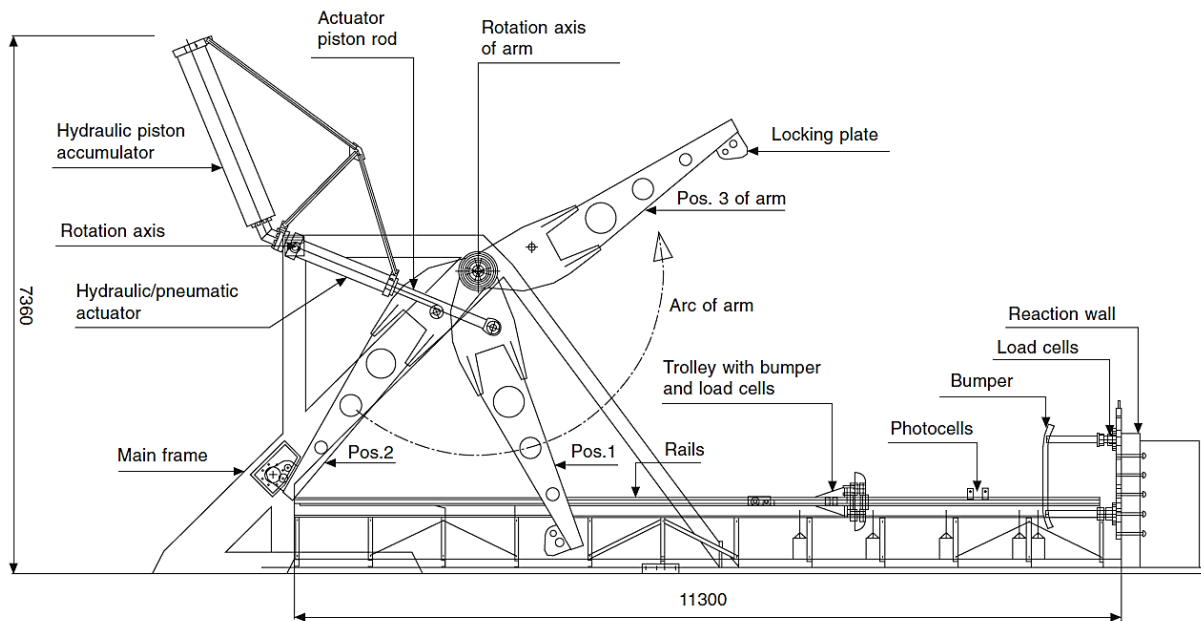
b



Figure 4-41: Quasi-static test: (a) shows the load cell and attached horizontal bar. (b) shows the ODS pointing on a reference point on the horizontal bar.

### 4.7 Set-up of dynamic tests

The dynamic tests of the stiffened steel plates were conducted using the kicking machine developed at SIMLab, NTNU [24]. The kicking machine is a device for impact testing of structural components, and it is for instance used for testing of automotive bumper systems. The kicking machine with a typical experimental test set-up for bumper systems is illustrated in Figure 4-42. The system consists of an arm that rotates around a set of bearings. The arm is connected to a hydraulic/pneumatic actuator system, which provides the moving force. This system accelerates a trolley moving on rails up to the desired impact velocity. The trolley subsequently hits the test specimen fixed to a reaction wall at the far end. For a detailed description of the operation of the machine it is referred to the paper by Hanssen et al. [24].



**Figure 4-42: Illustration of the kicking machine at SIMLab, NTNU. [24]**

Figure 4-43a shows the test rig with specimen positioned onto the reaction wall. The test specimen is installed into the test rig frame in advance when it is positioned in a horizontal position. The complete test rig assembly is then lifted and installed into brackets welded towards the reaction wall and fastened via bolting. The bracket and bolting is shown in Figure 4-43b. Next a weld is added between the frame and the reaction wall. These welds are expected to transfer the major part of the load during testing.

Figure 4-44a shows the trolley. The trolley is equipped with a load cell and the force signal is used to obtain the acceleration, velocity and displacement history of the trolley, and the size of the impact force by the following equations.

$$\ddot{w} = -\frac{P(t)}{M_B} \tag{4-1}$$

$$F(t) = P(t) - M_N \ddot{w} \tag{4-2}$$

Here  $w$  is the displacement of the trolley measured from the moment of impact,  $P(t)$  is the force history from the load cell,  $M_B$  is the mass of the trolley located at the rear side of the load cell,  $M_N$  is the mass of the nose located in front of the load cell (indenter and attachment plate), and  $F(t)$  is the impact force acting directly on the test specimen. A rigid body diagram of the set-up is shown in Figure 4-45. As the support frame is rigidly attached to the reaction wall, it can be considered to be a part of the reaction wall in the diagram.

By inserting Equation (4-1) into Equation (4-2) the impact force may be expressed as:

$$F(t) = P(t) \left( 1 + \frac{M_N}{M_B} \right) = P(t) \cdot \gamma_{\text{force}} \quad (4-3)$$

Here,  $\gamma_{\text{force}}$  is referred to as a force factor.

The total weight of the trolley ( $M_B + M_N$ ) used in the experiments was (1373+58)kg=1431kg for tests with indenter A, and (1373+56)kg=1429kg for tests with indenter B. The corresponding force factors are 1.0422 and 1.0408 for tests with indenter A and B respectively.

The impact velocity  $v_0$  of the trolley is measured by a system of photocells located directly in front of the impact area. The photocells are shown in the lower left corner in Figure 4-43a. Two high-speed video cameras record the event at approximately 15000 frames per second. The cameras were installed on the outside of a protection cage and may be seen to the far right in Figure 4-44b. The recorded digital images are also used to find the velocity and displacement of the trolley during the impact, as an additional check of the data obtained based on the force signal from the load cell. This is done by a method referred to as *Harris & Stevens Corner Finder*, by tracking a few corners in the pattern indicated in Figure 4-46.

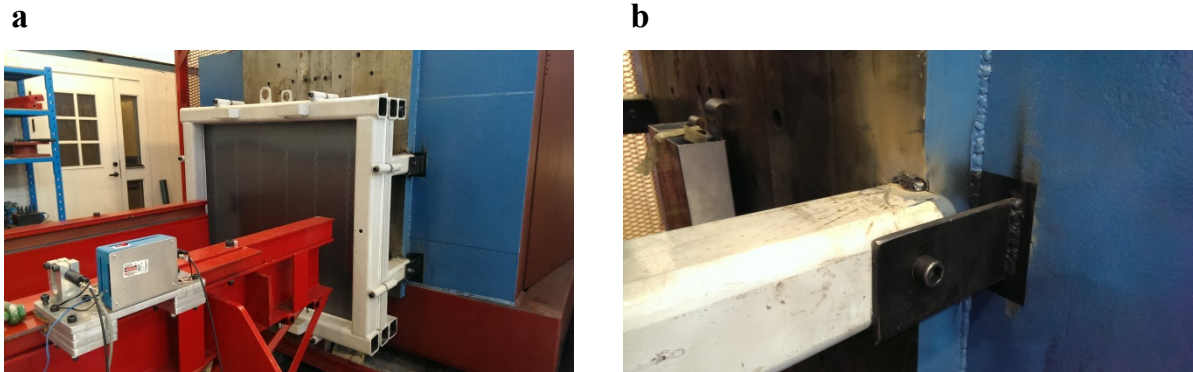


**Figure 4-43: Set-up of dynamic tests: (a) Picture of test rig assembly installed on reaction wall. (b) Close up view of attachment towards reaction wall.**

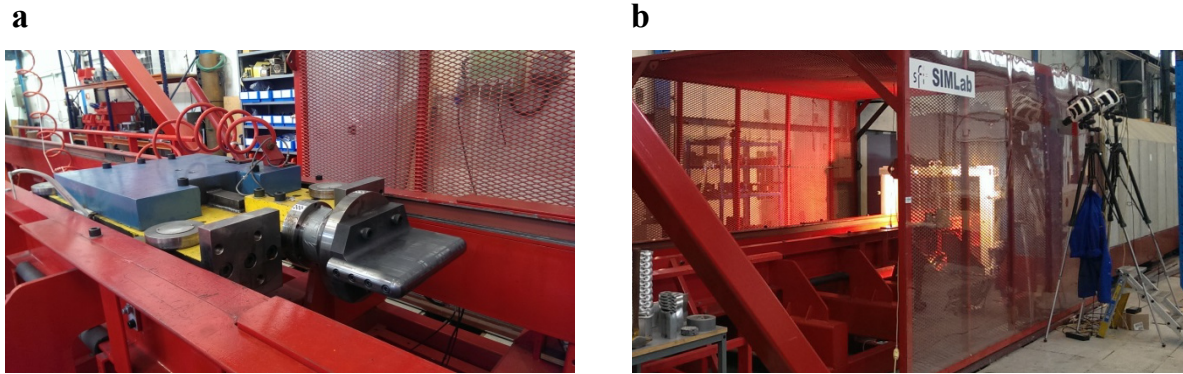


**Figure 4-44: Set-up of dynamic tests: (a) Picture of trolley. (b) Picture of test rig assembly installed in protection cage.**

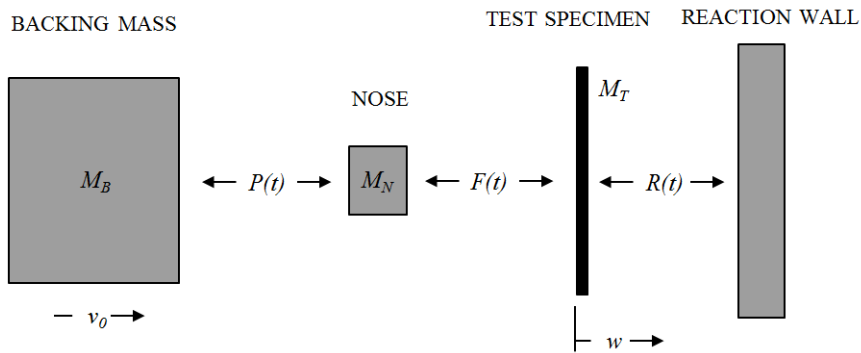


**Figure 4-45: Set-up of dynamic tests: Rigid-body diagram.**

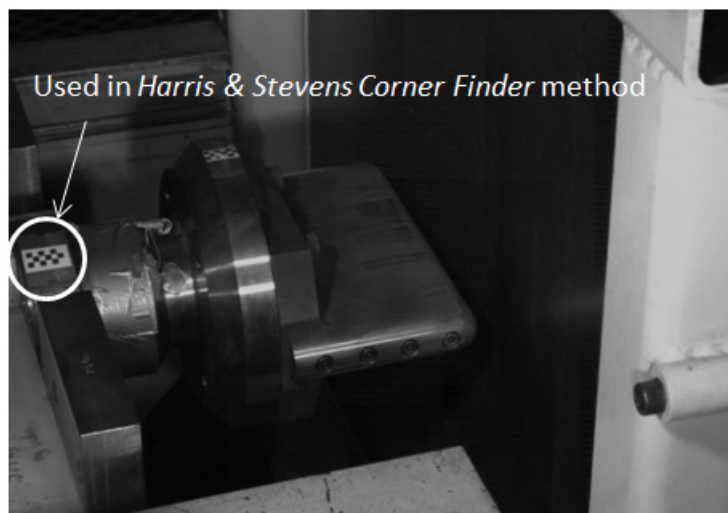


**Figure 4-46: Pattern used in *Harris & Stevens Corner Finder* method.**



## 4.8 Test program

In total four quasi-static tests, and four dynamic tests were performed using both indenter type A and B. As identified during the preliminary analysis, the displacement controlled quasi-static tests using indenter A should be stopped at maximum 150mm to avoid severe deformations at the supports. Just prior to the tests, quasi-static simulations using a material model calibrated from tension tests performed on the actual material (MAT1a, as presented in section 3.2) was performed. The results indicated that the loads would be slightly higher than in the preliminary analysis performed, mainly due to higher yield strength of the material. However, the corresponding load at 150mm indentation was still estimated to be below 414kN which was the characteristic load used to validate the structural integrity of the frame.

The quasi-static tests and the preliminary analysis were used as a reference when determining impact energies appropriate for the dynamic tests. Based on force-displacement measurements from the static tests, energy-displacement relations were calculated, and the energy level at fracture could be estimated. However, a few other practical considerations also affected the determination of appropriate impact energies. The details regarding the impact velocities with corresponding impact energies used in the tests, and details regarding the execution of the dynamic tests will be presented when discussing the results from the dynamic tests.

Table 4-11 gives an overview of the quasi-static and dynamic tests performed.

**Table 4-11: Overview of tests.**

	<b>Indenter</b>	<b>Test identifier</b>
<b>Quasi-static</b>	A	QSA1
		QSA2
	B	QSB1
		QSB2
<b>Dynamic</b>	A	DynA1
	B	DynB1
		DynB2
		DynB3

All test specimens was visually inspected for possible large imperfections prior to the tests. The main dimensions, i.e. height, width and center distances of the stringers, were inspected and checked for possible obvious deviations from the design drawings. Systematic control measurements of the plate and stringer thicknesses were conducted on four of the test specimen by using a micrometer. The plate was measured at six distributed locations, while each stringer was measured at one location. No significant deviations from the nominal measurements were detected. For the plate part, the maximum mean value for a specimen was 2.99mm, while the minimum mean value for a specimen was 2.98mm. For the stringers the maximum mean value of all six stringers within a test specimen was 3.05mm, while the corresponding minimum mean value for a test specimen was 3.02mm. However, as similar systematic measurements were not conducted consistently on all test specimens, the detailed results are not included in this report.



## 5 RESULTS FROM COMPONENT TESTS

### 5.1 Results from quasi-static tests

#### 5.1.1 General

This part presents the results from the quasi-static tests conducted. Both force-displacement and energy-displacement curves will be presented. The presented energy is calculated by integrating the interface force over the displacement and up to the maximum force it corresponds to the externally applied work. This is equivalent as the sum of the elastic strain energy and dissipated energy. If the unloading phase is included, the remaining energy level represents the total energy dissipated during the test. In section 5.1.4 an evaluation of the test data accuracy will be made.

#### 5.1.2 Load from indenter A

The force-displacement curves and energy-displacement curves from the quasi-static tests using indenter A is shown in Figure 5-1. A picture of specimen QSA1 after the test is shown in Figure 5-2. For the first test, QSA1, the maximum force recorded was 385kN. The test was stopped at an indentation of 150mm, and as expected, no fracture occurred.

As contact is taking place directly above two stringers, a bending and shear resistance is experienced in the initial stage as demonstrated in section 4.5.6. At a load level of approximately 30kN, the initial resistance dominated by bending resistance is reached and the stiffness reduces. This load level coincides well with the estimated resistance for the initial bending action as reported in the preliminary analysis when accounting for the increased yield strength from the preliminary analysis. As the indentation continues, the two center stringers start tipping towards the center just as observed in the preliminary analyses. At approximately 50mm, 100mm and 125mm indentation diffuse bumps in the force-displacement curve is observed. By inspecting the recorded images, it is seen that at the tipping motion of the stringers start to accelerate at approximately 100mm indentation. However, the images revealed no specific behaviour at the other levels of indentation. Another source of these bumps is probably that the contact regions at the supports vary throughout the test, which again affects the overall stiffness of the system. The latter statement is difficult to verify as these locations were not monitored during the test. However, similar bumps were observed in the preliminary analyses.

After the first test, a few bolts had to be cut in order to remove the specimen from the support frame. The bolts were difficult to remove without damaging the threading as high residual tension forces remained after unloading the plate. The tension forces arise due to buckling of the plate at the supports, pushing the top frame upwards. The location of this buckling is indicated on Figure 5-2. Buckling did also occur at the transverse supports of the plate, although to a lesser extent. Based on this experience it was decided to stop at 200kN in the second test in an effort to avoid damaging further bolts in the quasi-static tests. Limited buckling at these locations was predicted in the preliminary analysis. However, the observed deformations in the test was more severe than in the simulations, probably due to higher

flexibility (reduced stiffness due to Teflon sheets is neglected in the computer model). Nevertheless, as seen from the results, the agreement obtained between the two tests is very good.

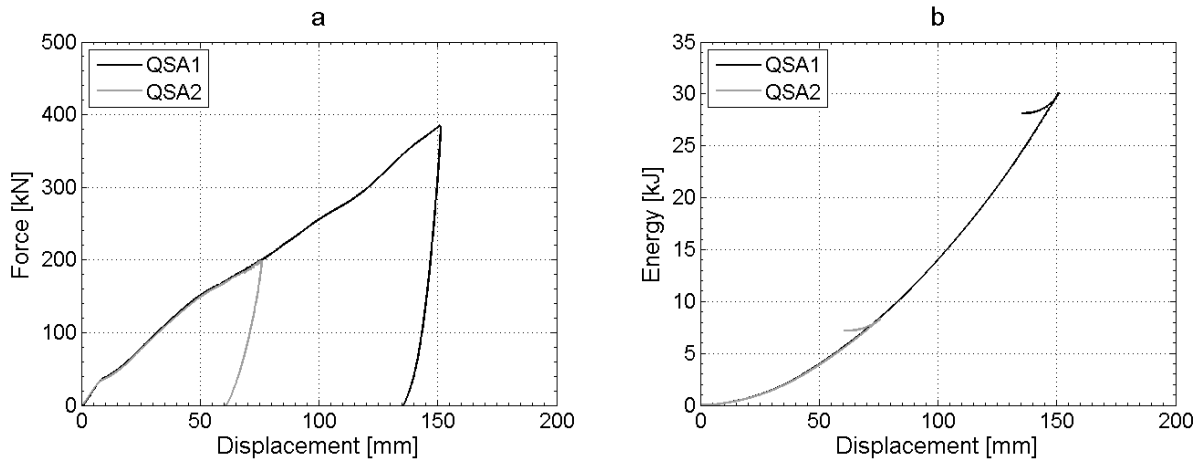


**Figure 5-1: Results from test No. QSA1 and QSA2.**



**Figure 5-2: Picture of test specimen QSA1 after unloading.**

### 5.1.3 Load from indenter B

Force-displacement curves and energy-displacement curves from the quasi-static tests using indenter B are shown in Figure 5-3. Both specimens were loaded until fracture occurred. The maximum force recorded from the first test, QSB1, is 246kN. In the second test, QSB2, the maximum force is 252kN.

By inspecting the initial phase of the force-displacement curves, approximately up to 15mm indentation, it is seen how the stiffness gradually is increasing. This is a direct result of the increasing effect of the membrane forces in the plate as the angle between the applied load and the plate reduces. As may be observed from the figure, the slope of the curve is slightly steeper for QSB1. Naturally some difference in response should be expected, due to small variations in geometry and material properties between the test specimens. The slight reduction of the stiffness for the second test may also be a consequence of the permanent deformations that occurred in the shim plates during test QSB1 which was the very first test conducted using the test rig. These deformations were anticipated and are briefly mentioned when assessing the structural integrity of the frame based on preliminary simulations, and are shown on Figure 4-36.

Similarly as observed for the tests using indenter A, a few diffuse bumps on the force-displacement curves are observed, although they are slightly less distinct. As for the first two tests, these bumps are probably related to the tipping motion of the stringers and varying contact action between stringers and frame at the supports.

In Figure 5-4a, which shows a picture from the center region just prior to fracture, a narrow band that appears to be a local neck may be observed. Shortly after, fracture occurs, and the crack propagates in a way that the plate immediately loses most of its load bearing capacity. For both tests the fracture zones were similar as shown in Figure 5-4b, and the remaining force after fracture was approximately 18% of the fracture force. From Figure 5-5a it may be seen that a significant thinning has taken place at the location of this narrow band. Further it is seen that the fracture planes away from this area seems to be inclined. Similar inclined crack planes, which were typical for the entire fracture zone, are better illustrated in the picture in Figure 5-5b. The fracture plane at the location where the narrow band was observed does also appear to be inclined, although with a lower angle towards the through thickness direction.

In these cases, it appears that instability initiated as a local neck at the location shown, and then developed into a through thickness shear instability which typically displays inclined fracture planes, similar as described in section 2.3.5. In the contact region towards the indenter with the hemispherical geometry, the plate will almost be in an equi-biaxial tension stress-state. The development of inclined fracture planes, which indicate some sort of through thickness shear instability, is in line with the results reported by e.g. Gruben et al. [18] in the study of ductile fracture of a dual-phase steel for a range of stress-states spanning from uniaxial tension to equi-biaxial tension.

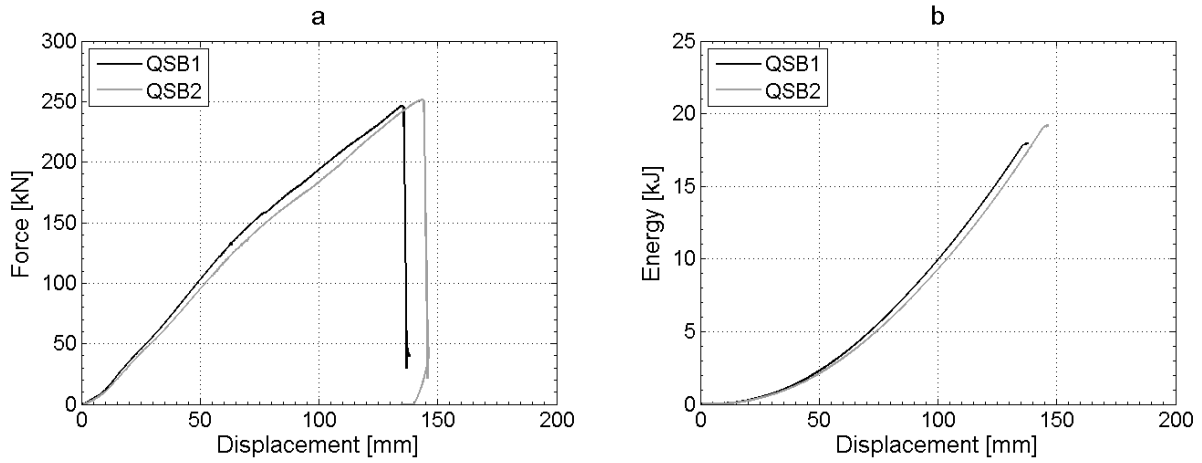


Figure 5-3: Results from test No. QSB1 and QSB2.

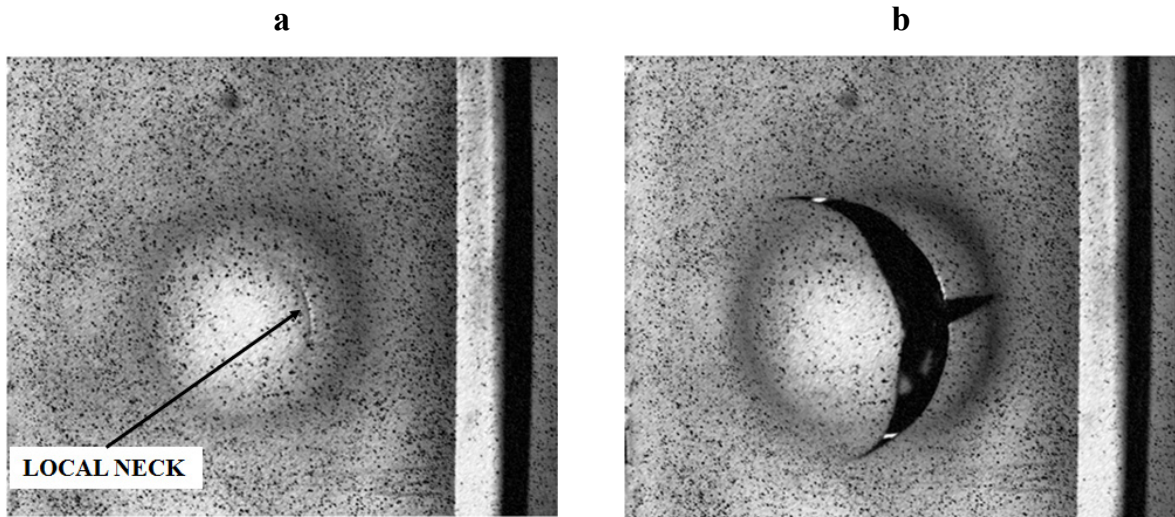


Figure 5-4: Pictures of test specimen: (a) and (b) shows the center region of test specimen QSB1 just prior and after fracture.

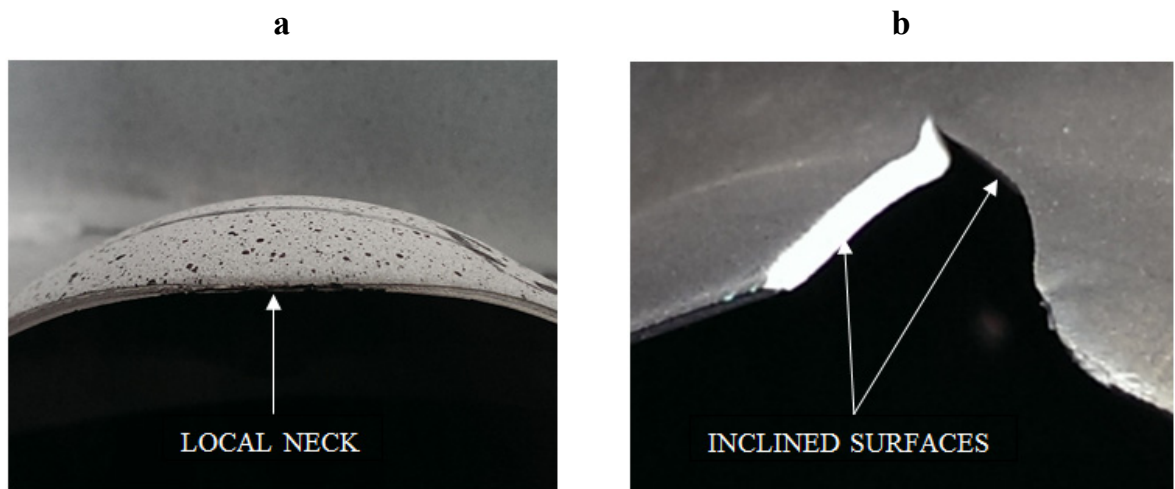


Figure 5-5: Pictures of test specimen: (a) Side view of fracture zone (QSB1). (b) Close up view of crack faces (QSB2).

### 5.1.4 Test data accuracy

The displacement measurements from the two lasers revealed a maximum deviation of 4mm between the two sides during both tests with indenter A. With a length of 1300mm between the two lasers, the corresponding maximum tilt of the cross head was 0.18 degree which is within the expected limit considering all relevant tolerances involved. The resulting displacements for these tests are taken as the average value from the two laser measurements.

The displacement from QSB2 was measured by using two lasers similar as for the tests using indenter A. Also for this test, the maximum deviation was approximately 4mm, and the resulting displacement is taken as the average value between these two measurements. QSB1 was the very first quasi-static test to be conducted on the stiffened steel plates. As described in section 4.6, the displacement was only measured at one side of the frame in this test. It is reasonable to assume that also in test QSB1 a similar tilt of the cross head occurred during loading. This implies that the displacement measurement from this test probably is off by 2mm. However, this is considered to be negligible.

Alsos et al. [6] performed quasi-static indentation tests of stiffened steel plates at an indentation velocity of 10mm/min with the velocity of 1mm/min for short periods of time in order to assess the effect of strain rates. A 1-2% increase in the load was observed when using an indentation velocity of 10mm/min compared to the reduced velocity. It is reasonable to assume that a similar strain rate effect was present in the current quasi-static tests as the same indentation velocity was used. This will be considered when comparing results from the experiments with those obtained from numerical simulations.

## 5.2 Results from dynamic tests

### 5.2.1 General

This part presents the results from the dynamic tests conducted. The acceleration during the impact may be found by Equation (4-1), which again allows the determination of the velocity and displacement histories by integration. The impact force is found from Equation (4-3).

As described in section 4.7, the high speed camera recordings may also be used to find the acceleration, velocity and displacement history. By comparing the displacement and velocity histories based on the two separate measurements, a very good agreement was found for the test involving indenter A. However, for the three tests using indenter B, there is a noticeable deviation in the measurements. The results presented in section 5.2.2 and 5.2.3 is those obtained directly from the measurements of the load cell. In section 5.2.4 a comparison of the displacement and velocity histories based on the two measurement approaches will be presented and the test data will be evaluated.

### 5.2.2 Load from indenter A

No fracture occurred in the quasi-static tests with indenter A for the applied load level. A similar result was expected for the dynamic load condition, and it was decided to conduct only one dynamic test using a moderate velocity. Results from the dynamic tests using indenter A are shown in Figure 5-6. The impact velocity recorded is indicated in the figure. In the force-displacement and energy-displacement plots, the results from the static test QSA1 is included for comparison. Considering this is an impact condition, it could be more intuitive to present the energy in terms of a reduction in projectile kinetic energy over the displacement. However, to simplify the comparison with the results from the quasi-static tests the presented

energy is calculated similarly as described in section 5.1 which is equivalent as the sum of the elastic strain energy and dissipated energy. The unloading phase (due to indenter rebound) is included and the remaining energy level corresponds to the dissipated energy during the impact. The deformed shape of the test specimen after unloading did not deviate from the corresponding quasi-static tests. Pictures before and after the impact for test DynA1 are shown in Figure 5-7.

By inspecting the results, it is seen that the static and dynamic response is similar for the tests conducted. As expected all the impact energy was absorbed without any fracture in the dynamic test. Similarly as identified in the preliminary simulations, dynamic oscillations occur in the initial phase of the impact. A slight increase in the stiffness compared to the corresponding static response may be observed for the dynamic test, probably due to strain rate effects. The latter statement is substantiated considering that the maximum force is reached at 0.03sec when the indenter velocity still is approximately 1m/s. At zero velocity, the force has reduced.

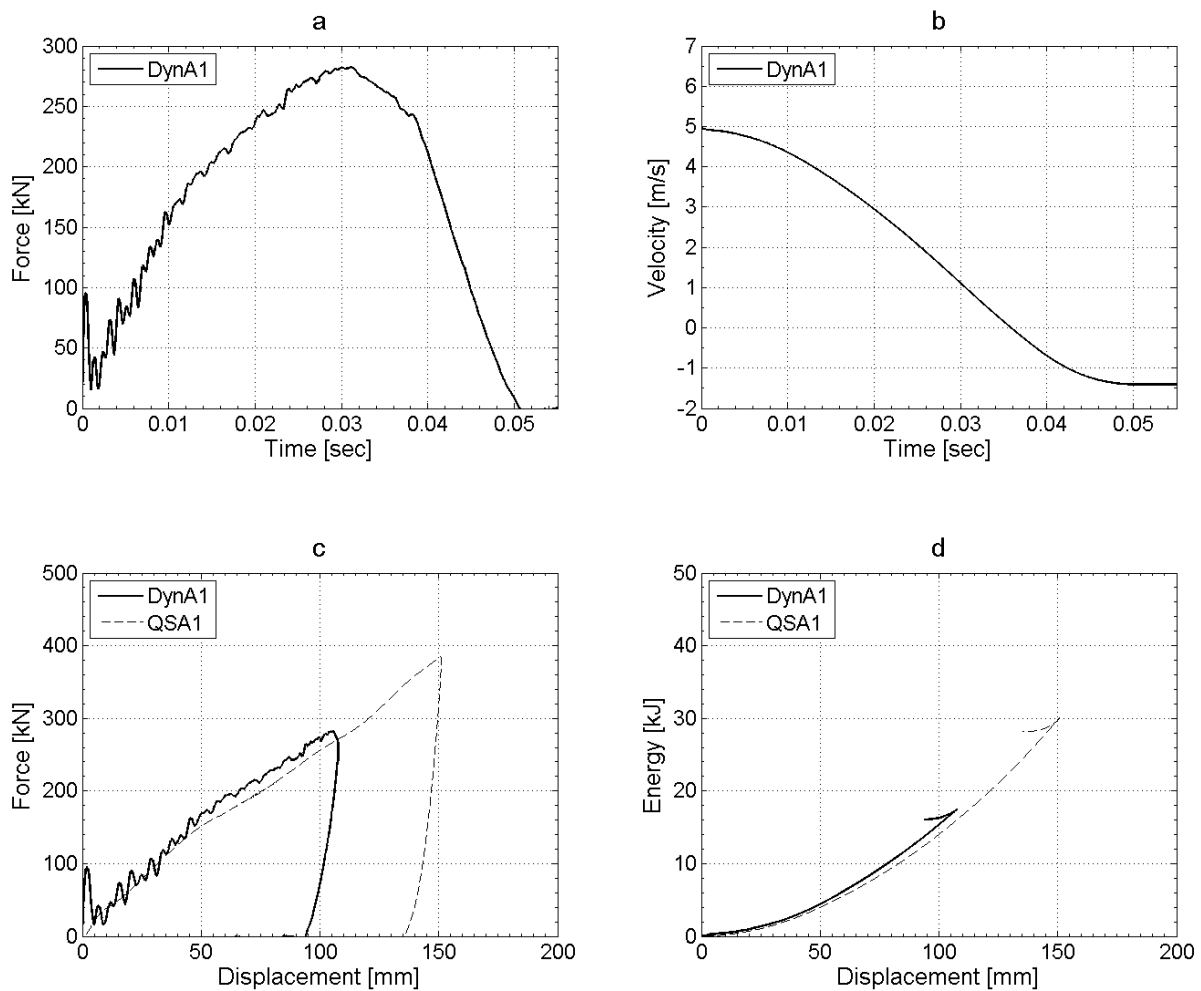
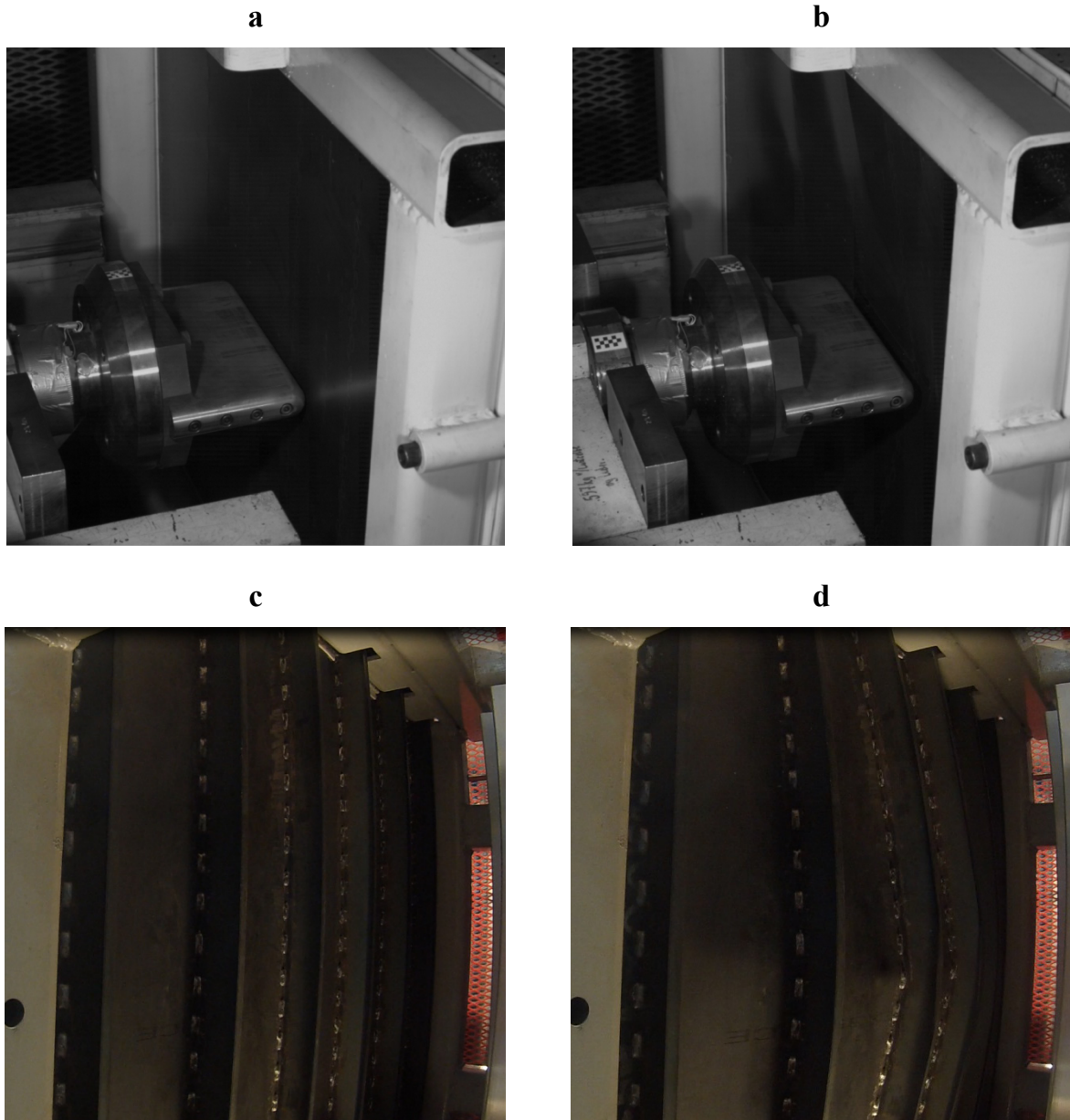


Figure 5-6: Results from test No. DynA1,  $M=1431\text{kg}$ ,  $v_0=4.95\text{m/s}$





**Figure 5-7: Pictures of test specimen DynA1. (a) and (c) Prior to impact. (b) and (d) After impact.**

### 5.2.3 Load from indenter B

Beforehand, the energy required to obtain fracture in the dynamic tests were assumed to be equivalent as the corresponding static ones. In the static tests, the maximum absorbed energy was approximately 19kJ. To obtain this energy in the tests, the corresponding impact velocity would be 5.2m/s when using a trolley mass of 1429kg. However, it was decided to increase the velocity slightly to assure that fracture occurred in the tests. In the first test conducted, DynB1, the impact velocity used was 5.7m/s (23.2kJ). This was found to be more than required to achieve full penetration of the plate and the residual energy was absorbed when the bolted flange of the indenter impacted the test specimen. For consistency the second test, DynB2, was conducted using a similar velocity. In the third and final dynamic test using indenter B, DynB3, the impact velocity was reduced. The motivation was to study whether any visual signs to material instability could be detected in a specimen loaded just below the fracture load.

Results from the dynamic tests using indenter B are shown in Figure 5-8, Figure 5-9 and Figure 5-10. Only the relevant data is included, i.e. the response when indenter attachment flange hits the test specimen is omitted. The energy is calculated similarly as previously described. The impact velocity recorded is indicated in the figures. As for the test using indenter A, the results from the static test are included for comparison. Pictures before and after the impact for test DynB1 are shown in Figure 5-11.

Based on the force-displacement curves, it seems that there is no increase in stiffness compared to the quasi-static tests as observed for test DynA1. Further the fracture load seems to be lower. However, as will be discussed in section 5.2.4 this might be a result of the deviations in the measurements.

For the two first test specimen, the fracture energy was lower than observed in the quasi-static tests. The difference in response between the two first dynamic tests which were conducted with approximately the same velocity is similar as the difference between the two static tests. The force-displacement curves just prior to fracture seems to be somewhat smoother than what was observed in the static tests, indicating a more gradual reduction in stiffness. Also for the last dynamic test without fracture, the stiffness seems to reduce when approaching the maximum load. In the latter case the reduced stiffness towards the end of the impact is probably a direct result of reduced strain rates as the indenter velocity is approaching zero.

Pictures of the fracture zones for test specimen DynB1 and DynB2 are included in Figure 5-12. The crack appears to have propagated similarly in both tests (although mirrored). The observations and comments made regarding the fracture zone and fracture planes for the quasi-static tests are also valid for the dynamic tests. In the pictures one may also observe the deformations that occurred when the bolts in the flange impacted the plate.

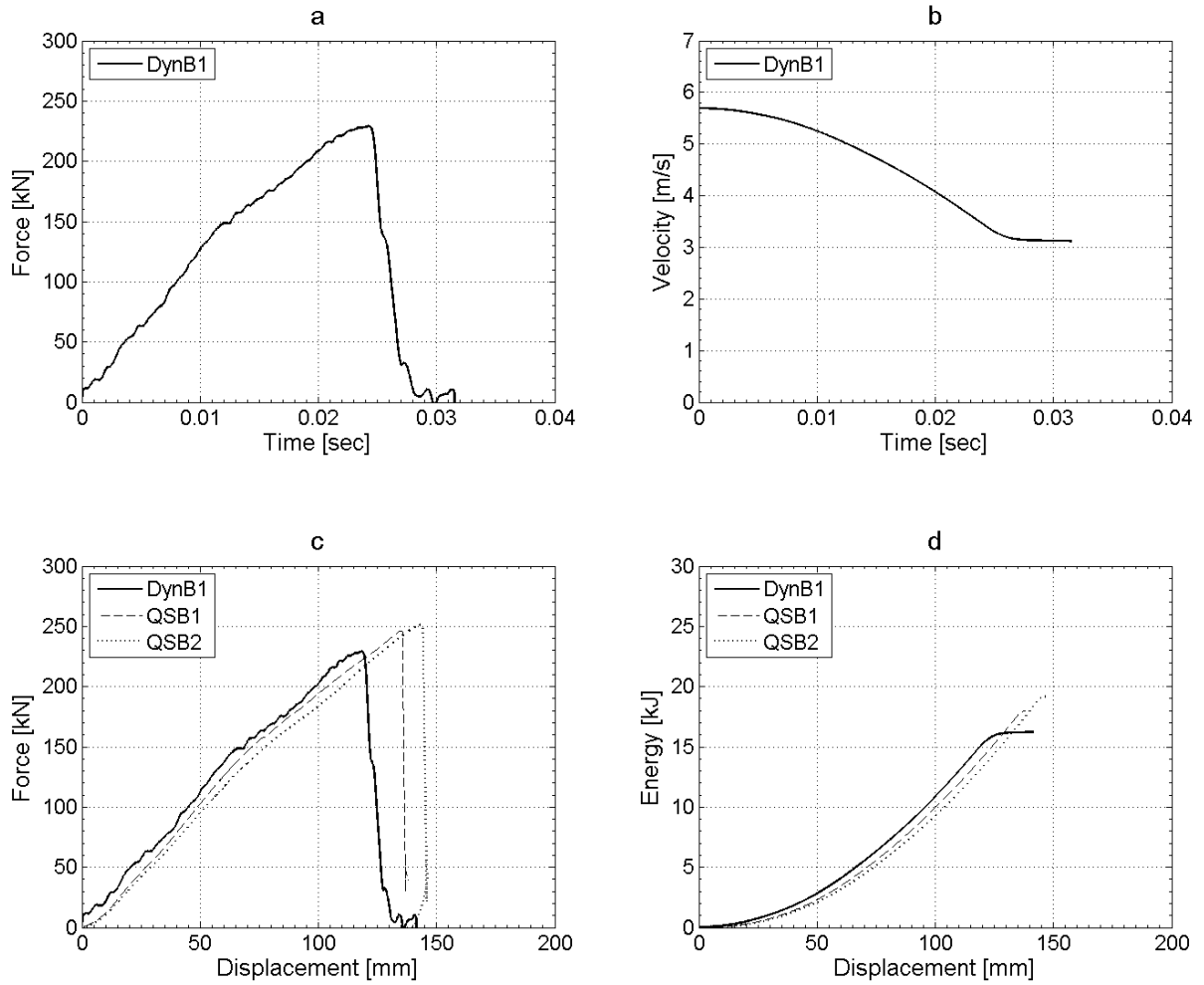
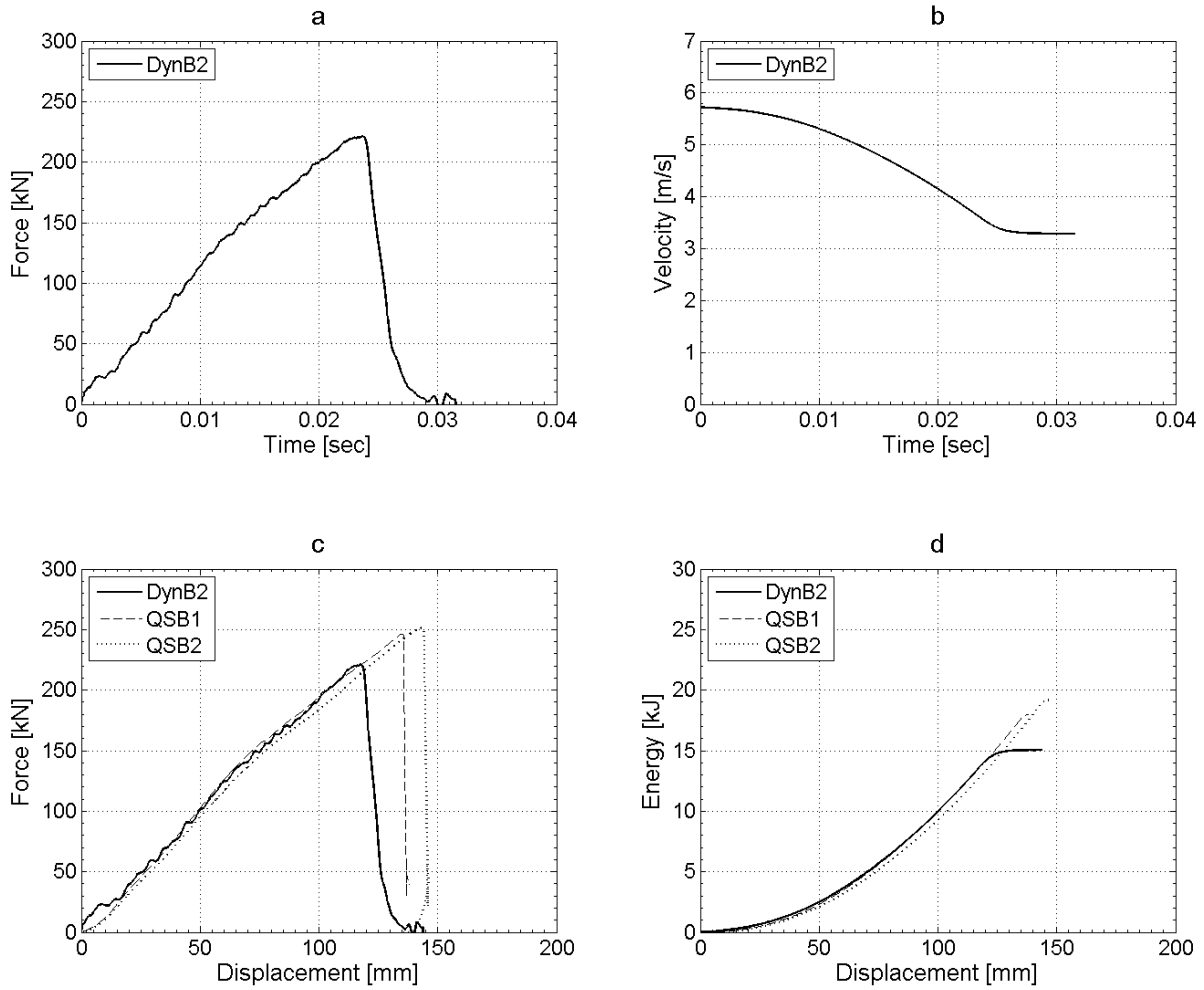


Figure 5-8: Results from test No. DynB1,  $M=1429\text{kg}$ ,  $v_0=5.70\text{m/s}$



**Figure 5-9: Results from test No. DynB2,  $M=1429\text{kg}$ ,  $v_0=5.72\text{m/s}$**

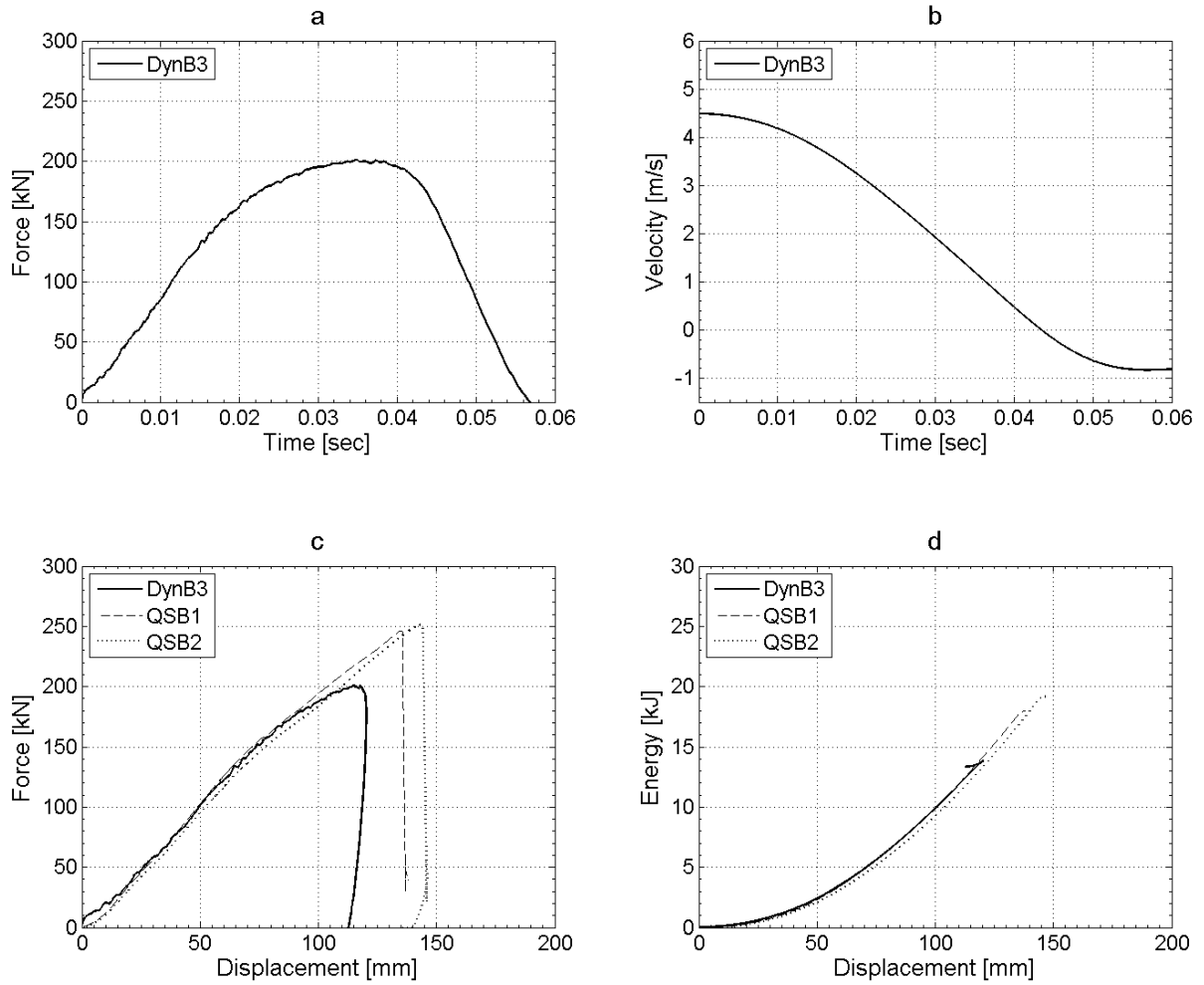
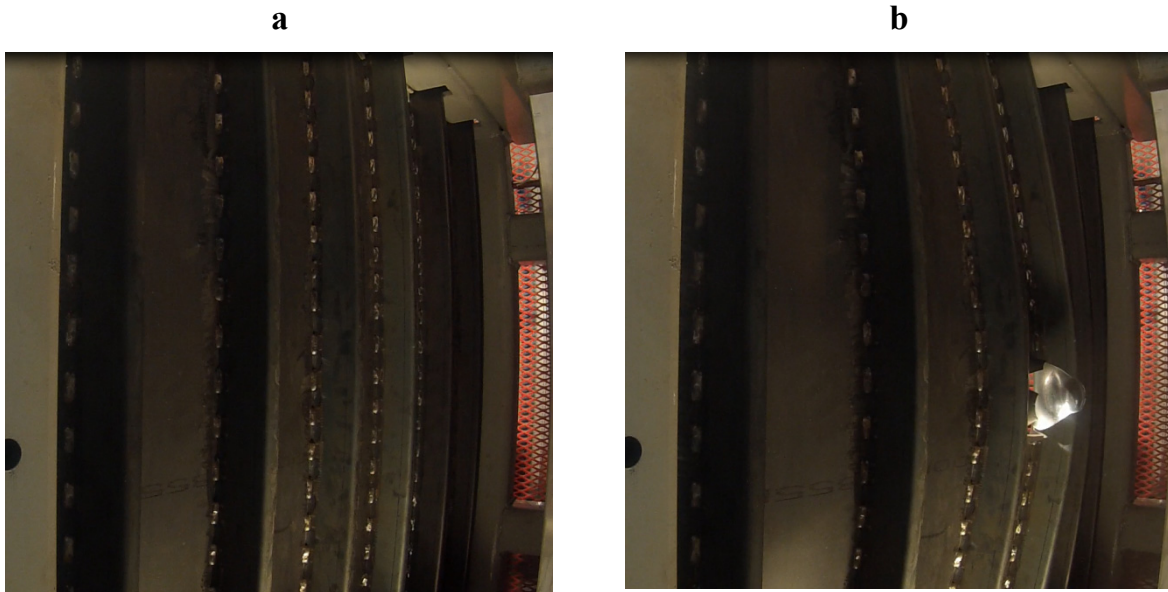
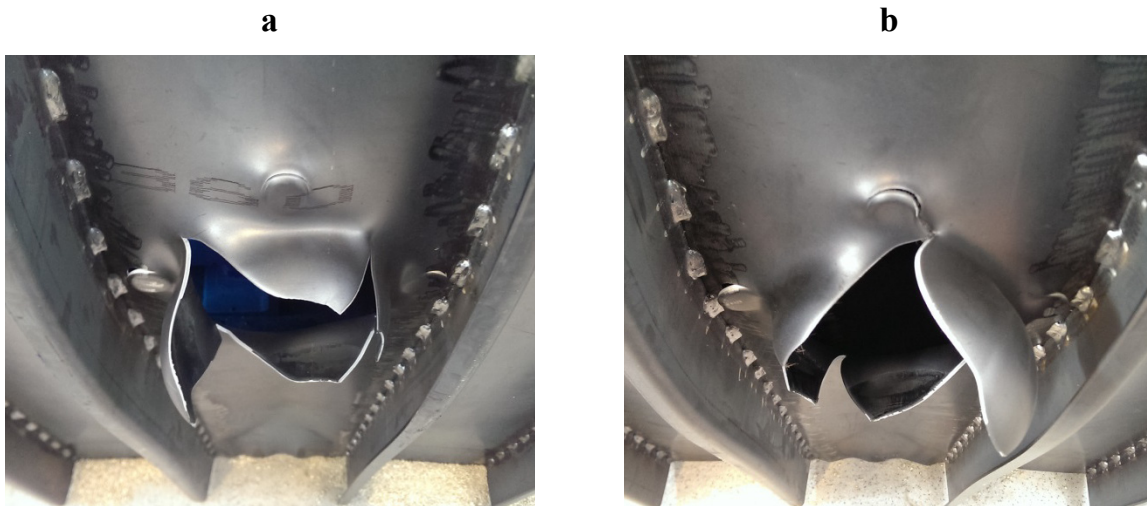


Figure 5-10: Results from test No. DynB3,  $M=1429\text{kg}$ ,  $v_0=4.49\text{m/s}$



**Figure 5-11: Pictures of test specimen DynB1. (a) Prior to impact. (c) After impact.**



**Figure 5-12: Pictures of test specimen fracture zone: (a) DynB1. (b) DynB2.**

#### 5.2.4 Test data accuracy

In Figure 5-13 the velocity and displacement histories for test DynA1 obtained based on measurements from the load cell are compared against those obtained from camera recordings. As seen a very good agreement between the two measurements are found. This indicates that the recorded test data for this test is accurate. For the three tests test involving indenter B, (DynB1, DynB2, DynB3), the corresponding agreement between measurements obtained from the load cell and those obtained from the camera recordings is not as good. The reason for this deviation is unknown, and it is not possible to determine which measurement is the most correct one. However, it can be shown that a better agreement between the two measurements may be obtained by adjusting the force by introducing an adjustment factor  $\gamma_a$ .

This leads to the following expression for the impact force:

$$F(t) = P(t) \cdot \gamma_{\text{force}} \cdot \gamma_a \quad (5-1)$$

Adjusting the force implies a change of the acceleration, velocity and displacement history. It is found that by using  $\gamma_a=1.1$ , a good fit of the velocity and displacement histories between the two different measurements from the three tests are found. Figure 5-14, Figure 5-15 and Figure 5-16 shows the comparison of the data obtained from the load cell and from the camera recordings for test DynB1, DynB2 and DynB3 respectively. The velocity and displacement curves based on original data from the load cell and the camera recordings are in the figures on the left hand side. The figures on the right hand side show the comparisons of the curves based on the adjusted data from the load cell with the data from the camera recordings. As may be observed the data correlates well after introducing the adjustment factor of 1.1, especially for test DynB3. For consistency the adjustment factor of 1.1 was used for all three adjusted data sets.

To illustrate how such an adjustment affects the results, force-displacement and energy-displacement curves for test DynB3 are shown in Figure 5-17. As seen, the response is stiffer and the maximum force increases (10%) when using the adjusted data. The peak energy, which equals the initial kinetic energy, still remains unchanged for this test. However, it should be noted that this adjustment will also increase the magnitude of the fracture energy for tests DynB1 and DynB2. This is illustrated in the velocity-time curves by a reduced constant velocity after full penetration of the plates (0.028sec and onwards). The increase is checked to be less than 7%.

To assure that the test data used in the validation phase does not overestimate the capacities of the stiffened steel plates, and considering that the reason for the deviation is unknown, it is decided to use the original measurements from the load cell in the validation phase in the present study. However, test results in terms of force-time curves, velocity-time curves, force-displacement and energy-displacement curves based on adjusted test data for the relevant tests (DynB1, DynB2, DynB3) are given in Appendix B.

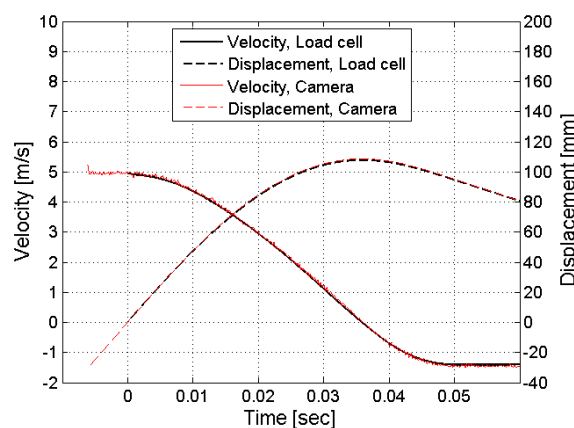


**Figure 5-13: Comparison of data obtained from load cell and from camera recordings for test DynA1.**

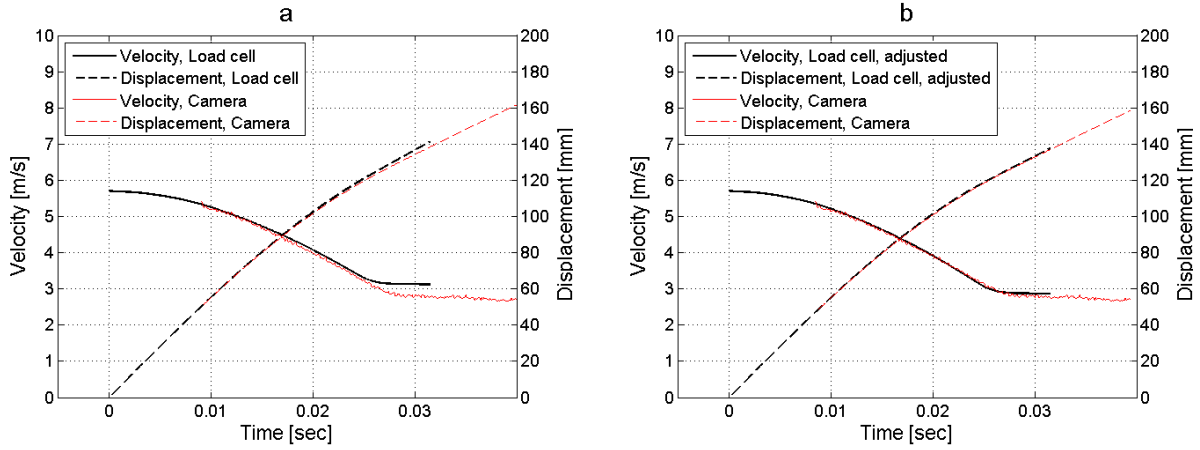


**Figure 5-14: Comparison of data obtained from load cell and from camera recordings for test DynB1. (a) Original data. (b) Adjusted data.**

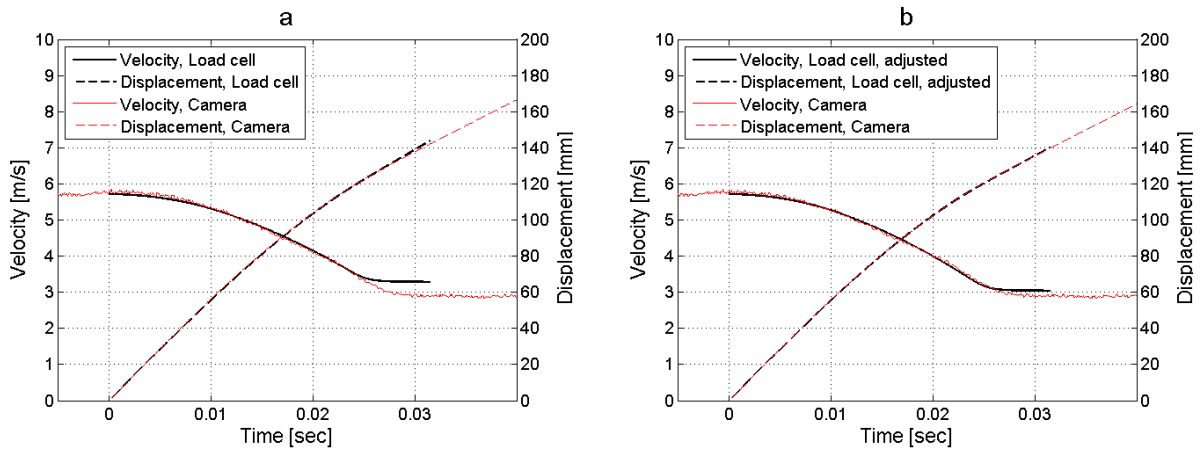


**Figure 5-15: Comparison of data obtained from load cell and from camera recordings for test DynB2. (a) Original data. (b) Adjusted data.**

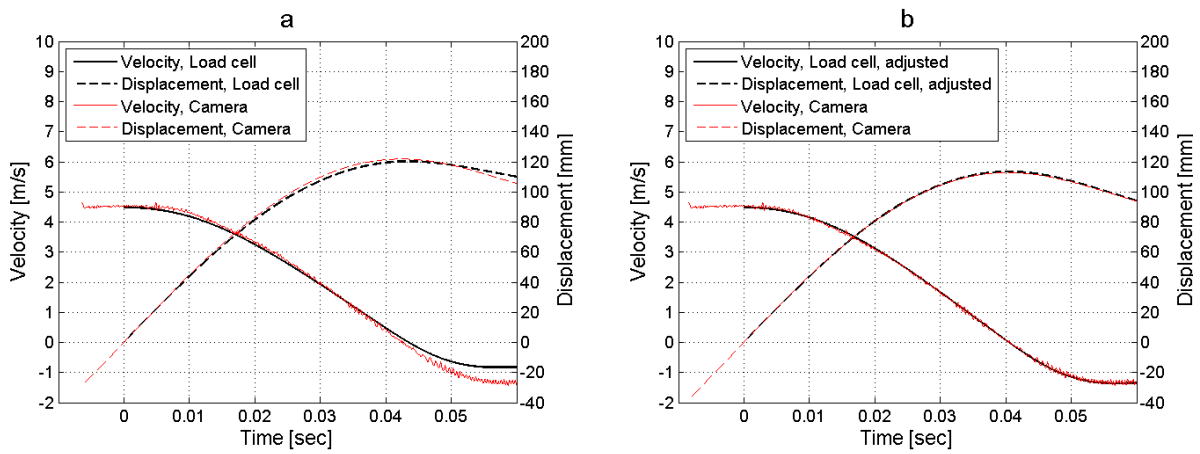


**Figure 5-16: Comparison of data obtained from load cell and from camera recordings for test DynB3. (a) Original data. (b) Adjusted data.**



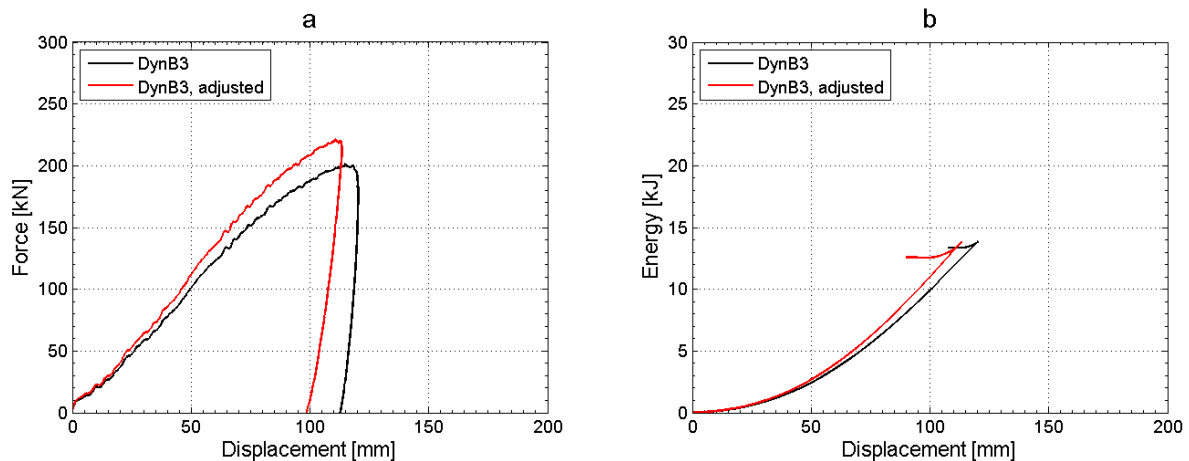


**Figure 5-17: Comparison of results obtained using original and adjusted data for test DynB3.**

### 5.3 Scale effects

In the present work the tests were carried out in scale 1:4. When introducing scaling, strain rate effects may arise which influence the scalability of the response when using classical replica scale modeling laws. No similitude analysis has been carried out in the present study to ensure that the response data obtained from these tests can be scaled.

In the experimentally study of the plugging capacity of steel plates performed by Langseth [14], a dimensional analysis according to the classical Buckingham Pi Theorem for a plated structure subjected to a dropped drill-collar is carried out and a literature review regarding the validity of the model law established is reported. As in the present study, the tests were conducted in scale 1:4. Good results are obtained in verifications of the model law, and based on the literature review reported it is indicated that a ductile dynamic response follows the replica scale modelling law when moderate scaling is used. The exception is in cases where tearing, cutting or ductile-brittle transitions occur during a structural response. Although it is a good indication, it is not a verification of that the test results obtained in the present study can be scaled using classical replica scale modeling laws.



## 6 ANALYSIS - VALIDATION BASED ON TESTS

### 6.1 General

In this part, validations based on the tests are reported. Comparisons between numerical and experimental results will be made, mainly by comparing force-displacement curves but also by inspecting deformations. Both the CL fracture criterion and the BWH instability criterion will be utilized in the numerical simulations in order to predict the capacity of the stiffened steel plates subjected to a concentrated load. In addition, the characteristic resistance of the stiffened steel plate is determined according to DNV-RP-C208 [28]. This is a document intended to give guidelines on how to establish the structural resistance for cases not covered by codes and standards by use of non-linear FE methods. The two first approaches used to determine the capacity are research approaches, while the latter is an industry approach. Towards the end of this chapter, the resistance according to the three approaches will be compared against each other.

In the quasi-static load situation, the capacity is predicted for load conditions involving both indenter A and B. Even if fracture did not occur in the test involving indenter A, it is still interesting to see what the capacity would be according to the above mentioned approaches. In the dynamic load situation, only the capacity for a load condition involving indenter B is investigated. However, the dynamic tests using indenter A will be simulated in section 6.5 when discussing the effects of including strain rate sensitivity in the simulations.

### 6.2 Computer model

The basic computer model with deformable frame (BM2) as described in section 4.5.3 is utilized as this produces the most realistic results as demonstrated in the preliminary analysis. The constraints that are enforced on the shim plates are removed and the parts are instead covered by the general contact formulation with a friction coefficient of 0.3 in the tangential direction. The shim plates are initially not in contact with the remaining part of the model. To avoid a situation where the parts are set into motion by propagating stress waves in the initial phase of the simulation, small stabilizing forces (0.01kN) is added, pushing the shim plates horizontally towards the frame.

As demonstrated in the parametric study performed on friction coefficients in the preliminary phase, the friction coefficient in the contact regions between the Teflon sheets and the plate has a great influence on the overall stiffness, hence also the force-displacement curves. Considering the effort spent in modeling the stiffness of the frame, it is also reasonable to use a more realistic friction coefficient than the idealized value of zero as initially assumed. Therefore the previously proposed low estimate friction coefficient of 0.04 is adopted. Nevertheless, it is worth mentioning that using a different friction factor may produce better results when comparing force-displacement curves with those obtained from the experiment. However, considering all other sources that influence the results such as, material properties, fabrication tolerances, frame stiffness modeling etc., calibrating the results to this particular friction coefficient alone does not add any value to the study.

In the quasi-static simulations it was desirable to study the effect of including strain rate sensitivity in the material definition. Consequently simulations using both the elastic-plastic and elastic-viscoplastic material models, MAT1a and MAT1b (refer to Table 3-3) are performed. To allow for a rate sensitive material model, mass scaling is used instead of time scaling so that the actual displacement rate of 10mm/min may be specified in the analysis. For consistency mass scaling was used in all quasi-static simulations. As may be observed from Equation (2-2) and (2-3), increasing the density will increase the critical time step in an explicit method, thus allowing the analysis time period to be extended without increasing the computational time. The size of the critical time step used is between 0.003sec and 0.08sec, depending on the mesh density. Similarly as in the preliminary simulations using time scaling, it is checked that the dynamic effects due to the mass scaling is small and negligible.

As for the quasi-static simulations, both MAT1a and MAT1b are utilized in the dynamic simulations. The indenter impact energy will be based on the actual energy used in the tests, and will be specified in each separate analysis.

For all validation approaches, at least one simulation using a very dense mesh in the plate field is performed. This simulation is considered as a reference, and will be used when comparing results between the different approaches. Mesh size 3mm is specified in the center region that experience the highest strains, and mesh size 6mm is used otherwise in the plate field. For convenience, this mesh configuration will only be referred to as mesh size 3mm. In the transition zone between the two mesh sizes, some elements are degraded to S3R in order to simplify mesh generation. S3R is the 3-node triangular version of S4R and has the required attributes, i.e. it is a general purpose element for thick and thin shells using finite membrane strains, and is thus suitable for the current analyses. A top view of the model with a refined mesh in the center region is shown in Figure 6-1, while a close up view is shown in Figure 6-2.

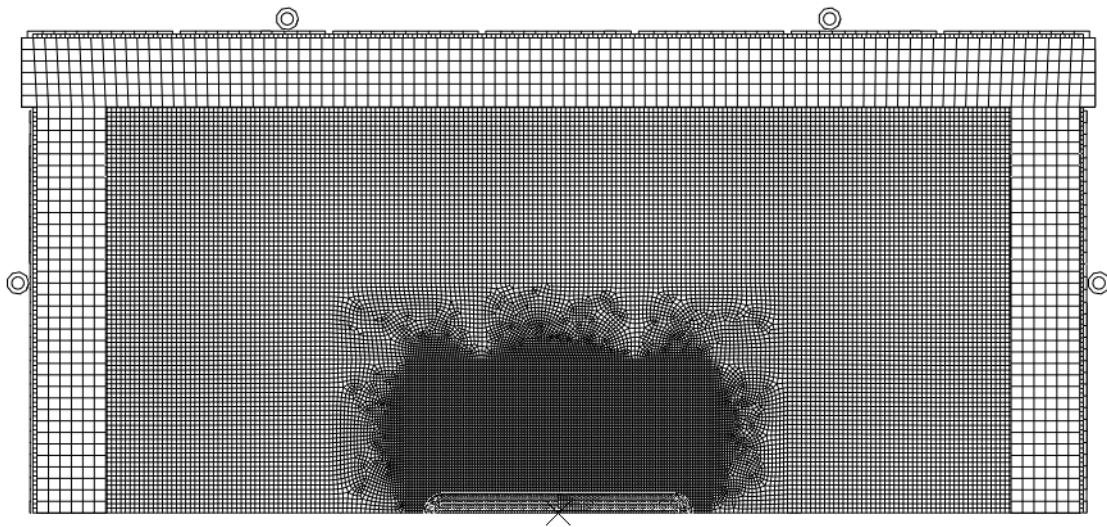


**Figure 6-1: Model with refined mesh in center region - Top view.**

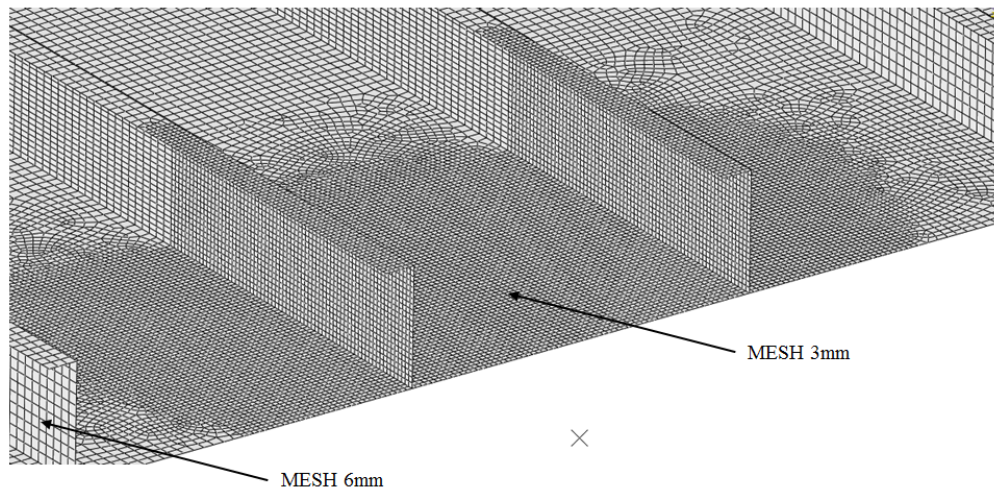


Figure 6-2: Model with refined mesh in center region - Close up view.

## 6.3 Simulations of the quasi-static tests

### 6.3.1 Validation using CL fracture criterion

#### Description

The critical energy measure per unit volume,  $W_{cr}$ , in the CL criterion is taken as 1109MPa as calculated in section 3.2.3. Each thickness integration point of the element is treated separately and once  $W_{cr}$  is reached, the integration point will be deactivated. With this approach, there will be a gradual reduction of the element stiffness. Once  $W_{cr}$  is reached in all five thickness integration points, the element is removed from the mesh.

The simulation using indenter A is only performed with the rate independent material model, while for indenter B both rate independent and rate dependent material models are used. Mesh size 3mm is used in these simulations. In addition, a simulation with mesh size 12mm is performed using indenter B to demonstrate how the combination of the CL criterion as it is implemented and a coarse mesh will considerably overestimate the capacity.

#### Load from indenter A - Results

Figure 6-3 shows the force-displacement curve from the analysis compared against test QSA1. In general, a good agreement is found between the two curves. At a displacement of approximately 125mm, the test starts to display a slightly stiffer behaviour. As previously described, the plate starts to buckle and deform at the supports as shown in Figure 5-2. This behaviour is difficult to model exactly; hence an increased difference in the numerical and experimental results as the deformation develops is expected. Fracture occurs in the simulation for a load level of 488kN with corresponding displacement of 217mm. This location is indicated with a circle on the curve. The plate indentation was stopped prior to fracture in the experiment; hence a comparison of the fracture load cannot be made.

In Figure 6-4 the distribution of the equivalent plastic strains just prior to fracture is shown. The maximum equivalent plastic strain extracted from the elements integration points is 1.37. The location is indicated in the figure. From Figure 6-5 it is seen that critical damage is

reached at the bottom integration point of three elements in the visible part of the model at a displacement of 213mm (plotted values are distance from fracture). The elements bottom side is the side facing away from the indenter. However, the critical damage is not yet reached in all integration points, thus the element is still active and it contributes to the stiffness. Shortly after, at 217mm, the three elements have failed. An interesting observation is that even at a displacement of 253mm, no additional elements have failed. Despite this the force continues to drop. By inspecting the deformed model in the analyses it is noted that the plate is close to sliding off the supports at the moment of fracture. A reduced stiffness at the supports due to reduced contact area is probably the major reason for the drop in the force observed.

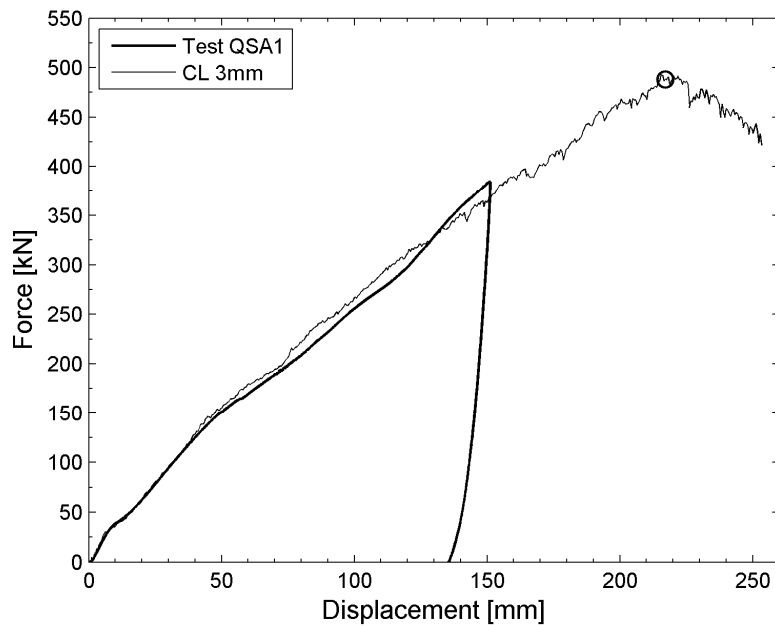


Figure 6-3: Quasi-static simulation with indenter A - Validation using CL criterion.

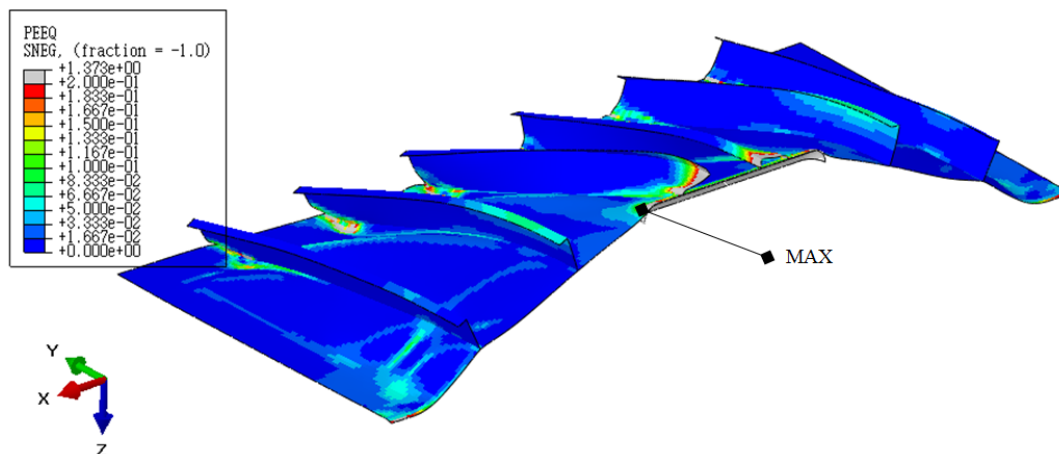
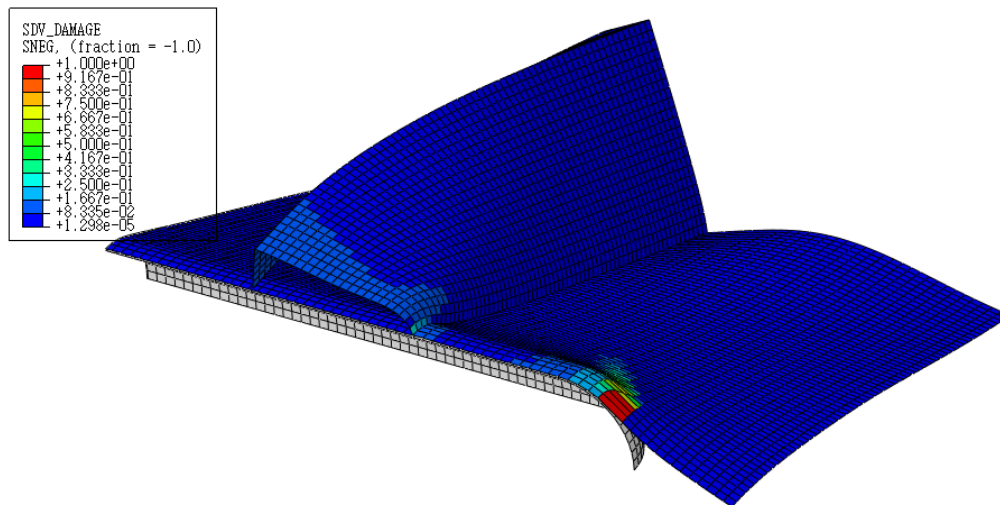


Figure 6-4: Quasi-static simulation with indenter A, CL 3mm – Equivalent plastic strain in plate field extracted from elements bottom integration point at 213mm indentation.



**Figure 6-5: Quasi-static simulation with indenter A, CL 3mm - Accumulated damage in critical region at 213mm indentation (1.0 indicate that the criterion is reached).**

#### Load from indenter B - Results

Figure 6-6 shows the force-displacement curves from the analysis compared against test QSB1 and QSB2. The agreement between the numerical and experimental results is excellent up to the point of fracture for the simulations with a dense mesh. Further the effect of including rate sensitivity in the material model is hardly noticeable. Only around the peak force, where the strain rates are at maximum, a slight increase in the load is observed due to rate sensitivity. In the simulations, fracture is reached for a load level of 251kN and 254kN for the rate independent and rate dependent material respectively. The corresponding displacement is approximately 141mm for both runs. It is also seen how the simulation with a coarse mesh will overestimate the capacity if the CL criterion is implemented in the same manner. The force-displacement curve for this run was omitted to better illustrate the other two simulations.

In Figure 6-7 the distribution of the equivalent plastic strains just prior to fracture is shown. The maximum equivalent plastic strain extracted from the elements integration points is 1.38. From Figure 6-8 it is seen that the critical damage is reached, at the bottom integration point for a few elements on both sides of the geometrical center. In the tests fracture first occurs towards one of the sides towards a stinger, see Figure 5-4. In the simulations initial fracture also occurs towards one of the sides. However, fracture on two other locations occurs directly after, as seen in Figure 6-9a. Both the simulations and the test develops a circular crack which leads to a significant drop in the load bearing capacity of the plate, see Figure 5-4b and Figure 6-9b. However, the material behaviour in the simulation is perhaps a little too ductile as the crack propagation does not develop as rapidly as observed in the tests.

In the simulations the computer model is mathematically perfect, i.e. no material or geometric imperfections are introduced. In the tests it is likely that some offset between the indenter and the plate center was introduced, which might have contributed to trigger fracture only towards one of the sides.

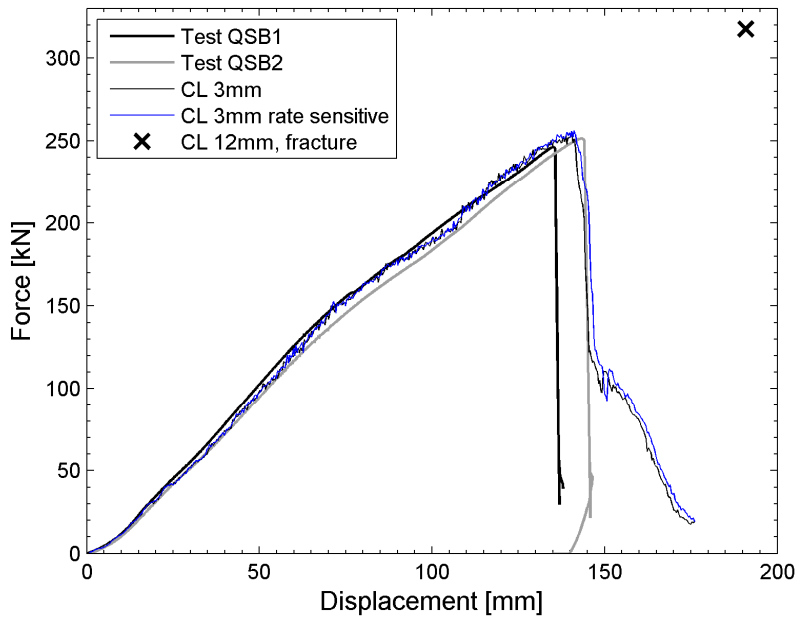


**Figure 6-6: Quasi-static simulation with indenter B - Validation using CL criterion.**

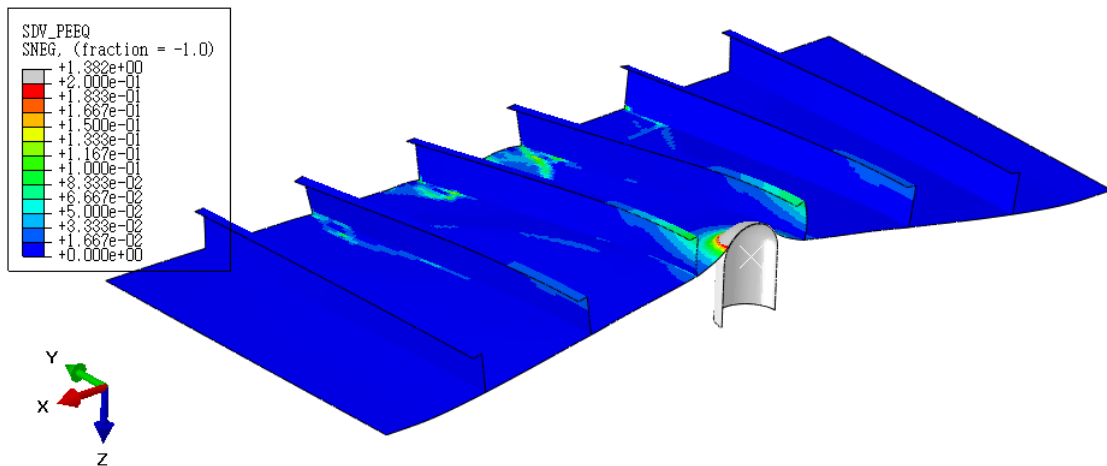


**Figure 6-7: Quasi-static simulation with indenter B, CL 3mm - Equivalent plastic strain in plate field extracted from elements bottom integration point at 140mm indentation.**



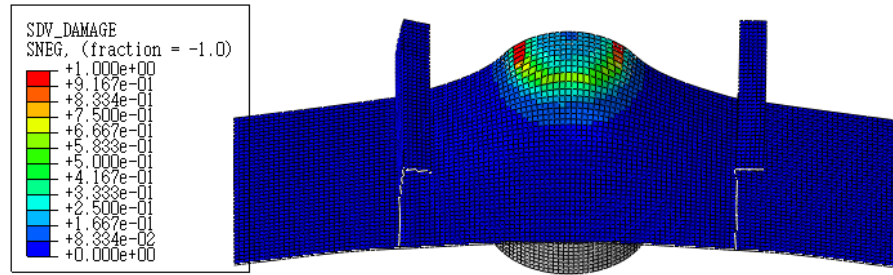


Figure 6-8: Quasi-static simulation with indenter B, CL 3mm - Accumulated damage at 140mm indentation extracted from the elements bottom integration point.

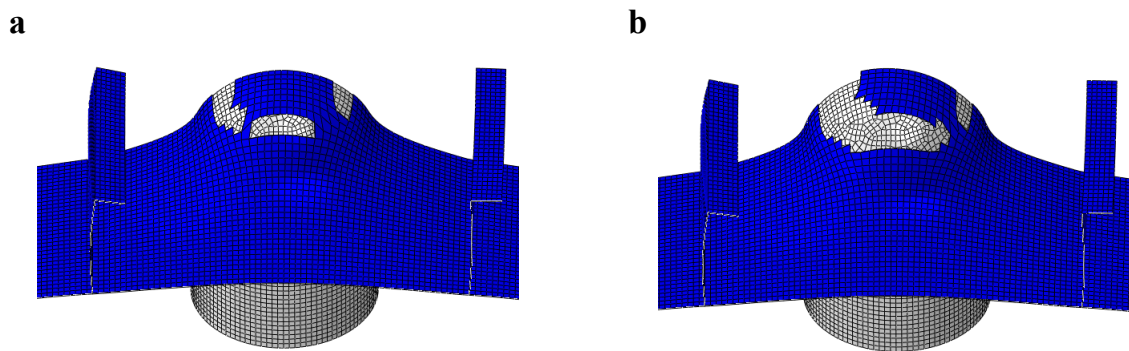


Figure 6-9: Quasi-static simulation with indenter B, CL 3mm: (a) Crack at 145mm indentation. (b) Crack at 152mm displacement.

### 6.3.2 Validation using BWH instability criterion

#### Description

The numerical simulations reported in this section are carried out using three different characteristic element sizes,  $l_e = [30, 12, 3]$  mm for indenter A, and four element sizes for indenter B,  $l_e = [30, 18, 12, 3]$  mm. Further is the elastic-plastic material model MAT1a used in all simulations. The BWH criterion is reached when the major principal stress averaged through the thickness of an element reaches the critical value as defined by Equation (2-44). With this approach bending effects are ignored which is reasonable considering the BWH criterion searches for local instability and thus applies to membrane stresses and strains only. As the criterion is reached, the element is removed from the mesh. The stress based forming limit diagram according to the BWH instability criterion was presented in section 3.2.4.

The effect of geometric scaling according to Equation (2-45) is investigated by scaling the critical stress for the entire plate field for a few simulations which has element size larger than the plate thickness. The approach of applying geometric scaling to the entire plate field will be a conservative approach as the real intention of the geometric scaling as proposed by Alsos et al. [8], is that it should only be used for the locations where strain concentrations most likely will appear, e.g. at plate stringer intersection or the location of a concentrated load. If geometric scaling is used in a particular simulation it will be indicated.

### Load from indenter A - Results

Figure 6-10 shows the force-displacement curves from simulations against test QSA1. The circle on the curves indicates the first occurrence of instability according to the BWH criterion. A simulation with element size 30mm without scaling was also performed but did not predict fracture for the applied displacement. This simulation is excluded from the figure to better illustrate the other simulations.

Figure 6-11 and Figure 6-12 illustrates the failed elements at 150mm indentation for the simulation using element size 3mm and the simulation using element size 12mm in combination with geometric scaling. For the simulation using element size 3mm in the center region, the BWH criterion is first triggered in the plate directly below the indenter, similarly as observed for the simulations using the CL criterion. However, the BWH criterion is triggered much earlier. For the simulation with element size 12mm and geometric scaling, instability is first initiated in the stringer flange followed by a part of the web. This is clearly a result of geometric scaling as this does not occur for the corresponding simulation without scaling. The stress distribution in the stringer is obtained quite accurately using a relatively coarse mesh. Applying geometric scaling to this area will thus initiate the BWH criterion prematurely. Also for the simulation using element size 30mm and scaling, instability is first triggered in the stringer.

From approximately 150mm indentation there is a relatively large scatter in the force-displacement curves. For the simulations with a coarse mesh, i.e.  $l_e = [30, 12]$  mm, the crack seems to propagate in arbitrary directions. The consequence is a rapid drop in the resistance. Figure 6-13 shows how the crack has evolved at 200mm indentation for the simulation using element size 3mm and the simulation with element size 12mm and geometric scaling. For the simulation with element size 3mm, the crack has propagated almost in a straight line so that membrane stresses can still be carried in the direction transverse to the indenter. For element size 12mm with geometric scaling, there is almost a total loss in resistance. Similar crack propagations are observed for the other simulations with a coarse mesh, only at different levels of indentation.

By inspecting the major and minor principal strains (plots not included) it is seen that the region where instability occurs in the plate directly below the indenter is in a tension-tension strain state (biaxial stretching). The stringer is almost in a uniaxial stress state, which implies positive major principal strains in longitudinal direction and negative minor principal strains in the transverse direction. It follows that it is the Bressan-Williams shear criterion that is triggered in the plate below the indenter, while it is Hill's instability criterion that is triggered when instability occurs in the stringers, refer to Equation (2-44).

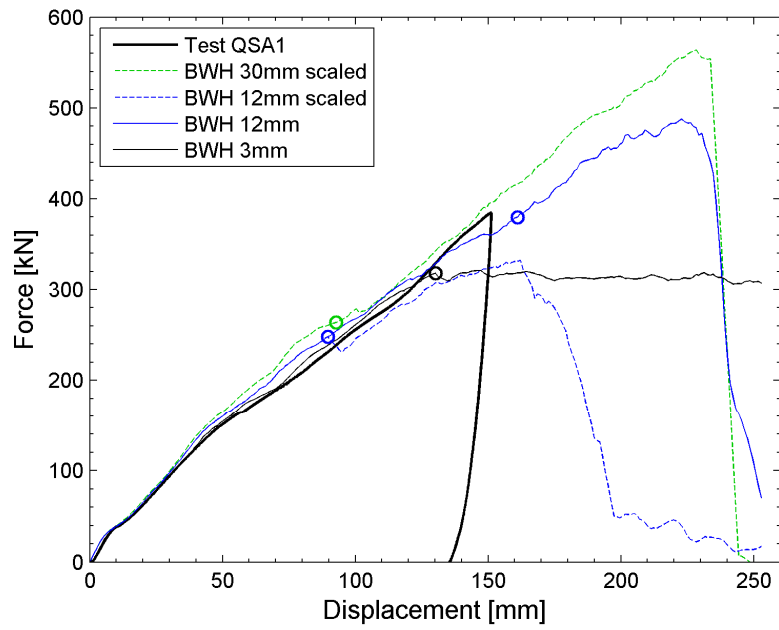


Figure 6-10: Quasi-static simulation with indenter A - Validation using BWH criterion.

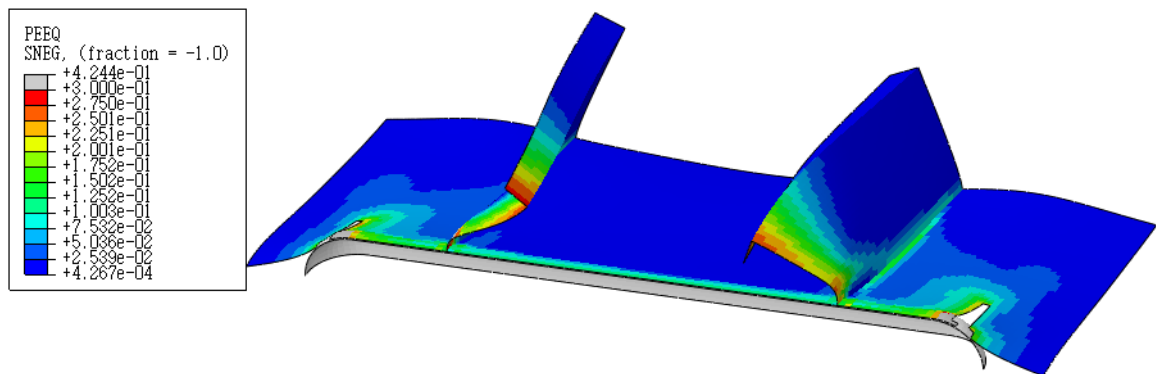
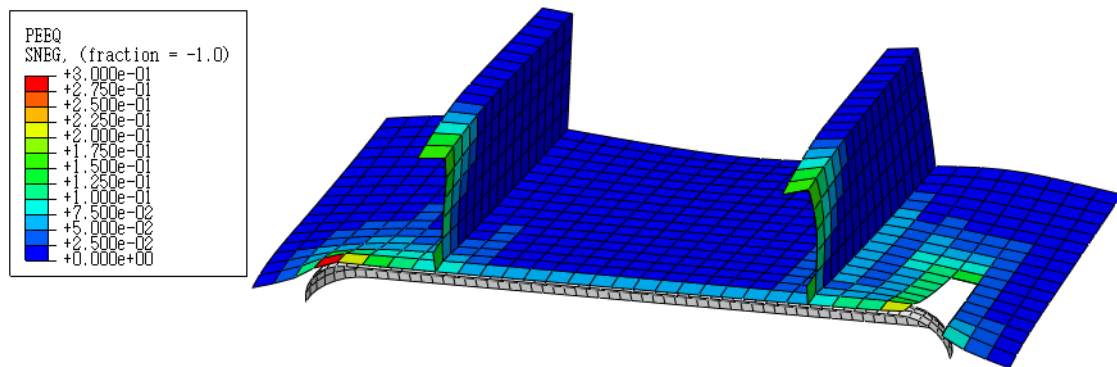
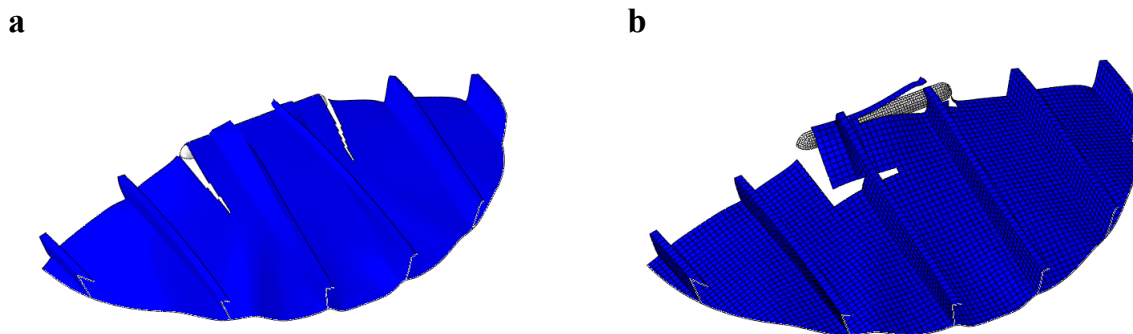


Figure 6-11: Quasi-static simulation with indenter A, BWH 3mm - Plastic equivalent strain at 150mm indentation extracted from the elements bottom integration point.



**Figure 6-12: Quasi-static simulation with indenter A, BWH 12mm scaled - Plastic equivalent strain at 150mm indentation extracted from the elements bottom integration point.**



**Figure 6-13: Quasi-static simulation with indenter A: (a) Crack at 200mm indentation for BWH 3mm. (b) Crack at 200mm indentation for BWH 12mm scaled.**

### Load from indenter B - Results

Figure 6-14 shows the force-displacement curves from the simulations compared against test QSB1 and QSB2. The BWH instability criterion is activated for a lower load level than the fracture load from the test for all simulations performed. The maximum load in the simulation with element size 3mm in the center region is 161kN, which is approximately 65% of the minimum fracture load from quasi-static tests. As this simulation should be able to represent the relevant stress concentrations, and since no geometric scaling is needed, this can be considered to be the “real” capacity according to the BWH instability criterion. From the curves it is seen how geometric scaling yields conservative results compared against the “real” capacity according to BWH instability criterion. Further it is seen that the simulations with element size 12mm and 30mm without geometric scaling overestimates the load at onset of instability relative to the one with a dense mesh. As an additional check, the simulation BWH 3mm were also run with zero friction between the indenter and the plate. This resulted in an insignificant increase of the fracture load, and is therefore not reported.

Figure 6-15 shows how the crack has propagated and the level of equivalent plastic strain at fracture for the simulation with a dense mesh. As soon the BWH criterion is reached in one element the crack propagates very rapidly which leads to a sudden drop in resistance,

similarly as observed in the tests. Several fracture lines occur and they seem to develop in straight lines, eventually allowing for full penetration of the indenter through the plate. As for the simulations with indenter A, the crack propagates differently when using larger element sizes. However, as full penetration of the plates occurs very rapidly for all cases, this has a negligible influence on the force-displacement curves.

From Figure 6-16 it is seen that the local plate field directly below the indenter is in a tension-tension strain state (biaxial stretching). It follows that it is the Bressan-Williams shear criterion that triggers incipient instability in the simulations, refer to Equation (2-44).

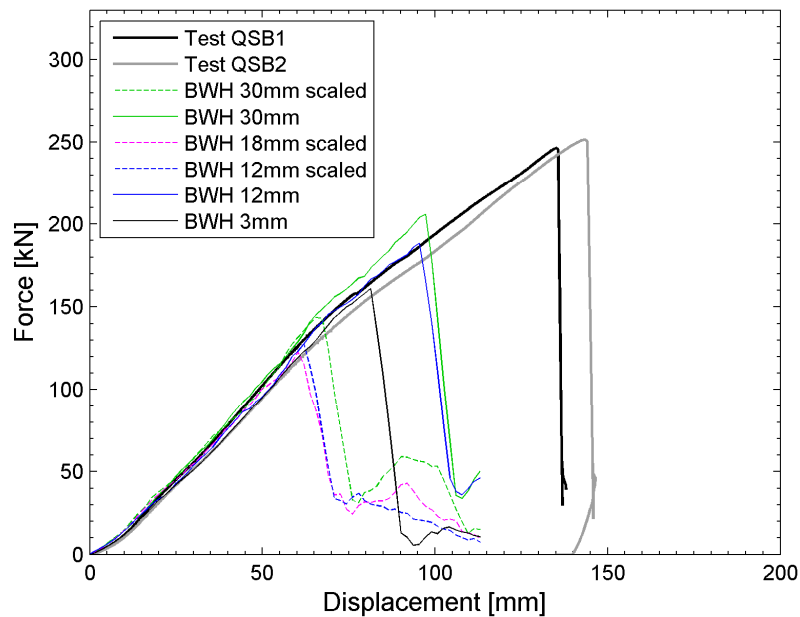


Figure 6-14: Quasi-static simulation with indenter B - Validation using BWH criterion.

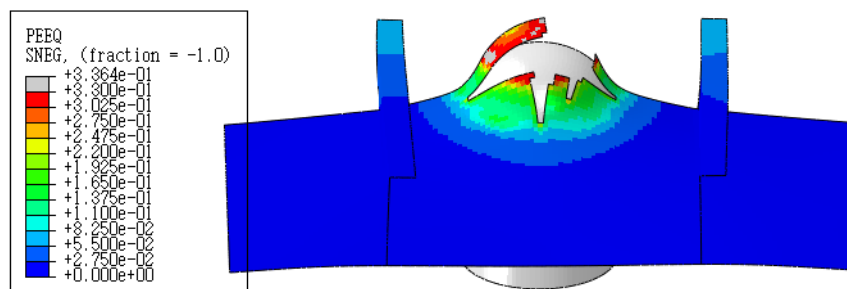
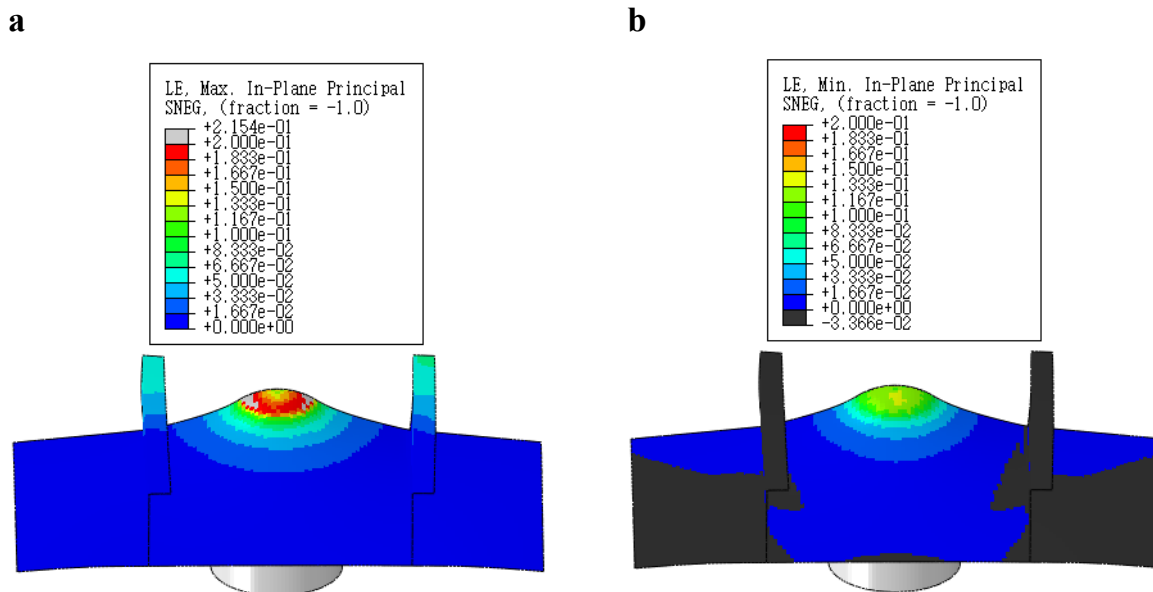


Figure 6-15: Quasi-static simulation with indenter B, BWH 3mm - Plastic equivalent strain at 88mm indentation extracted from the elements bottom integration point.



**Figure 6-16: Quasi-static simulation with indenter B, BWH 3mm: (a) and (b) shows the major and minor principal strain just prior to instability.**

### 6.3.3 Validation using DNV-RP-C208

#### Description

Similar to what is required by many other structural standards using the limit state safety format, the characteristic resistance as defined by DNV-RP-C208 should represent a value that meets the requirement that there is less than 5% probability that the resistance is less than this value. This typically involves using the specified minimum yield stress according to steel material standards. DNV-RP-C208 proposes an idealized bilinear true stress-strain curve based on the minimum yield stress. However, in order to perform a reasonable comparison when validating the capacity according to the DNV recommended practice against the tests, the material model MAT1a established in section 3.2 is utilized.

When designing against tensile failure DNV-RP-C208 proposes two main solutions. The first approach, which also will be the more accurate of the two, is to calibrate the non-linear FE analysis against a known solution. This means that a similar problem with a known capacity, either from a design code or a test, is selected as a reference object. The reference object is modeled and analyzed using the recommended methods and a failure strain parameter is determined. The capacity of the real structure is found by modeling and analyzing using the same technique as used for the reference object.

The above approach will have many limitations, e.g. in cases where problems similar as the one at hand are not covered by any code or test available. The second approach, which is the one that will be visited herein, is a simplified approach for plane plates. The simplified approach involves two checks for tensile failure:

1. Tensile failure due to gross yielding along a failure line
2. Tensile failure due to cracks starting from local strain concentrations

The plastic strain limit for tensile failure due to gross yielding along a failure line is 0.04, while the limit for local yield strain is 0.12 for S355 steel when using the simplified method.

The method allows for elements up to 5 times the plate thickness to be used. However, if a coarse mesh is used, a resistance knock down factor should be determined based on a convergence study. The analyses reported in this section is based on postprocessing of the results from the two quasi-static simulations referred to as “CL 3mm”, refer to section 6.3.1. I.e. simulations with mesh size 3mm and the elastic-plastic material model MAT1a.

### Load from indenter A - Results

The meaning of a failure line in this context would be that a structure loses most of its ability to carry the load if failure occurred along this line. For the stiffened steel plate geometry it could be difficult to identify what is a critical failure line. One approach would be to say that the bottom flange of the stringers is a critical line. However, this would be very conservative, as a large part of the load is carried by membrane forces in the plate, and not by the stringers. A more reasonable approach would be to state that the line directly below the indenter is a critical line. This line is indicated on Figure 6-17. A large part of the membrane stresses in the plate is carried in the direction perpendicular to this line (in y-direction). As a result the major principal stresses are more or less pointing in the same direction for all the elements along this line.

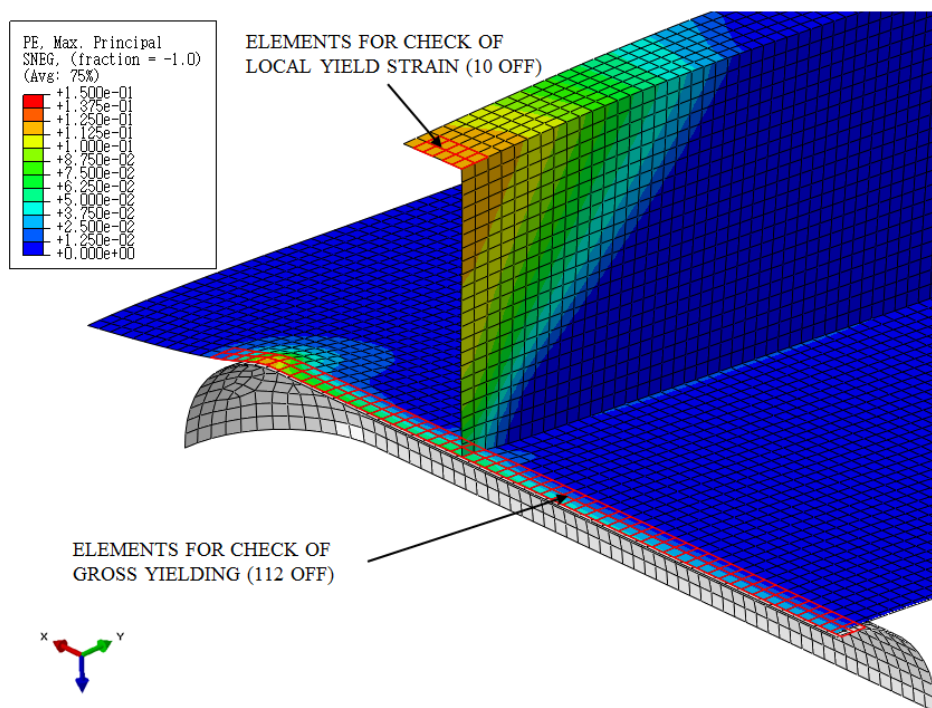


**Figure 6-17: Analysis with indenter A - Maximum principal plastic strain at bottom integration point, with chosen elements for data extraction indicated.**

DNV-RP-C208 suggests that for plane plates, the gross yielding along a failure line should be checked by averaging the strain in the direction of the maximum principal plastic strain and by linearization along the failure line and through the plate thickness. A linearization through a shell element thickness is similar as using the values obtained from the top or the bottom integration point, whatever is the maximum. The strain may be averaged over a length of up to 5 times the thickness of the plate, for pure membrane strains. Due to the line load, out-of-plane bending action also occurs along this failure line. However, the membrane action

dominates, and it is checked that both the top and bottom integration point of the shell element experience tension.

Considering the full geometry in this case, the strain is averaged over a length of 4 elements, which is within the limit as the element length equals the plate thickness. A linearization along the failure line will in this case be identical as the average strain over the failure line when considering the full geometry (if assuming symmetry in x-direction, refer to Figure 6-17). When calculating the average strain, the maximum principal plastic strain extracted from the elements bottom integration point is used. The elements bottom side is the side opposite to the indenter.

In addition to checking the critical line, the local yield strain limit should be fulfilled to ensure that no tensile failure occurs due to cracks starting from local strain concentrations. DNV-RP-C208 suggests that the local yielding can be checked by averaging the strain over a rectangular prismatic volume at the location with the largest strain. Further, this volume should be taken through the thickness of the plate and may extend up to 5 times the thickness in the other directions. The strain can be calculated as the average value in the direction of the maximum principal plastic strain and should be linearized in the other two directions. The corner with the largest plastic strain should be below the critical local yield strain.

The flange of one of the center stringers is identified as governing when checking for the local yield strain limit. The chosen volume for data extraction is 5x2x1 elements (5x4x1 elements when considering the full geometry) as shown in Figure 6-17, which is within the limit as the element length equals the plate thickness. When calculating the local gross yielding the maximum principal plastic strain is extracted from the elements bottom integration point and averaged over the volume. It is checked that the maximum principal strain is more or less in the same direction (y-direction) within the volume, and that the strain in the elements top integration point are less onerous.

The analysis results are shown in Table 6-1. It is seen that for a load level of 165kN, the gross strain along the failure line does not exceed the critical strain value of 0.04 and the local strain does not exceed the critical strain level of 0.12.

**Table 6-1: Quasi-static analysis results, indenter A - Gross and local yielding**

Load level [kN]	Gross maximum principal plastic strain	Local maximum principal plastic strain
165	0.0369	0.1191
176	0.0400	0.1280

#### Load from indenter B - Results

The load condition using the geometry of indenter B involves a point load. When a point load is involved, the plastic strains in the region of applied load will be high and the governing check is found to be tensile failure due to cracks starting from local strain concentrations.

The chosen volume for data extraction is 5x2x1 elements (5x4x1 elements when considering the full geometry), which is within the limit given in DNV-RP-C208 as the element length equals the plate thickness. Figure 6-18 shows the maximum principal plastic strain at the bottom of the shell in the region below the indenter with the chosen elements indicated. When calculating the local gross yielding the maximum principal plastic strain is extracted from the elements bottom integration point and averaged over the volume. It is checked that the



maximum principal strain is more or less in the same direction (x-direction) within the volume, and that the strain in the other in-plane direction is less onerous. The strain at the upper integration point is checked to be in tension, thus the bending strain criteria is not relevant.

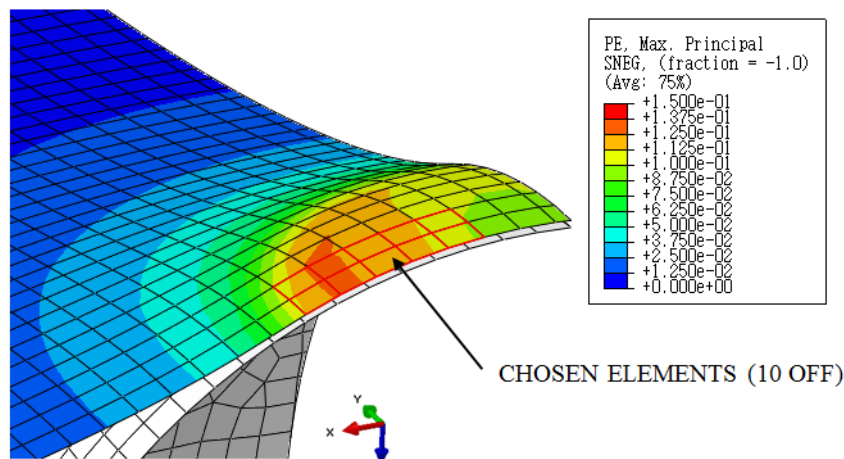


**Figure 6-18: Analysis using indenter B - Maximum principal plastic strain, with chosen elements for data extraction indicated.**

From Table 6-2 it is seen that for a load level of 101kN, the local strain does not exceed the critical strain value of 0.12. This is 41% of the minimum capacity of 246kN found from the quasi-static tests.

**Table 6-2: Quasi-static analysis results, indenter B - Local yielding.**

Load level [kN]	Local maximum principal plastic strain
101	0.1196
104	0.1217

## 6.4 Simulations of the dynamic tests

### 6.4.1 Validation using CL fracture criterion

#### Description

The dynamic tests found to be relevant for validation using the CL fracture criterion are test DynB1 and test DynB2. As reported in section 5.2.3 the measured impact velocities for these runs were 5.70m/s and 5.72m/s for test DynB1 and DynB2 respectively. Due to the similar impact velocities, the second test is considered to be a repetition of the first one. Both tests resulted in fracture of the stiffened steel plate.

In the numerical simulations reported in this part, an impact velocity of 5.70m/s is specified. The indenter mass is adjusted in the computer model to correspond to the measured trolley mass of 1429kg. The resulting impact energy is 23.2kJ, which is the same as in test DynB1. Both the rate independent and rate dependent material models are used and the computer model with a very dense mesh in the center region is used (3mm in the center region, and mesh size 6mm otherwise, as shown in Figure 6-2). These runs will be referred to as “CL

3mm”, and “CL 3mm rate dependent”. In addition the effect of increasing the friction coefficient between the indenter and the plate to 0.5 is investigated (the friction coefficient in the basic computer model is 0.3, refer to Table 4-1). This run is referred to as “CL 3mm  $\mu_3=0.5$ ”. The CL fracture criterion is implemented identically as for the quasi-static simulations reported in section 6.3.1.

#### Load from indenter B - Results

Figure 6-19 shows the force-displacement curves from the simulations compared against test DynB1 and DynB2. Both the simulations “CL 3mm” and “CL 3mm rate sensitive” overestimate the capacity compared to the tests. The force-displacement curve for run “CL 3mm” is very similar as the corresponding static one, which implies similar fracture energy. When accounting for rate sensitivity, the capacity further increases as seen in the figure. In this simulation fracture occurs at the maximum load. However, full penetration of the indenter into the plate is not achieved and a rebound occurs. As discussed when reporting the results from the dynamic tests, the stiffness and the maximum force from tests with indenter B is probably underestimated. Nevertheless, when accounting for this possible underestimation, the reduced fracture energy that was observed in the dynamic tests compared to the equivalent static tests is not accurately reproduced in the simulations. It is also noted that the force in the initial phase is higher in the tests compared to the simulations.

As fracture is occurring directly in the interface between the indenter and the plate, the contact conditions in this area affect the initiation of strain localization. As demonstrated in the preliminary simulations, specifying zero friction in this area reduced the capacity for the computer model with mesh size 12mm. Specifying zero friction in the simulations reported in this part, seem to further increase the capacity. However, as seen from the results of run “CL 3mm  $\mu_3=0.5$ ”, the capacity reduces when increasing the friction coefficient to 0.5 from the value of 0.3 that is used in this contact region in the other simulations. With an increased friction, the strain localization accelerates when using this mesh and the CL fracture criterion is reached at an earlier stage.

For all the dynamic simulations reported in this part, fracture first occurs in the same elements as in the corresponding quasi-static simulation. These elements are shown in Figure 6-8.

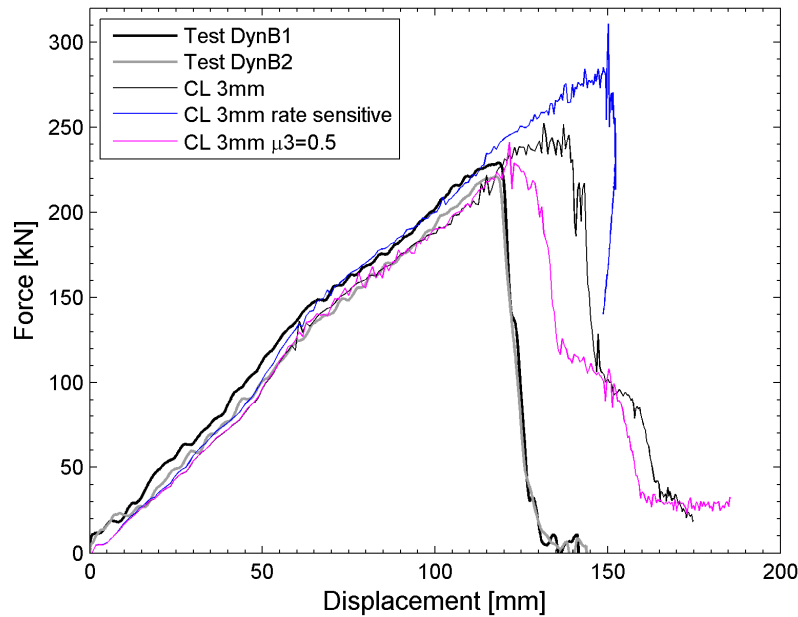


**Figure 6-19: Dynamic simulations with indenter B,  $M=1429\text{kg}$ ,  $v_0=5.70\text{m/s}$  - Validation using CL criterion.**

## 6.4.2 Validation using BWH instability criterion

### Description

As for the simulations performed with the CL criterion, the dynamic tests DynB1 and DynB2 are found to be relevant for validation using the BWH instability criterion. Similarly, the indenter is given an initial velocity of  $5.70\text{m/s}$  and the mass is adjusted to correspond to the trolley mass of  $1429\text{kg}$ , which give the resulting impact energy of  $23.2\text{kJ}$ . As demonstrated in the quasi-static simulations with indenter B, the characteristic element sizes  $30\text{mm}$  and  $18\text{mm}$  provided similar capacity as the simulations with element size  $12\text{mm}$ . Therefore, in the simulations reported in this section element size  $3\text{mm}$  and  $12\text{mm}$  will be utilized. The latter mesh is used with and without geometric scaling.

The BWH instability criterion is implemented identically as for the quasi-static simulations reported in section 6.3.2.

### Load from indenter B - Results

Figure 6-20 shows the force-displacement curves from the simulations compared against test DynB1 and DynB2. As for the quasi-static simulations, the BWH instability criterion is activated for a lower load level than the fracture load from the tests. If comparing the curves from all dynamic simulations with BWH criterion with the corresponding curves from the quasi-static condition shown in Figure 6-14, very little difference is observed. As the fracture energy from the dynamic tests was lower than the static ones, this implies that the BWH instability criterion will be less conservative in the dynamic condition than what was observed for the static condition.

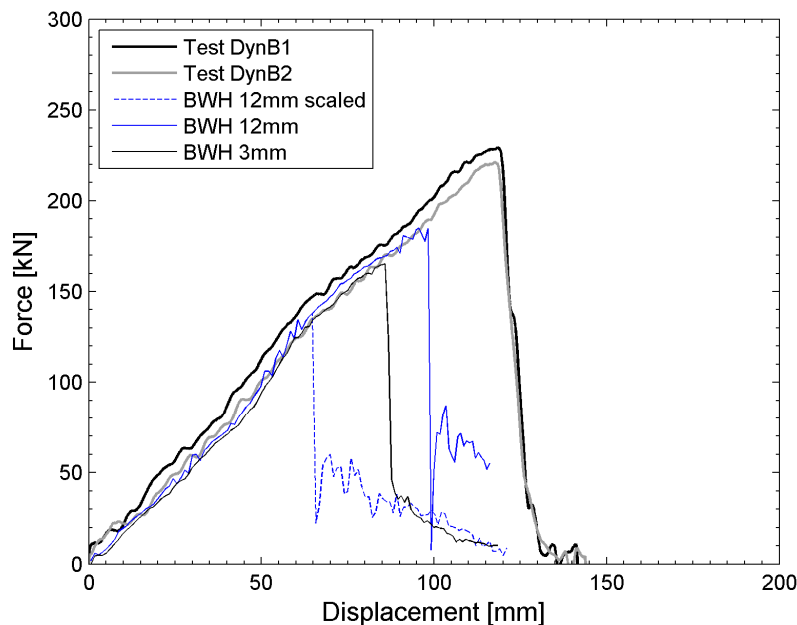


**Figure 6-20: Dynamic simulations with indenter B,  $M=1429\text{kg}$ ,  $v_0=5.70\text{m/s}$  - Validation using BWH criterion.**

### 6.4.3 Validation using DNV-RP-C208

#### Description

In this part the capacity of the stiffened steel plate subjected to a dynamic load from indenter B is determined according to DNV-RP-C208. The analysis presented is based on post-processing of the results from the dynamic simulation referred to as “CL 3mm”, refer to section 6.4.1. This is a dynamic simulation using a very dense mesh (3mm) in the center region of the plate field identically as shown in Figure 6-2 and with the elastic-plastic material model MAT1a. The impact velocity for this simulation is 5.70m/s, and the impact energy is 23.2kJ. Based on the analysis results obtained for the quasi-static condition presented in Table 6-2, there is no doubt that this will give significant higher impact energy than allowed according to the simplified method in DNV-RP-C208. However, as for the validation using the BWH criterion, the approach of using the same impact energy as in the test is chosen in order to simplify the comparison between the three different approaches used to predict tensile failure.

#### Load from indenter B - Results

By following the same procedure as for the quasi-static load condition described in section 6.3.3, the results shown in Table 6-3 are found. The local maximum principal strain is averaged over the exact same elements as shown in Figure 6-18 (found to be governing also in this load case). It is seen that for a load level of 106kN, the local maximum principal strain is below the limit of 0.12. It is mentioned in DNV-RP-C208 that increased strength and reduced ductility due to strain rate effects may be considered. Further a material model to account for strain rate effects is proposed. More details on this material model will be shown in section 6.5.1 when discussing the effect of including strain rate sensitivity in the analysis.

**Table 6-3: Dynamic analysis results, indenter B - Local yielding.**

Load level [kN]	Local maximum principal plastic strain
106	0.1192
110	0.1237

## 6.5 Discussion on results from numerical simulations

### 6.5.1 Strain rate sensitivity

The rate dependent material model used in the present study, MAT1b, was calibrated against tension tests performed at a low strain rate. It may be argued that this approach does not give reliable data on the rate parameters. DNV-RP-C208 proposes to use the Cowper-Symonds (CS) model to simulate strain rate effects. The CS model may be expressed as [28]:

$$\sigma_{dynamic} = \sigma_{static} \left( 1 + \left( \frac{\dot{p}}{C} \right)^{\frac{1}{p}} \right) \quad (6-1)$$

Further it is stated that the constants  $C$  and  $p$  should be based on experiments and calibrated for the expected maximum stress (strain). In lack of data,  $C=4000s^{-1}$  and  $p=5$  is proposed for common offshore steel materials. Figure 6-21 shows the difference between MAT1b and the Cowper-Symonds model with the constants proposed in DNV-RP-C208 for two selected strain rates. As may be observed, the latter model is more strain rate sensitive.

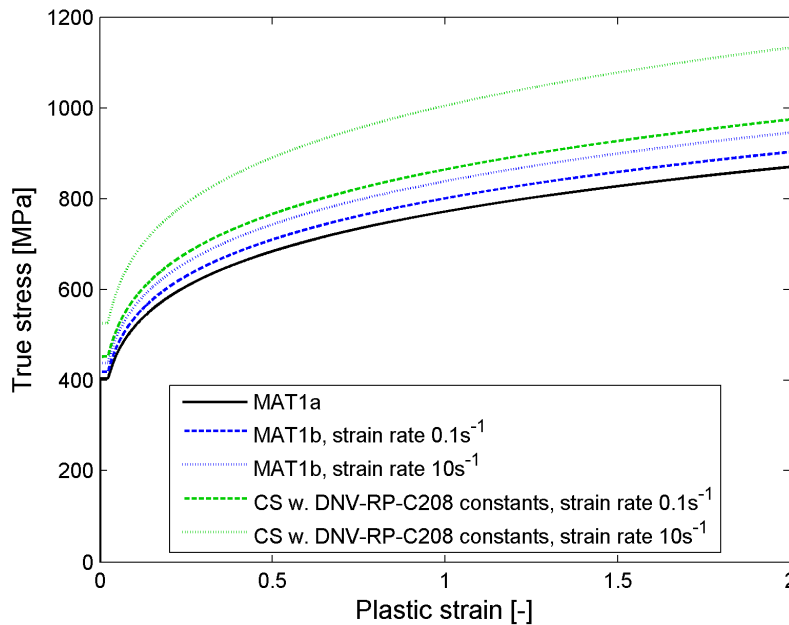


**Figure 6-21: Comparison of MAT1b and the CS model with proposed constants from DNV-RP-C208.**

As previously described the results from the tests using indenter B probably underestimates the stiffness of the structure. Therefore, it was not possible to check whether the strain rate

sensitivity parameters determined for material model MAT1b gave any accurate results regarding increased stiffness when simulating the dynamic tests DynB1 and DynB2. However, by simulating the dynamic test DynA1 using MAT1a and MAT1b, it will be possible to evaluate the approximate level of accuracy for the material model. A simulation using the CS material model with constants proposed in DNV-RP-C208 is also performed for comparison and to study the effects of increased rate sensitivity. The computer model with a very dense mesh in center region and indenter A is utilized. The impact velocity is taken as 4.95m/s as recorded in the test and the indenter mass is adjusted to correspond to the trolley mass of 1431kg.

The results from these simulations are shown in Figure 6-22. As may be seen, the test results are reproduced quite well. As expected, the run without accounting for strain rate sensitivity underestimates the stiffness slightly. The run with the CS model seems to overestimate the stiffness, indicating that the rate parameters proposed in DNV-RP-C208 is not accurate for this particular material. The run using MAT1b indicates that the established rate parameters appears to be quite appropriate, at least for the strain levels that are present in this test. However, one should not overstate the validity of the model based on this single comparison. The parameters are still established based on tensile tests performed at a low velocity.

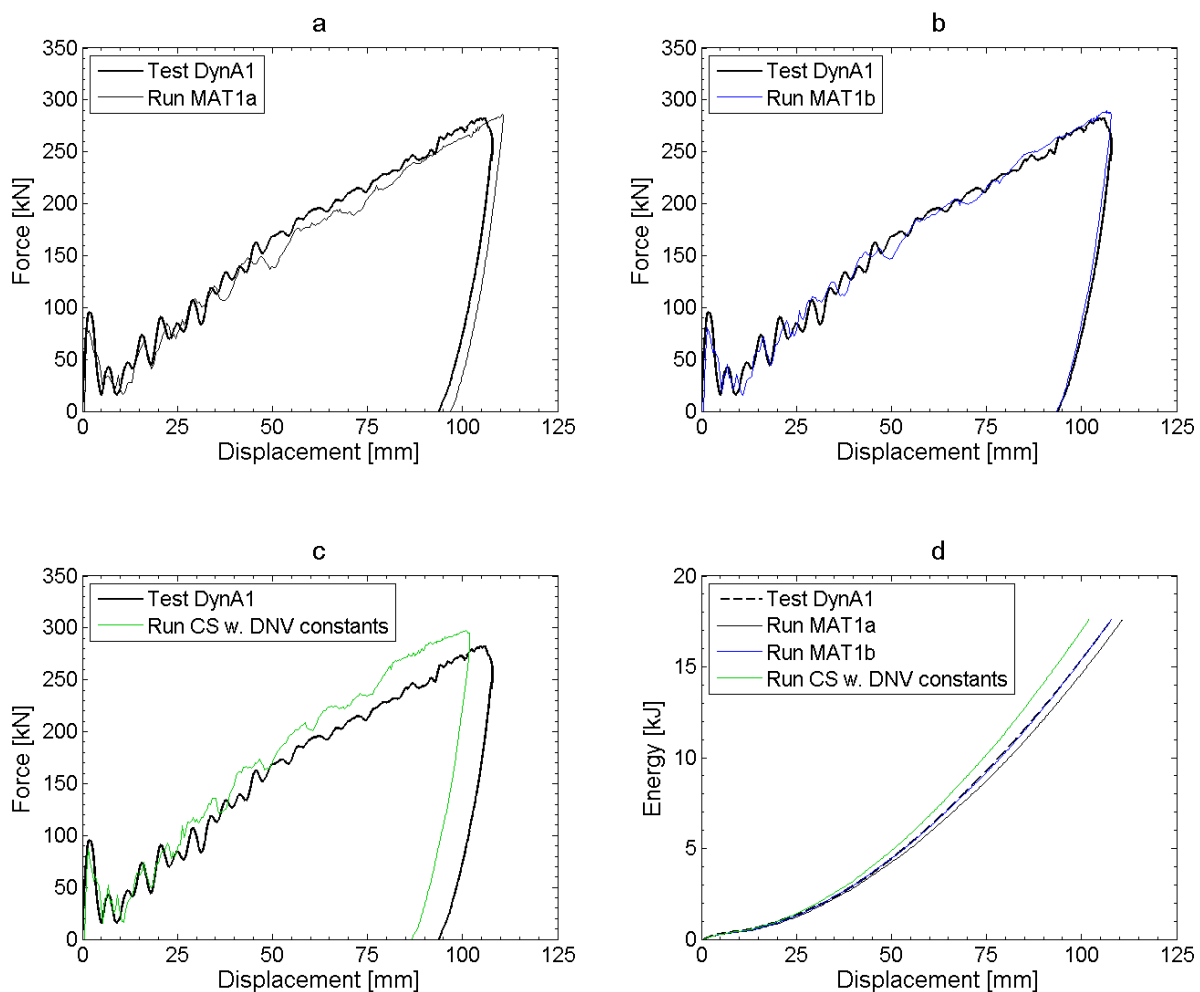


**Figure 6-22: Comparison of results from dynamic simulations with indenter A using MAT1a, MAT1b, and the CS model with proposed constants from DNV-RP-C208.**

### 6.5.2 Quasi-static versus dynamic simulation

Regardless of the accuracy of the established rate parameters, the increased strength and reduced ductility due to strain rate effects does not seem to be very important when determining the capacity according to BWH instability criterion or DNV-RP-C208 for the situations investigated. This is seen by evaluating the difference between static and dynamic test results (both original and adjusted) at the allowable load levels. This implies that a similar impact condition with the applicable material can be analyzed without taking strain rate effects into account without too much error. Further can the applicable impact problems studied herein be simulated quasi-statically when determining the capacity according to the BWH instability criterion or DNV-RP-C208, as the dynamic and quasi-static response is relatively similar.

However, the simulations using the CL criterion that predicted fracture with high precision in the quasi-static condition, did overestimate the capacity in the dynamic condition. The simulation was not able to capture the reduced ductility that apparently was present in the dynamic condition, resulting in non-conservative results.

### 6.5.3 Comparison of methods used to predict tensile failure

#### Description

In this part the three main approaches used to predict tensile failure are compared against each other. The test results are also included. The quasi-static test results are represented by test QSA1 and test QSB1. The latter showed the lowest capacity of the two tests using indenter B. The dynamic test results are represented by test DynB2, which displayed the lowest capacity of the two tests performed with a velocity of approximately 5.7m/s.

Considering a dropped object design condition the most relevant information is usually the energy absorbing capacity of the structure before fracture and the energy-displacement relation. The elastic strain energy and dissipated energy is interesting as it directly indicates the amount of kinetic energy allowed in the impact. The displacement due to an accidental impact can be interesting for situations where equipment is installed directly below the struck target. Therefore, when comparing the results from the three approaches used to predict tensile failure against each other and against the tests, energy-displacement curves are included in addition to force-displacement curves. The energy from the analysis is equivalent as previously calculated for the tests, i.e. sum of all elastic strain energy and dissipated energy which equals the external work inflicted by the indenter.

In all validation methods, the capacity is found for a simulation with mesh size 3mm and with the elastic-plastic material model MAT1a. The capacity found using this input is the one that will be used in the comparisons which are made herein. In the three following figures, the capacity according to the CL criterion is referred to as “Fracture, CL”. The capacity according to the BWH instability criterion is referred to as “Fracture, BWH”. The capacity according to DNV-RP-C208 is referred to as “Fracture, DNV”. The real capacity found from tests is referred to as “Fracture, Test”.

#### Quasi-static load condition

Figure 6-23 shows a comparison between the methods used to predict tensile failure of the stiffened steel plate subjected to a concentrated quasi-static load from indenter A. Figure 6-24 shows the same for a quasi-static load from indenter B.

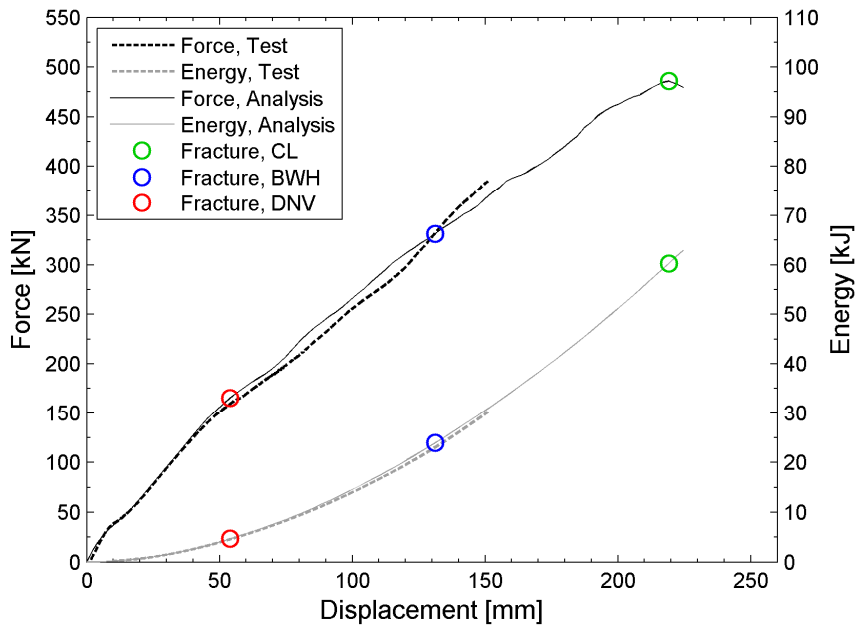


**Figure 6-23: Comparison of methods to predict tensile failure, Quasi-static load condition with indenter A: Force-displacement and energy-displacement curves.**

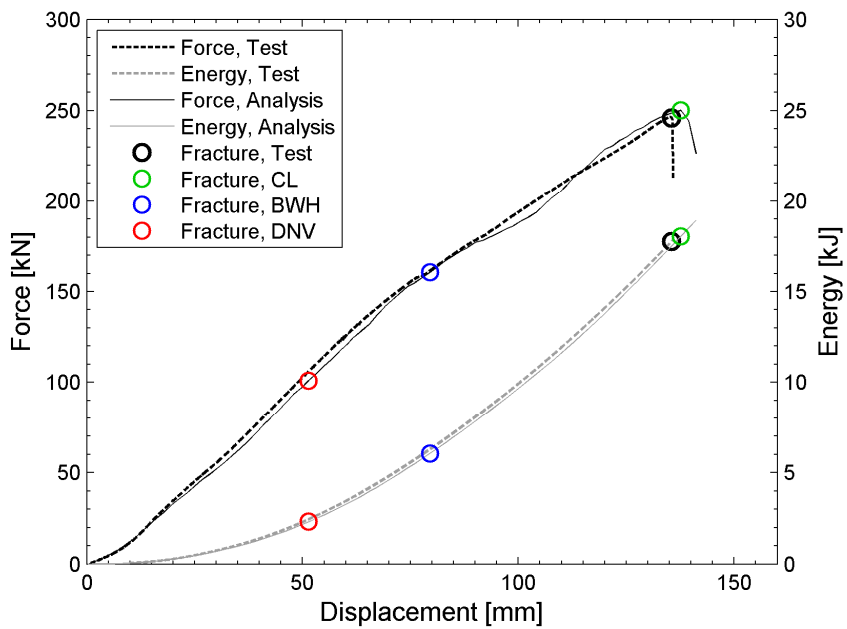


**Figure 6-24: Comparison of methods to predict tensile failure, Quasi-static load condition with indenter B: Force-displacement and energy-displacement curves.**



### Dynamic load condition

Figure 6-25 shows a comparison between the methods used to predict tensile failure of the stiffened steel plate subjected to a concentrated dynamic load from indenter B.

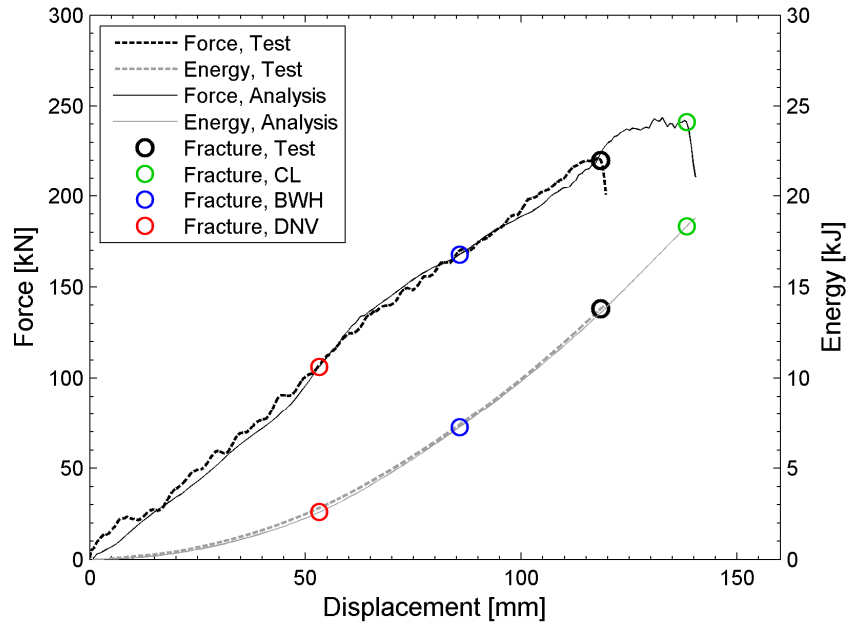


**Figure 6-25: Comparison of methods to predict tensile failure, Dynamic load condition with indenter B: Force-displacement and energy-displacement curves.**

### Discussion

From the three previous figures it is seen that there is a large scatter in the load and energy level at fracture for the three different methods investigated. It is interesting to see how conservative the allowable load and energy levels according to DNV-RP-C208 is compared to the simulation with the CL fracture criterion. The allowable load and energy levels according to the BWH instability criterion is always positioned somewhere in between the two other approaches.

Compared to the fracture load and energy from the tests, it becomes evident that the current simplified method to predict tensile failure in DNV-RP-C208 is very conservative for a structure with the applicable geometry and material properties subjected to the loads as in the present study. If focusing on the dynamic load condition, the allowable fracture energy is less than 20% of the minimum fracture energy measured from the tests. The corresponding ratio for the BWH instability criterion is approximately 50%. If considering the fracture load rather than fracture energy, the ratios will of course be higher. Also the fracture energy from the dynamic tests is probably underestimated slightly as previously discussed. Although the quasi-static simulation using the CL criterion predicted fracture energy very close to the test results, the corresponding dynamic simulation overestimated the capacity regardless whether original or adjusted test data is considered.

It is underlined that DNV-RP-C208 is intended for a wide range of structures and load conditions and might not always be as conservative for other applications as observed in the

present study. Further, the critical failure lines and locations for local yielding were chosen manually when determining the structural capacity in this study. With this approach, the resulting calculated resistance will always depend on the experience and judgement of the responsible engineer. This will at least be the case for larger and more complex structures than the stiffened steel panel visited in this study.

Simulations with a coarse mesh:

The approach from DNV-RP-C208 could be used for simulations with a characteristic element size of up to 5 times the thickness of the plate, i.e.  $l_e=15\text{mm}$ . As a possible increased resistance due a coarse mesh must be reduced by a resistance knock down based on a convergence study, the calculated capacity will remain more or less unchanged regardless of mesh size.

The BWH criterion in combination with globally applied geometric scaling and a coarse mesh, i.e.  $l_e=(30, 18, 12)\text{mm}$ , consistently provided a capacity lower than the “real” capacity according to BWH criterion. The “real” capacity was defined as the one found using mesh size 3mm. In addition, very little scatter is found when comparing capacities for these simulations. This may be seen by inspecting Figure 6-10 and Figure 6-14. This type of consistency in the calculated resistance is essential for the reliability if such an approach is to be implemented in a structural design code or given as a recommended practice. Although, the capacities found with this approach is perhaps too conservative. Without any type of scaling of the critical stress which accounts for mesh size, the capacity seems to vary to some extent, at least in the element size range 3mm to 12mm.

Although it is worth mentioning that in the quasi-static simulation using indenter A and element size 30mm in combination with the BWH instability criterion without scaling, fracture did not occur for an indentation of 250mm. This is perhaps no surprise if one considers the limited extent of the critical strain concentration as shown in Figure 6-3, and if inspecting the mesh at this area as shown in Figure 4-27a. Whether fracture would have occurred for this level of indentation is not known. However, it is plausible as the simulation using the CL criterion and a dense mesh did predict fracture for this level of indentation. This demonstrates that the BWH instability criterion in combination with a coarse mesh can give conservative results for certain applications, while it can give non-conservative results for others. I.e. without any type of geometric scaling, conservative results cannot be guaranteed.

In an interesting failure model recently proposed by Storheim et al. [23], the BWH instability criterion is combined with a damage model. Instead of removing the elements from the mesh at the moment local necking is predicted by the BWH criterion, a mesh size dependent damage model is activated allowing further post-necking deformation before element removal. The damage model assumes that strain localization occurs locally inside the element within a virtual neck, and calculates a gradual reduction in the load-carrying capacity of an element based on geometrical considerations. One may argue that the deformation energy within a local neck is small within each element. However, a delay in element removal followed by a gradual reduction in element stiffness may allow a redistribution of stresses to occur for certain situations, which again could allow for a further increase in the applied load. The results obtained using this coupled-damage model in simulations of indentation tests shows good agreement with experiments when instability is predicted by the BWH criterion. Similarly as was observed in the simulations reported in the present work, it was found that a globally applied geometric scaling rule as defined by Equation (2-45) applied to the BWH criterion produces conservative results with small scatter.

As seen from Figure 6-6 a simulation with a coarse mesh and the CL criterion as it is implemented would significantly overestimate the capacity.

The dynamic simulation with mesh size 3mm in the center region and 6mm otherwise, required approximately 15 times more CPU time than the corresponding simulation using mesh size 12mm when run with the same set-up. The equivalent ratio between mesh size 3mm and mesh size 30mm is 25. Without the computational resources required due to the deformable support frame that is included in the simulations, the ratios would have been even higher.

#### **6.5.4 Model accuracy**

##### General

As seen by the results from the numerical simulations, the component test results are reproduced well by means of the finite element method. Excellent agreement is found when comparing force-displacement relations and energy-displacement relations. However, in order to obtain these results, great effort was needed in order to model the correct boundary conditions present in the test set-up. This effort resulted in the computer model with deformable elements simulating the support frame stiffness. This representation of the support frame may be argued to be disproportionate detailed considering it is the behaviour of the stiffened steel plates that are of interest.

Part of the reason for using the computer model with deformable frame in the validation phase of the study, was the behaviour of the shim plates during loading. The behaviour of these plates causes relatively complicated contact conditions. As they are allowed to translate horizontally, the geometry of the supports varies which again influence the stiffness. If the current support frame is used in further research work, a solution may be to skip the shim plates altogether. Especially for a concentrated load configuration similar as the one inflicted by hemispherical indenter in this study, it is believed that the loss of support surface at the cut-outs would not be a major issue. The decision of including shim plates was made based on the behaviour of the plate loaded by a large size indenter to a large indentation. If the shim plates are excluded from the tests, a computer model with a rigid simulation of the support frame similar as the one presented in section 4.5.2, is believed to produce more reasonable results. However, reduced stiffness due to deformations of the frame and Teflon sheets, allowing the plate to buckle at the supports will still occur for large load levels.

##### Material models

The BWH instability criterion was more conservative for the structure in the present study than expected in advance. The level of accuracy obtained by the simulations of indentation tests performed by e.g. Alsos et al. [7] on unstiffened and stiffened steel plates in S235 material grade is in general higher. Although, it is interesting to see that the conservatism was highest in the indentation test of an unstiffened panel where the stress state in the critical zone resembles the one in the critical zone for tests using indenter B in the present study. As previously mentioned the stress state in the region directly below the indenter can be described as “almost” equi-biaxial tension. Conservative results for this stress state in combination with the BWH instability criterion was also observed by Storheim et al. [23] which simulated formability tests of ship construction steel varying from uniaxial tension to equi-biaxial tension.

Naturally, the accuracy of the BWH instability criterion is also affected by the accuracy of the constitutive equation used to describe the relation between stresses and strains. Using this criterion, the abilities of the power law model to represent post-necking hardening are important.

In section 3.2.2 it was shown that the gauge area in an FEA of the tension test using the established material model based on the power law expression necks down at a greater rate than the test. It was assumed that the main reason for a slower necking phase in the test compared to the simulation was due to strain rate effects present in the test. It is possible that the strain rate effects were exaggerated to some extent. A similar behaviour is not necessarily the case for all steel materials, where a power law model curve fitted to a tension test up to necking might overestimate the further strain hardening. Such an overestimation would imply that post-necking deformation develops more slowly in the FEA than in the tension test. Of course, the stress state in a uniaxial tension tests is different than in the sub panels between stringers so the same behaviour does not necessarily have to be present in the simulations of the component tests. Nevertheless, it illustrates the importance of using appropriate estimates of the post-necking strain hardening if a criterion such as the BWH instability criterion should be implemented in a structural design standard or be given as a recommended practice.

## 7 CONCLUSIONS AND RECOMMENDATIONS

### 7.1 Conclusions

#### Experimental set-up and test results:

The design and set-up of the component tests were a success, and both quasi-static and dynamic tests of stiffened steel plates subjected to concentrated loads could be conducted. The support frame designed for testing of stiffened panels performed well and allowed for testing of eight stiffened steel plates in the present study. The chosen combination of steel plate geometry and support conditions was best suited for tests with a locally applied load between two stringers.

Except for the initial transient phase, the general dynamic and quasi-static response is similar. However, the test results indicate that the dynamic fracture energy is lower than the corresponding static one for the applicable structure and load conditions studied. It is underlined that this observation is based on the results from only two dynamic and two quasi-static tests.

#### Numerical modeling and validation based on tests:

The component test results are reproduced well by means of the finite element method. Excellent agreement is found when comparing force-displacement relations and energy-displacement relations. To achieve these results an accurate representation of the support conditions, i.e. simulation of the support stiffness and behaviour, was found to be important.

The three implemented approaches to predict tensile failure, the CL fracture criterion, BWH instability criterion and the industry approach by using the simplified method in DNV-RP-C208, resulted in significant different predictions of the load level at failure. It was possible to calculate the capacity with high precision using the CL fracture criterion. However, the way this fracture criterion was implemented in the present study it was inefficient with regard to computational time as it required a very dense mesh to obtain reliable results. For the applicable structure in this report, the Bressan-Williams-Hill instability criterion predicted acceptable estimates of the capacity, although with a higher degree of conservatism than expected in advance. Nevertheless, this would be the preferred method, as it gives reasonable predictions of the capacity and can be used in combination with a coarse mesh. The simplified method in DNV-RP-C208 produces overly conservative results for the problems investigated. Additionally it can be cumbersome to manually identify and analyze critical yield lines and local yield zones as required by the simplified method in DNV-RP-C208.

Based on the findings from the performed work presented in this report the following modeling guidelines with respect to similar impact problems are given:

1. The characteristic structural resistance of a stiffened steel plate subjected to a concentrated load can be determined by predicting the onset of instability in tension, using the BWH criterion. The criterion can quite easily be implemented into a commercial finite element software such as Abaqus, and does not require detailed material or failure data. Results to the safe side were obtained for simulations with characteristic element length spanning from one times the thickness, to ten times the thickness of the plate. However, the coarsest mesh produced non-conservative results in one particular problem as the mesh was not able to detect the critical strain concentration. In order to get robust failure response of coarsely meshed shell structures, a geometric mesh scaling rule to overcome the shortcomings of a too coarse mesh may be required.
2. The impact problems may be analyzed quasi-statically when determining the characteristic resistance based on the method above as the dynamic and static response is similar.

### **7.2 Recommendations for further work**

The performed work presented in this report has led to the following recommendations for further work regarding the impact behaviour of stiffened steel plates:

1. Study the response when having other indenter geometries. The geometries could represent real life dropped objects relevant for the offshore industry.
2. Study the effect of an impact directly on top of a stringer.
3. Study the effect of an impact near the support.
4. Study the effect of possible reduced ductility in local areas of the plate field due to welds.
5. Study the relationship between static and dynamic fracture energy for a stiffened steel plate constructed of a typical offshore structural steel.
6. Study how different steel material properties (combinations of yield strength and strain hardening) with corresponding different properties of the power law expression affect the accuracy when predicting the capacity using the BWH instability criterion.
7. In relation to all points above, establish detailed modeling guidelines to be given as a recommended practice on how to establish structural resistance of a large scale shell structure subjected to impact loading by use of non-linear finite element methods.

---

## 8 BIBLIOGRAPHY

### Literature:

- [1] R. D. Cook, D.S. Malkus, M. E. Plesha, R. J. Witt, *Concepts and Application of Finite Element Analysis*, 4th ed. John Wiley & Sons, New York, 2002
- [2] J.A. Zucas, T. Nicholas, H. Swift, *Impact Dynamics*, Krieger Publ. Co, Malabar, 1992
- [3] O.S. Hopperstad, T. Børvik, *Lecture Notes, Materials Mechanics Part I*, Structural Impact Laboratory (SIMLab). Trondheim, 2013
- [4] G.E. Dieter, *Mechanical metallurgy*, McGraw-Hill, New York, 1961
- [5] Z. Marciniak, J. L. Duncan, S. J. Hu, *Mechanics of Sheet Metal Forming*, 2th ed. Butterworth-Heinemann, 2002
- [6] H.S. Alsos, J. Amdahl “On the resistance to penetration of stiffened plates, Part I - Experiments”. *International Journal of Impact Engineering*, Vol. 36, No. 6, 2009, pp. 799-807.
- [7] H.S. Alsos, J Amdahl, O.S. Hopperstad, “On the resistance to penetration of stiffened plates, Part II - Numerical analysis”. *International Journal of Impact Engineering*, Vol. 36, No. 7, 2009, pp. 875-887.
- [8] H.S. Alsos, O.S. Hopperstad, R. Törnqvist, J. Amdahl, “Analytical and numerical analysis of sheet metal instability using a stress based criterion”, *International Journal of Solids and Structures*, Vol. 45, No 7, 2008, pp 2042-2055.
- [9] S. Ehlers, J. Broekhuijsen, H.S. Alsos, F. Biehl, K. Tabri, “Simulating the collision response of ship side structures: A failure criteria benchmark study, *International Shipbuilding Progress*, Vol. 55, pp. 127-144
- [10] R. Villavicencio, C. G. Soares, “Numerical prediction of impact loads in rectangular panels” *Advances in Marine Structures: proceedings of the 3<sup>rd</sup> International Conference on Marine Structures: MARSTRUCT 2011, Hamburg, Germany, 28-30 March 2011 / editors, C. Guedes Soares, W. Fricke*, Leiden, The Netherlands: CRC Press,2011
- [11] B. Liu, R. Villavicencio, C.G. Soares, “Simplified analytical method to evaluate tanker side panels during minor collision incidents”. *International Journal of Impact Engineering*, Vol. 78, 2015, pp. 20-33
- [12] M. Langseth, P.K. Larsen, “Dropped objects’ plugging capacity of steel plates: An experimental investigation”, *International Journal of Impact Engineering*, Vol. 9, No 3, 1990, pp. 289-316

- [13] M. Langseth, T. Berstad, P.K. Larsen, A. Jensen “Impact loading of Plates: A Comparison between Numerical Simulations and Experimental Results”, Prepared for submittal to the *Sixth International Symposium on the Interaction of Nonnuclear Munitions with Structures*, 1993
- [14] M. Langseth, “Dropped objects: plugging capacity of steel plates”, Dr ing. Thesis, Division of Structural Engineering, NTH, Trondheim, 1988
- [15] M. E. Backman, W. Goldsmith. “The mechanics of penetration of projectiles into targets”, *International Journal of Engineering Science*, Vol. 16. No. 1, 1978, pp. 1-99
- [16] J. Amdahl, “Offshore ship collision and dropped objects”, *Last og sikkerhet for marine konstruksjoner*, NTH, Trondheim, 1985
- [17] G. Gruben, O.S. Hopperstad, T. Børvik, “Evaluation of uncoupled ductile fracture criteria for the dual-phase steel Docol 600DL”, *International Journal of Mechanical Sciences*, Vol. 62, 2012, pp. 133-146
- [18] G. Gruben, D. Vysochinskiy, T. Coudert, A. Reyes, O.-G. Lademo, “Determination of Ductile Fracture Parameters of a Dual-Phase Steel by Optical Measurements”, *Strain*, Vol. 49, No. 3, 2013, pp. 221-232
- [19] S. Dey, T. Børvik, O.S. Hopperstad, M. Langseth, “On the influence of fracture criterions in projectile impact of steel plates”, *Computational Materials Science*, Vol. 38, 2006, pp. 176-191
- [20] M. G. Cockcroft, D. J. Latham, “Ductility and the Workability of Metals”, *Journal Institute of Metals*, Vol. 96, 1968, pp. 33-39
- [21] R. Hill, “On discontinuous plastic states, with special reference to localized necking in thin sheets”, *Journal of the Mechanics and Physics of Solids*, Vol. 1, No.1, 1952, pp. 19-30
- [22] J.D. Bressan, J.A. Williams, “The use of a shear instability criterion to predict local necking in sheet metal deformation”, *International Journal of Mechanical Sciences*, Vol. 25, No. 3, 1983, pp. 155-168
- [23] S. Storheim, H.S. Alsos, O.S. Hopperstad, J. Amdahl, “A damage-based failure model for coarsely meshed shell structures”, *International Journal of Impact Engineering*, Vol. 83, 2015, pp. 59-75
- [24] A. G. Hansen, T. Auestad, T. Tryland, M. Langseth, “The kicking machine: A device for impact testing of structural components”, *International Journal of Crashworthiness*, Vol. 8, No. 4, 2003, pp. 385-392
- [25] K. M. Mathisen, “Lecture 1: The Finite Element Method - Introduction and Fundamental Concepts”, Lecture Notes in TKT4192 Finite Element Methods in Strength Analysis, NTNU, 2013
- [26] K. M. Mathisen, “Lecture 9: Solution of the Nonlinear Dynamic Equilibrium Equations”, Lecture Notes in TKT4197 Nonlinear Finite Element Analysis, NTNU, 2014
- [27] K. M. Mathisen, “Lecture 12: Formulation of Geometrically Nonlinear FE”, Lecture Notes in TKT4197 Nonlinear Finite Element Analysis, NTNU, 2014



Industry standards and recommended practices:

- [28] DNV-RP-C208, *Determination of Structural Capacity by Non-linear FE analysis Methods*, 2013
- [29] ISO 19900:2013, *Petroleum and natural gas industries - General requirements for offshore structures*
- [30] ISO 19902:2007, *Petroleum and natural gas industries - Fixed steel offshore structures*
- [31] ISO 898-1:2013, *Mechanical properties of fasteners made of carbon steel and alloy steel - Part 1: Bolts, screws and studs with specified property classes - Coarse thread and fine pitch thread*
- [32] NS-EN 1993-1-5:2006, *Design of steel structures - Part 1-5: Plated structural elements*

Websites:

- [33] Engineer's Handbook, *Reference Tables -- Coefficients of friction*, URL <http://www.engineershandbook.com/Tables/frictioncoefficients.htm>, Accessed April 25, 2015

Computer software:

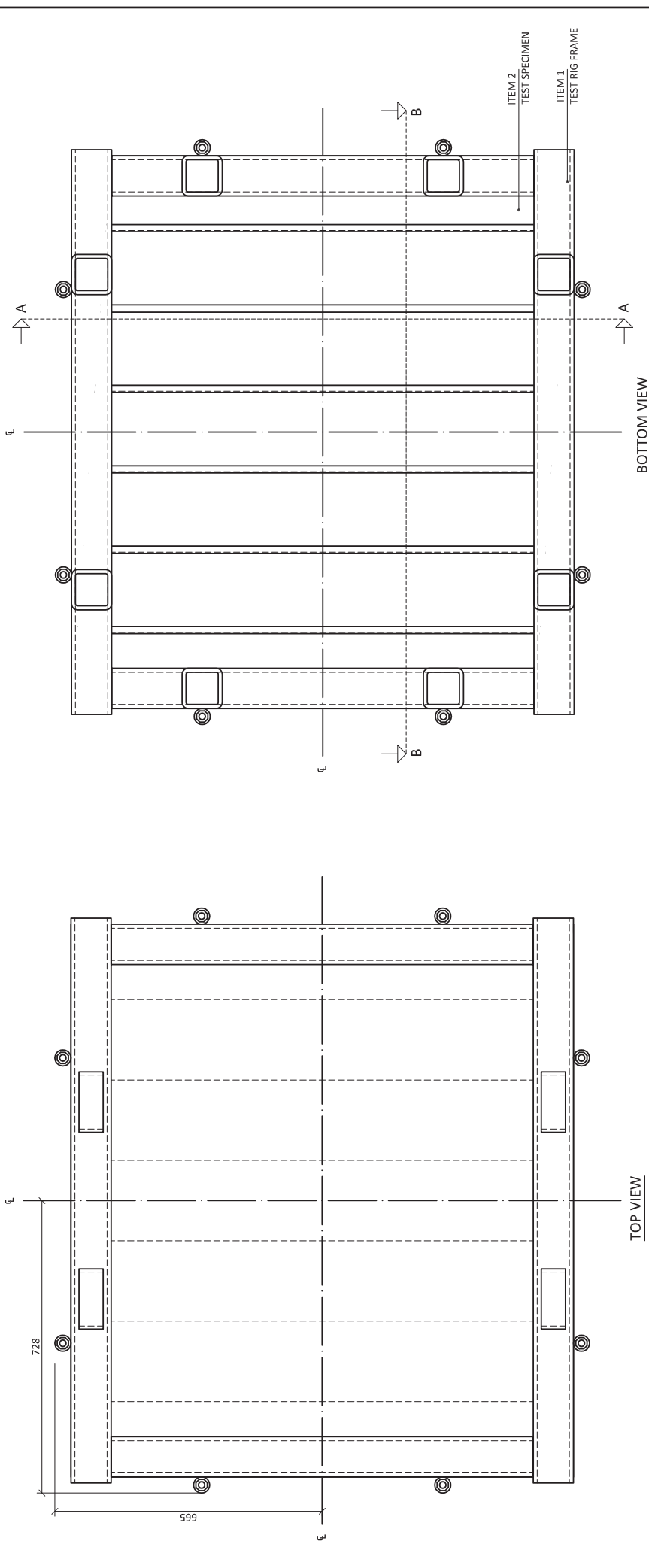
- [34] Abaqus/CAE 6.14-1, Dassault Systèmes SIMULIA Corp, USA, 2014
- [35] Microsoft Office, Microsoft, USA, 2010
- [36] MathCAD 15.0, Parametric Technology Corporation. USA, 2010
- [37] AutoCAD, Autodesk, USA, 2015
- [38] MATLAB 2013b, MathWorks, USA, 2013
- [39] eCorr v3.0 Digital Image Correlation Tool, SIMLab NTNU, Norway, 2013



# APPENDIX A

## DRAWINGS

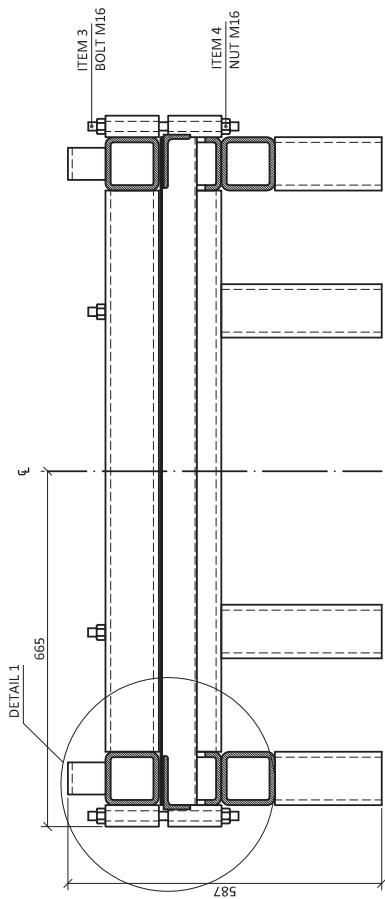
<b>DRAWING NAME</b>	<b>page</b>
TEST RIG - ASSEMBLY	A1
TEST RIG FRAME	A3
PLATE W. STRINGERS	A5



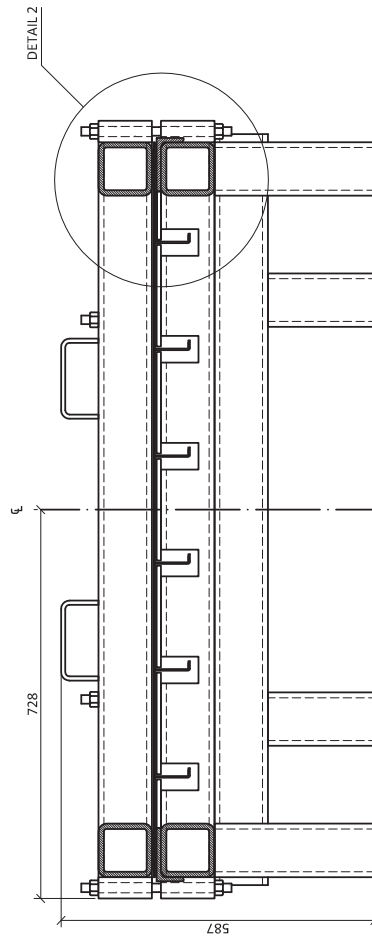
14	6	ANGLE 100x50x8	L=190	S335	-
2	5	ANGLE 100x50x8	L=1050	S335	-
16	4	NUT M16	-	12,9	-
8	3	BOLT M16	-	12,9	-
1	2	PLATE W. STRINGERS	-	-	A-120
1	1	TEST RIG FRAME	-	-	A-110
Qty.	Item	Name of item	Dimensions of item	Material	Drw. no

Drawing name:  
**TEST RIG - ASSEMBLY**

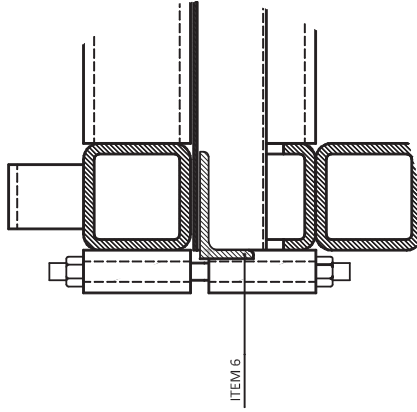
Prepared by:	Size:	Sheet:
Sindre Sølvernes	A3	1/2
Scale:	Date:	Revisions:
1:10	-	Drawing number: A-100



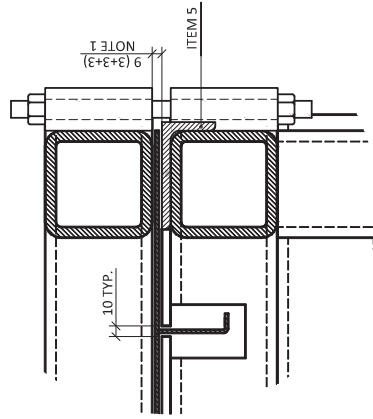
SECTION A-A



SECTION B-B



DETAIL 1  
SCALE 1:5



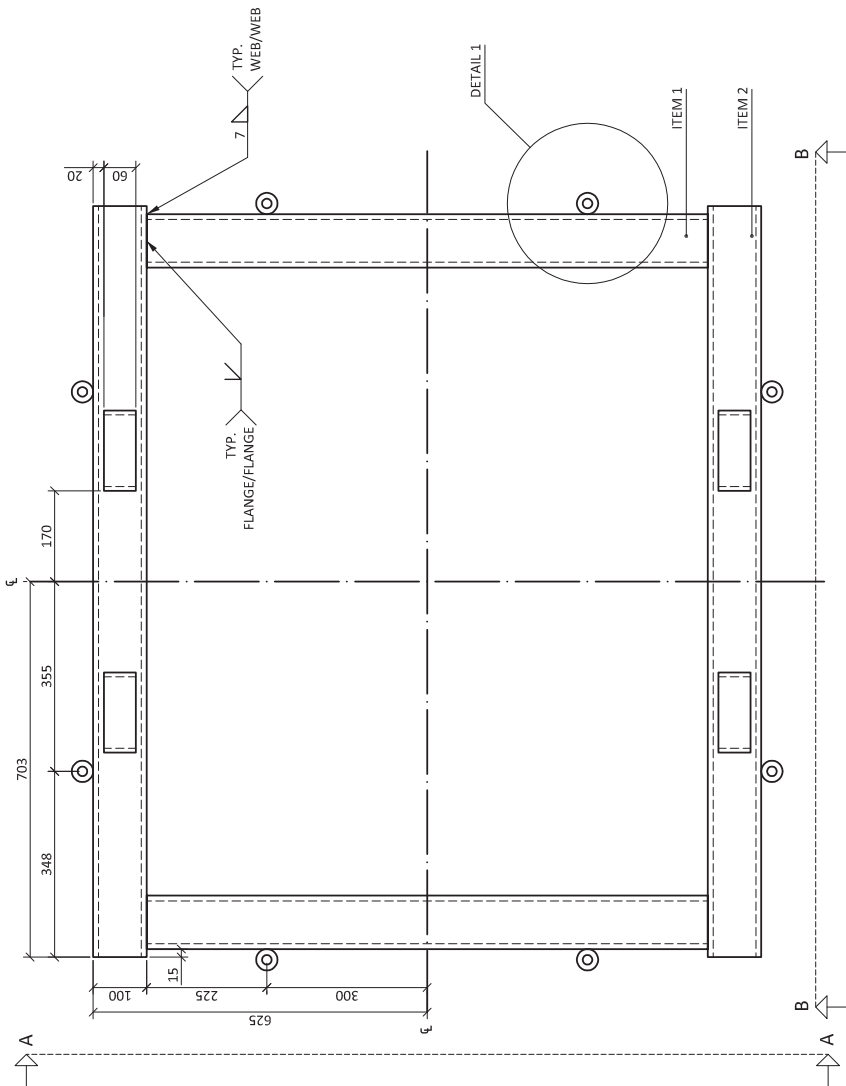
DETAIL 2  
SCALE 1:5

NOTES

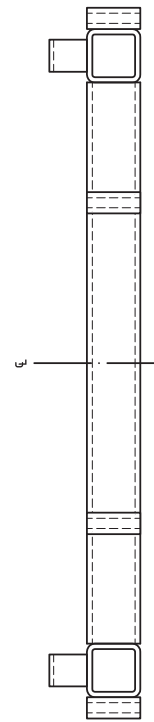
1. TEFLON LAYER, 3MM TO BE INCLUDED ON BOTH SIDES OF TEST SPECIMEN MAIN PLATE TOWARDS SUPPORT FRAME.

Drawing name:  
**TEST RIG - ASSEMBLY**

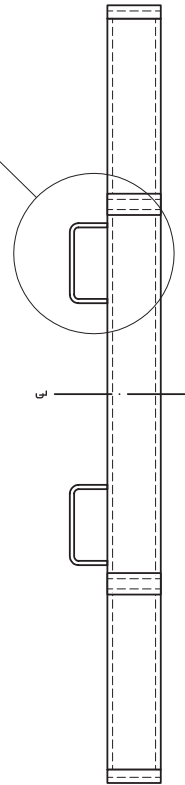
Prepared by: <b>Sindre Sølvernes</b>	Size: <b>A3</b>	Sheet: <b>2/2</b>
Scale: <b>1:10</b>	Date: <b>-</b>	Revision: <b>-</b>
	Drawing number: <b>A-100</b>	



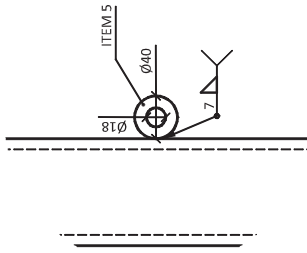
TOP FRAME - TOP VIEW



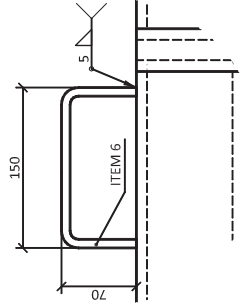
VIEW A-A



VIEW B-B



DETAIL 1  
SCALE 3:5



DETAIL 2  
SCALE 1:5

4	6	SHS150x8	L = 60	S355	-
16	5	RB40	L = 100	S355	-
4	4	SHS100x10	L = 200	S355	-
4	3	SHS100x10	L = 300	S355	-
6	2	SHS100x10	L = 1405	S355	-
4	1	SHS100x10	L = 1050	S355	-
Qty.	Item	Name of item	Dimensions of item	Material	Drw. no

Drawing name:

**TEST RIG FRAME**

Prepared by:

Sindre Sølvernes

Size:

A3

Sheet:

1/2

Scale:

1:10

Date:

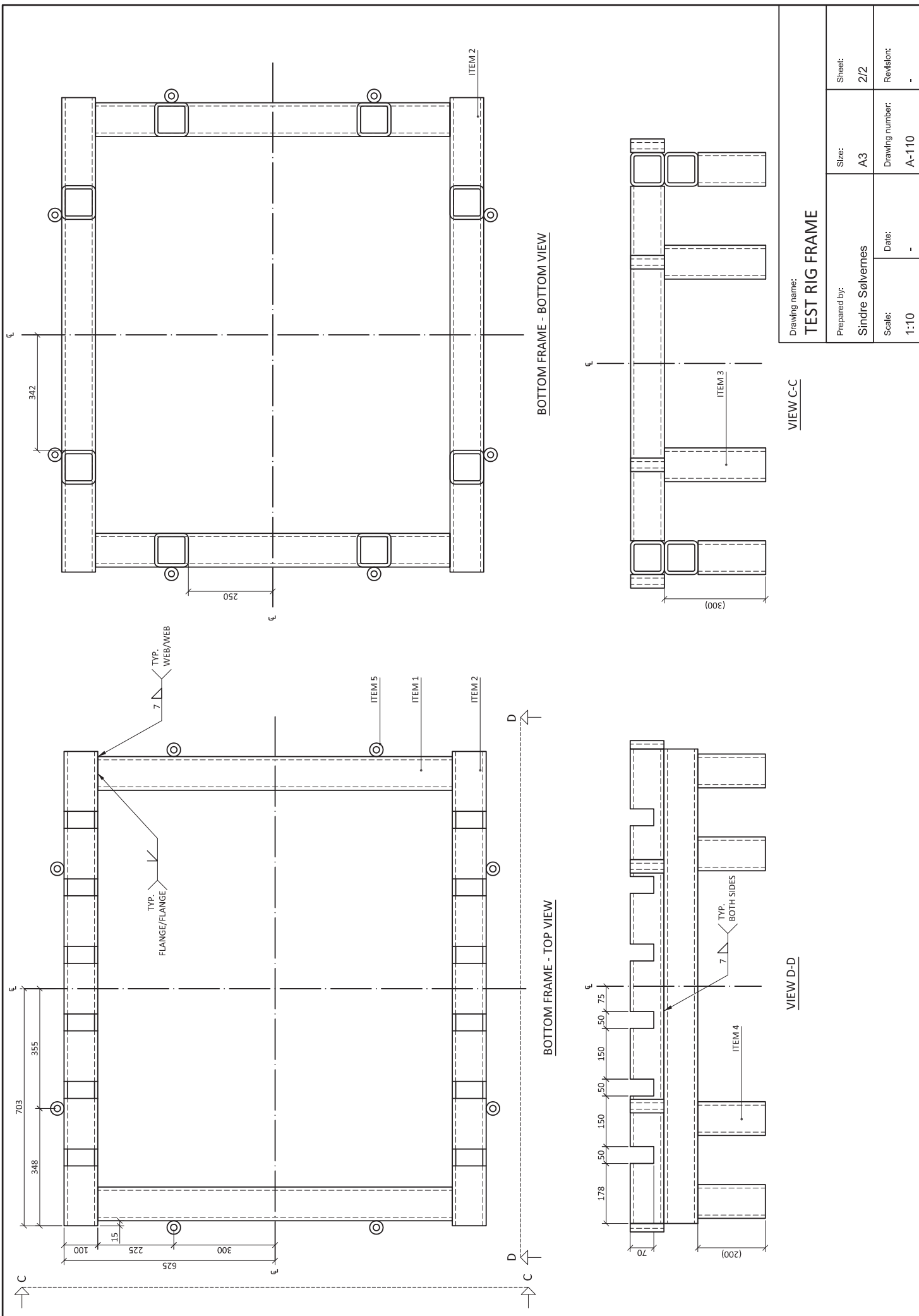
-

Drawing number:

A-110

Revision:

-

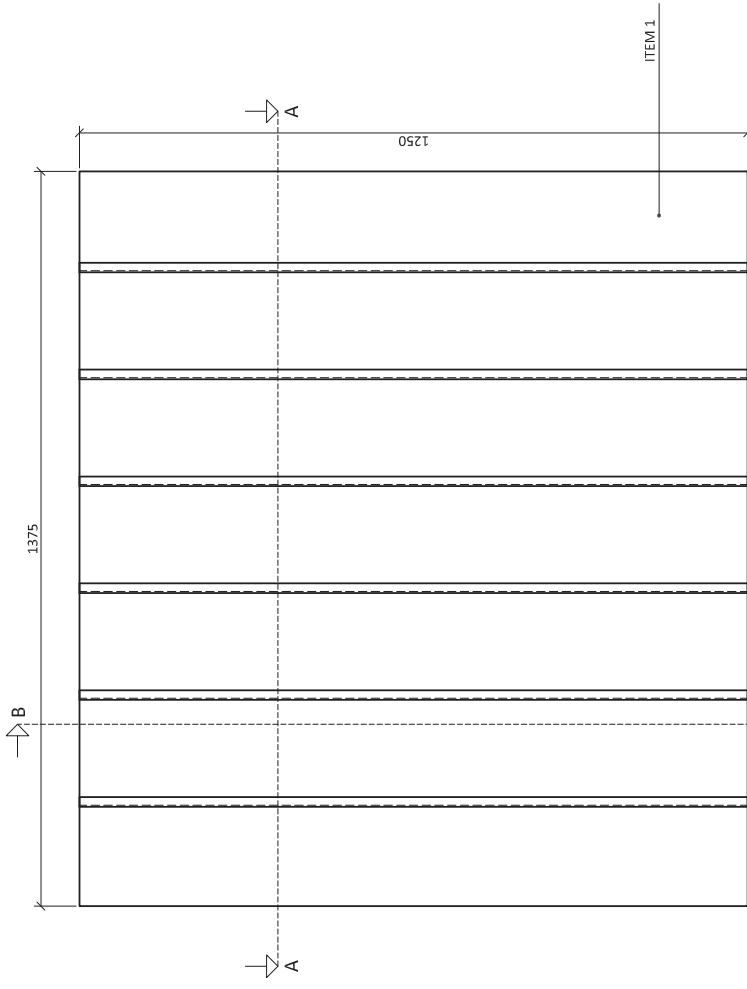


Drawing name:  
**TEST RIG FRAME**

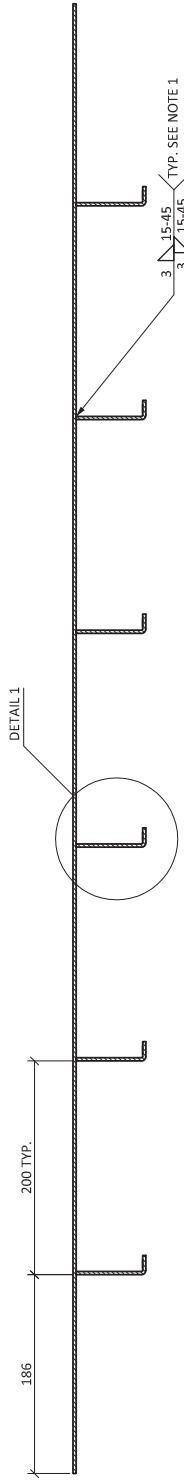
VIEW C-C

VIEW D-D

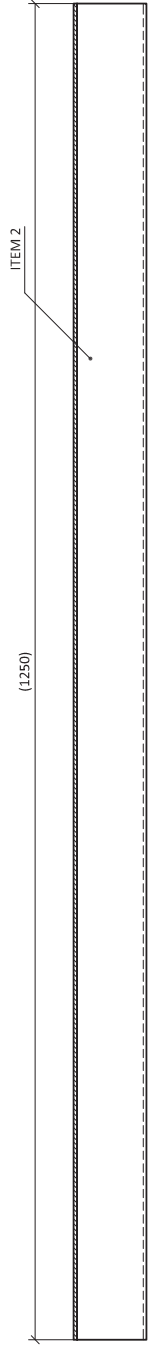
Prepared by: <b>Sindre Sølvernes</b>	Size: <b>A3</b>	Sheet: <b>2/2</b>
Scale: <b>1:10</b>	Date: <b>-</b>	Drawing number: <b>A-110</b>
		Rev/Slot: <b>-</b>



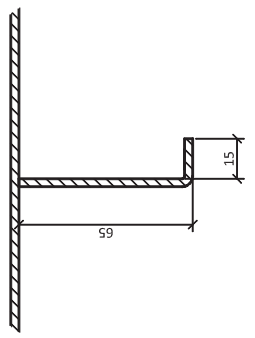
**BOTTOM VIEW**



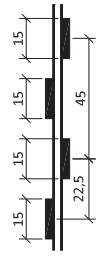
**SECTION A-A**  
SCALE 1:5



**SECTION B-B**  
SCALE 1:5



**DETAIL 1**  
SCALE 1:2



**NOTES**

1. APPLICATION OF DIMENSIONS TO INTERMITTENT FILLET WELD IS SHOWN IN FIGURE BELOW. IF REQUIRED BY ACTUAL LENGTH OF THE JOINT, THE LENGTH OF THE INCREMENT OF THE WELDS AT THE END OF THE JOINT SHOULD BE INCREASED TO TERMINATE THE WELD AT THE END OF THE JOINT.

6	2	PLATE	1250x60x3	S355	-
1	1	PLATE	1375x1250x3	S355	-
Qty.	Item	Name of item	Dimensions of item	Material	Dwg. no
Drawing name: <b>PLATE W. STRINGERS</b>					
Prepared by: <b>Sindre Salvemes</b>		Size: <b>A3</b>	Sheet: <b>1/1</b>		
Scale: <b>1:10</b>	Date: <b>-</b>	Drawing number: <b>A-120</b>	Revision: <b>-</b>		



## **APPENDIX B**

### **DYNAMIC TEST RESULTS BASED ON ADJUSTED DATA**

<b>CONTENTS</b>	<b>page</b>
Figure B1: Adjusted results from test No. DynB1, $M=1429\text{kg}$ , $v_0=5.70\text{m/s}$	B1
Figure B2: Adjusted results from test No. DynB2, $M=1429\text{kg}$ , $v_0=5.72\text{m/s}$	B2
Figure B3: Adjusted results from test No. DynB3, $M=1429\text{kg}$ , $v_0=4.49\text{m/s}$	B3

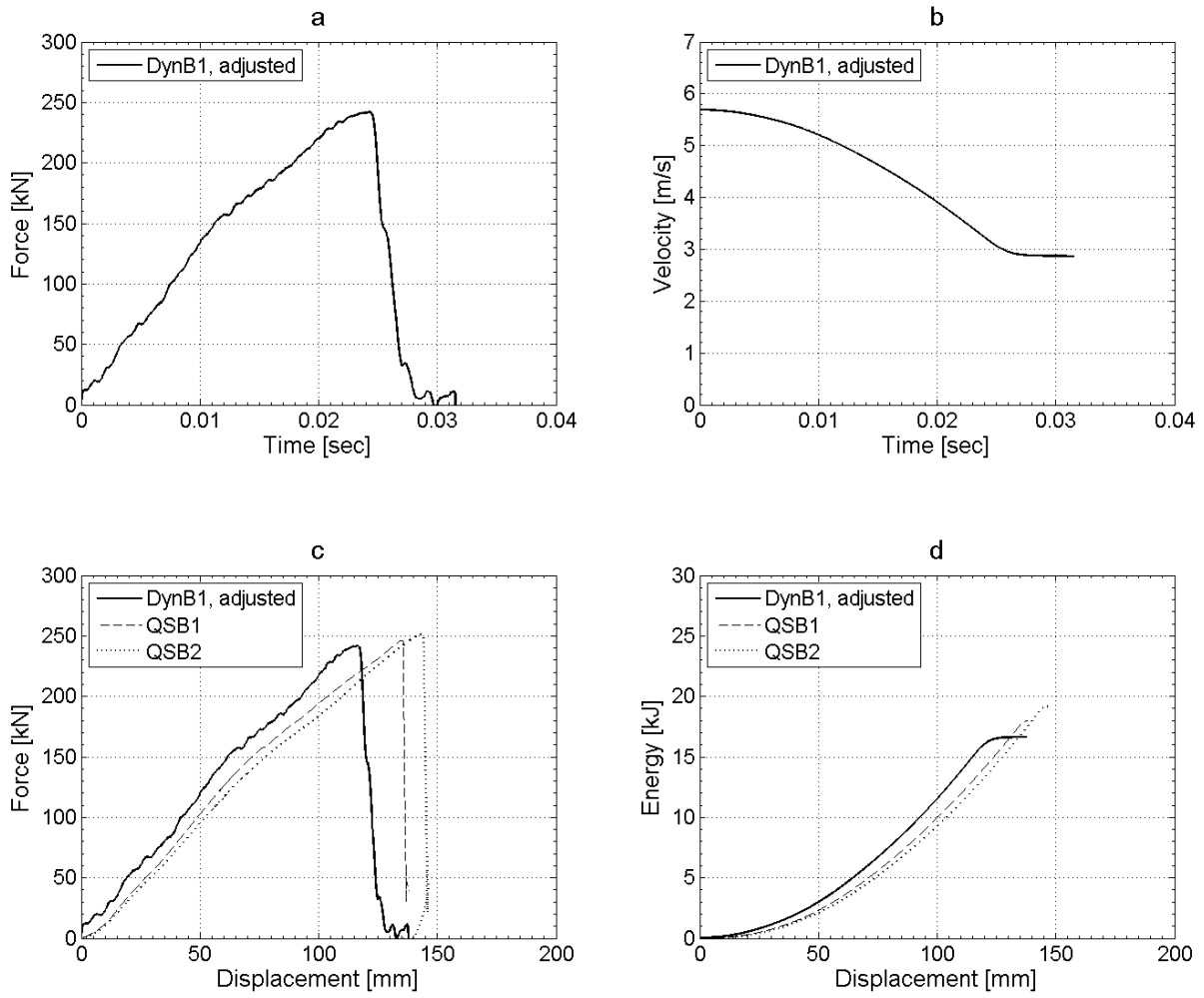


**Figure B1: Adjusted results from test No. DynB1,  $M=1429\text{kg}$ ,  $v_0=5.70\text{m/s}$**

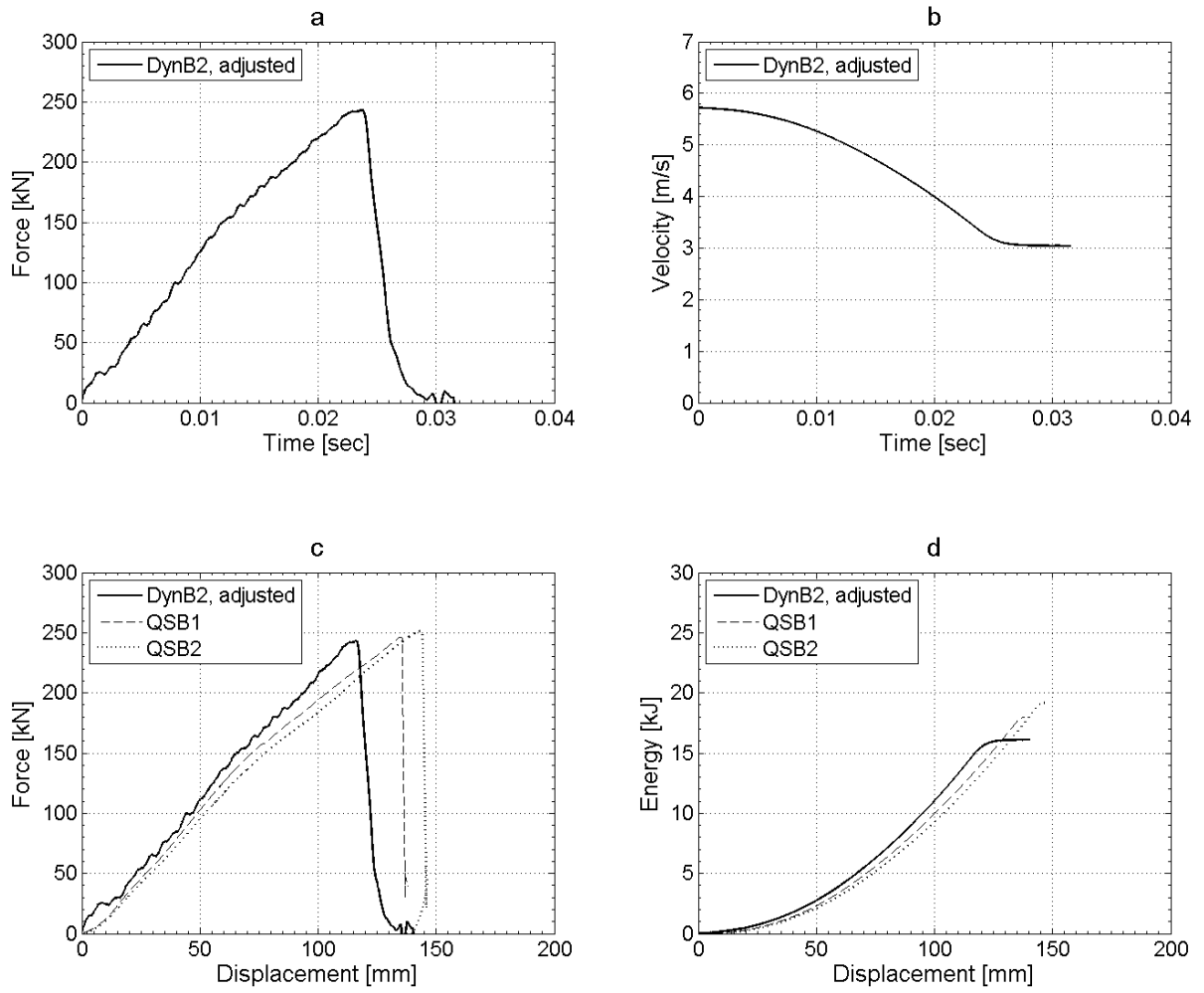


**Figure B2: Adjusted results from test No. DynB2,  $M=1429\text{kg}$ ,  $v_0=5.72\text{m/s}$**

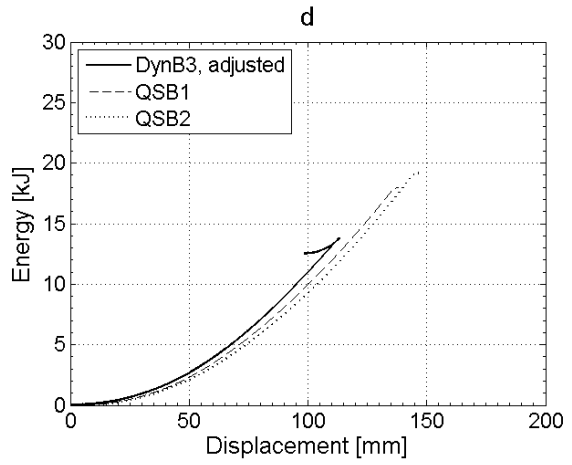
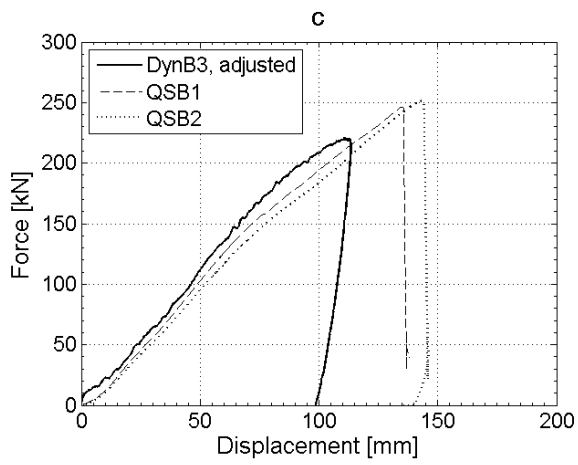
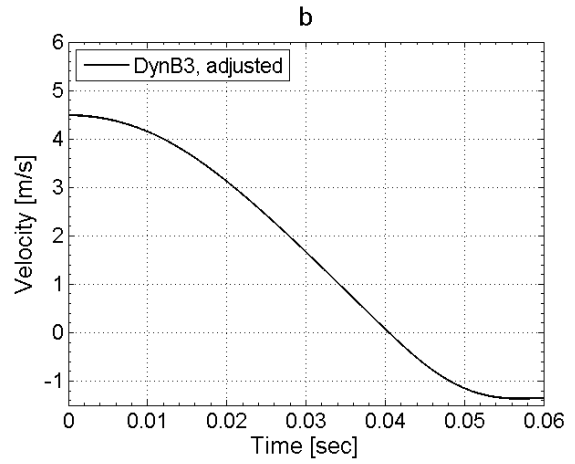
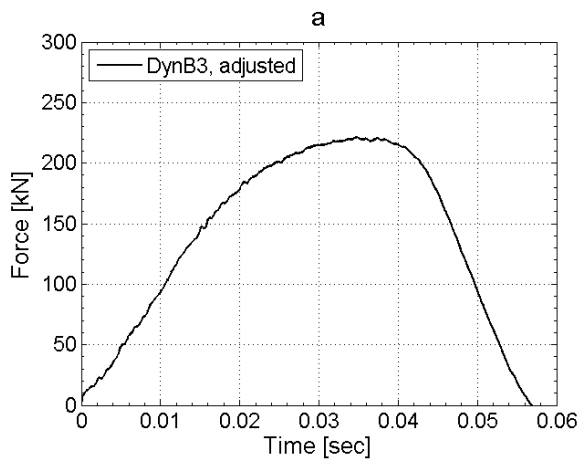


**Figure B3: Adjusted results from test No. DynB3,  $M=1429\text{kg}$ ,  $v_0=4.49\text{m/s}$**